Neutral Pion Production in Proton+Proton Collisions at $\sqrt{s} = 8$ TeV and Insight into Hadron Production Mechanism

Hiroshima University
Graduate School of Science
Department of Physical Science

Satoshi Yano

March 5, 2018

Abstract

High transverse momentum particles play an important role for investigation of Quark-Gluon Plasma (QGP) induced by nucleus-nucleus collisions. When high transverse momentum partons traverse the QGP, they lose their energy. Consequently, the yield of high transverse momentum hadron is suppressed relative to proton+proton collisions scaled by the number of binary nucleon-nucleon collisions (jet quenching). The phenomenon is expected to give us much information about properties of QGP.

Thus far, almost all models consider only parton energy loss during passing through. However, the perturbative Quantum Chrome Dynamics (QCD) predicts the direct hadron production (the higher-twist effect). If hadrons produced by this mechanism exist, the hadron energy loss should be considered additionally. For checking if there is the higher-twist effect, investigation of hadron production in proton+proton collisions is suitable.

The invariant differential cross sections for inclusive neutral pion at midrapidity are measured in proton+proton collisions at $\sqrt{s} = 8$ TeV using the ALICE detector at LHC. The neutral pion is identified from the invariant mass of photon pairs detected by the PHOS detector covering $260° < \phi < 320°$ and $|\eta| < 0.12$. To cover a wide transverse momentum range, two different triggers are used. One is a minimum-bias trigger to measure from low to middle transverse momentum range. The other is the high energy photon trigger deployed in PHOS detector to enhance high transverse momentum statistics.

To calculate the neutral pion invariant cross-section, the LHC beam luminosity in proton+proton collisions at $\sqrt{s} = 8$ TeV is measured by using van der Meer scan technique. The luminosity is determined by the ALICE minimum-bias trigger which requires at least one hit on both side of V0 detector with a pseudorapidity coverage of $2.8 < \eta < 5.1$ and $-3.7 < \eta < 1.7$. The cross-section of the trigger is found to be 55.8 ± 1.2 mb^{-1}. The value is a baseline for not only the neutral pion measurement but also other measurements in ALICE.

By using the x_T scaling property, the particle production mechanisms at RHIC and LHC collision energies are investigated. The result reveals that both higher-twist and jet fragmentation should be taken into account for RHIC collision energies, but on the other hand at LHC energies, the higher-twist contribution is found to be negligible below about 20 GeV/c. The result suggests that the high transverse momentum particle suppression is caused by the parton energy loss for the LHC energies, but both parton and hadron energy loss should be taken into account at RHIC.

The phenomena which were not expected have been measured in proton+proton collisions with the high multiplicity event at LHC. To study the phenomena, the production rate of neutral pion is measured as a function of event multiplicity. Two transverse momentum ranges, from 1.0 GeV/c to 1.5 GeV/c and from 5.5 GeV/c to 16 GeV/c, are compared with the Color-Reconnection (CR) model. For both ranges, the model describes the multiplicity dependence of the neutral pion yield.

要旨

通常、クォークやグルーオン（総称してパートン）は、ハドロンの中に閉じ込められている。この状態は、高温・高密度状況下で、パートンがハドロンから解放されたクォーク・グルーオン・プラズマ（QGP）に相転移する。自然界では、ビックバン直後の数マイクロ秒後の世界や中性子星内部が QGP の状態であり、人工的にも高エネルギー原子核衝突実験で作り出すことができる。

　BNL-RHIC 加速器における高エネルギー原子核衝突実験で、QGP 生成の確証を初めて得て、その後、2009 年より稼働する CERN-LHC 加速器でも生成を確認した。この加速器は、RHIC 加速器の 28 倍の衝突エネルギーを実現し、生成する QGP はより高温・長寿命であるため、その性質の精密測定が期待できる。また、両加速器での温度の異なる QGP を用いた系統的な物性研究も始まっている。　性質の解明に有効なプローブとして高横運動量ハドロンの収量抑制がある。高横運動量ハドロンは、衝突初期に硬散乱した高エネルギーパートンが破砕することによって生じる（ジェット機構）。そのようなパートンが QGP を通過する際にエネルギーを失うことで、高横運動量ハドロンの収量が減少すると解釈されている。抑制量のハドロン種や横運動量依存性から、QGP の性質を解明することができる。しかし、摂動 QCD はジェット機構に加え、ハドロンの直接生成も予言している（直接生成機構）。この機構がある場合、パートンのエネルギー損失に加え、ハドロンのエネルギー損失も考慮しなければならない。直接生成の寄与は、衝突エネルギーに依存し、また、ジェット機構で生成した場合と異なる横運動量分布になると予想される。ハドロンとジェットの横運動量分布の比較によって、ハドロンの生成機構を研究することが可能である。　また、LHC 加速器における陽子+陽子衝突の高粒子多重度事象で、今までに考えてこなかった長距離粒子相関を初めて観測した。数々の理論モデルによる理解を試みているが、まだ解明できていない。単純な陽子+陽子衝突においても基本的な粒子生成機構に関して未知な部分がまだある。

　　本論文では、陽子+陽子衝突において幅広い横運動量領域での中性 π 中間子の生成断面積を測定することで、ハドロンの生成機構を研究した。中性 π 中間子の崩壊光子を電磁カロリーメータ（PHOS）で検出し、2 光子の不変質量を計算して粒子を同定する。幅広い横運動量領域を測定するため、最小バイアストリガーだけでなく高エネルギー光子トリガーで取得したデータも用いた。この高エネルギー光子トリガーのデータ解析手法を確立したことで、幅広い横運動量領域（1.0 GeV/c から 30 GeV/c）の生成断面積の測定が可能になった。この結果と ALICE 実験の他の検出方法（EMCal 法、PCM 法、PCM-EMCal hybrid 法）とを統合することにより更に幅広い領域（0.3 GeV/c から 35 GeV/c）の測定に成功した。　この生成断面積の測定には、LHC 加速器のビーム輝度を正確に見積もる必要がある。ビーム分離法を用いることで、ビームの形状が不明な条件下でもビーム輝度を測定することができる。この方法を用いて、誤差 2.6%の精度でビーム輝度を測定することに成功した。　さらに、測定した生成断面積とジェット機構を考慮した摂動モデル計算とを比較した。このモデルは、RHIC 加速器エネルギーでは測定結果を良く再現しているが、LHC 加速器エネルギーでは 50%程度の差異を確認した。また、衝突エネルギーが大きくなると、差異も大きくなっていた。　中性 π 中間子とジェットの運動量分布から、LHC 加速器と RHIC 加速器における高横運動量ハドロンの生成機構を研究した。LHC 加速器エネルギーでは、ハドロンのほとんどがジェット機構によって生成しており、一方で RHIC 加速器エネルギーでは、ジェット機構と直接生成機構の両方が高横運動量ハドロンの生成に寄与していると示唆する結果を得た。直接生成機構を考慮していないモデルで、高横運動量ハドロンの生成を記述しようとしていたため、様々な衝突エネルギーで生成量を統一的に再現できなかったと考えられる。　直接生成機構の減少は、粒子生成に関与する核子内のパートン分布が、衝突エネルギーによって変化することに起因すると考えられる。直接生成は、硬散乱するパートンの一つがクォークである必要がある。しかし、LHC 加速器エネルギーでは、グルーオン対散乱が支配的であるため、直接生成が抑制される。　この研究の成果から、RHIC 加速器エネルギーでは、硬散乱したパートンのエネルギー損失だけでなく、直接生成したハドロンのエネルギー損失も考慮しなければならないが、LHC 加速器エネルギーでは硬散乱したパートンのエネルギー損失のみを考慮すればよいと結論される。　これに加え、運動量領域の異なる中性 π 中間子収量の粒子多重度依存性を測定した。低横運動量領域に比べ高横運動量領域の中性 π 中間子の収量が増加していることを観測した。この結果は、初期パートンの多重硬散乱に起因する色荷再結合モデルの結果と一致しており、LHC 加速器における初期パートンの多重散乱の重要性を示している。

Contents

Chapter 1

Introduction

The Large Hadron Collider (LHC) provides collisions of protons and lead ions at unexploited ultra-relativistic collision energies. The LHC is located at the European Organization for Nuclear Research (CERN) in Geneva and it has been operating since 2009. There are six collider experiments and they have recorded the properties of products induced by collisions to explore the subatomic structure and the properties of the fundamental forces as well as the elementary particles. In order to achieve each physics goal, the detector of the experiments is designed and cover broad ranges of high-energy physics topics.

ALICE (A Large Ion Collider Experiment) is one of the LHC experiments. Its detector is designed to study heavy-ion collisions to investigate properties of deconfined strongly interacting matter, Quark Gluon Plasma (QGP) which is predicted by the Quantum Chromodynamics (QCD). The QCD describes the strong interaction kinematics which is one of the fundamental interactions. The strong interaction is very complex system and there still remain many obscure phenomena, in particular in low energy region. The QGP is expected to have rich information about the strong interaction and is studied vigorously to understand the fundamental mechanism of the particle physics. Furthermore, the QGP is assumed to have existed $\sim 10^{-6}$ second after the big bang and the inside of neutron stars. Therefore, the study of the QGP also leads to understanding the evolution of the universe and stars.

ALICE experiment is also dedicated to the measurement of proton+proton collisions as well as the heavy ion collisions. The detector makes a significant contribution to the study of the particle production mechanism provoked by the hadronic interactions because it can identify the particle species in a wide transverse momentum range. The covering transverse momentum range is down to ~ 0.1 GeV/c and up to several dozen GeV/c with the particle identification. In particular, neutral mesons can be measured up to ~ 100 GeV/c with its identification. The capabilities are important to study the particle production mechanism because the mechanism in the low and high transverse momentum region is different as well as the particle contents.

The particle production is divided into two processes, "soft" and "hard" processes, roughly. The soft process dominates low transverse momentum phenomena and the other hard process does high transverse momentum phenomena. The mechanism of high transverse momentum particle production can be calculated with the perturbative QCD (pQCD) because the coupling constant becomes small due to the asymptotic freedom. In contract, in the soft process, the four-momentum transfer is small and the perturbative technique can not be applied to the region, $Q^2 \leq \lambda_{\mathrm{QCD}}$. Therefore, the lattice QCD (lQCD) which is based on the first-principles calculation and the phenomenological approaches has been tried to describe the soft processes.

In the hard process, one important production mechanism is predicted by the pQCD. Almost all particles at high transverse momentum region come from parton fragmentation. However, the prediction suggests there is a certain amount of contribution from the direct production, "Higher-Twist". The particle produced by the higher-twist effect is generated from the quarks in the incident nucleons directly, e.g. $q\overline{q} \rightarrow h$, like the Drell-Yan process.

This process is not considered in general event generator based on the pQCD to estimate the fragmentation function. To understand the particle production mechanism at high transverse momentum region, the measurement of the higher-twist contribution quantitatively is important. Furthermore, the process strongly depends on the parton distribution function in the incident nucleon. Therefore, the investigation of the process contributes to not only expose the particle production mechanism but also to disclose the structure of the nucleon accelerated to the LHC energies.

At LHC collision energies, the multiple parton interactions (MPI) are expected to play an important part in the particle production. The MPI is that the more than one parton pair collides in one nucleon collisions. The MPI significantly affects many physics observables, such as the charged particle multiplicity. In recent years, the charged particle multiplicity in proton+proton collisions at $\sqrt{s} = 7$ TeV achieves up to the multiplicity of peripheral heavy ion (Cu-Cu) collisions at $\sqrt{s_{\mathrm{NN}}} = 200$ GeV. It is expected that these high multiplicity events are related to the MPI. Furthermore, in the high multiplicity events, the particle correlation and collectivity are also observed which is not expected in proton+proton collisions. It is also expected the correlation and collectivity are caused by the MPI. However, these phenomena have been observed in the heavy ion collisions as the QGP signal. These observations suggest that it could be possible that the QGP is formed in proton+proton collisions of high charged particle multiplicity events. Therefore, the charged particle multiplicity dependence of the particle production is expected to give an important piece of information to new phenomena observed in high multiplicity events at LHC.

In this thesis, the higher-twist contribution and the evolution of the particle production by the soft and hard processes with the event charged particle multiplicity at mid-rapidity in proton+proton collisions at $\sqrt{s} = 8$ TeV is studied through the neutral pion. In order to enhance the small cross-section event, the method to trigger the rare event which exhibits a very high transverse momentum photon plentifully is established. Owing to the trigger capability, the contribution of higher-twist production is verified precisely with the high transverse momentum neutral pion. This result gives the important insight of the parton distribution function in the nucleon accelerated to the LHC energies. Observing the particle production as a function of the charged particle multiplicity reveals that the contribution of different momentum particle to the overall charged particle multiplicity. Furthermore, the comparison of evolution as a function of the charged particle multiplicity gives insights of the underlying multiple parton interactions phenomena.

This thesis is structured as follows: Chapter 2 reviews theoretical models and experimental observations related to the particle production in hadronic collisions. In general, the particle production induced by hadronic collisions is described by a combination of three parts, the parton distribution function in the hadron, the QCD subprocess, and the fragmentation. In addition to the mechanism, the higher-twist production is also introduced. Furthermore, the MPI phenomena are also discussed while reviewing the recent experimental results, in particular, the small collision systems at LHC. Chapters3 briefly describe the LHC and the ALICE experiment. The acceleration chain of the LHC for protons and heavy ions and then the ALICE experiment overview are introduced. Then, each sub-system detector and its trigger system, as well as offline software system installed in the ALICE experiment, are explained briefly. Chapter 4 is devoted to the analysis procedure. The procedure is divided into two sections, one is the reference cross section measurement Section 4.1.4 and the other is the neutral pion measurement Section 4.3.3. The reference cross section measurement is the most basic measurement for experiments and is used in not only this thesis but also the whole ALICE measurements in proton+proton collisions at $\sqrt{s} = 8$ TeV. The specific triggered data analysis method is also explained as well as the neutral pion reconstruction. Then, the correction factors for calculation of the invariant cross-section and systematic uncertainties are discussed. In Chapter 5 shows the measurement this thesis results, the invariant cross-section of the neutral pion as a function of the charged multiplicity. The ALICE experiment can measure the neutral pion with the different sub-systems. They are summarized briefly and

then combined with this thesis result. The comparison with the theoretical calculation and the other collision energies are discussed in Chapter 6. The higher-twist contribution is studied with two methods quantitatively. Furthermore, the evolution of the neutral pion yield with the charged particle multiplicity is shown and compared with the theoretical calculation. From the measurements, the MPI phenomena are found out and discussed. Finally, Chapter 7 is devoted to the conclusion of this thesis.

Chapter 2

Theoritical and Experimental Background

In this chapter, the theoretical and experimental backgrounds related to particle production mechanisms in high energy hadronic collisions are reviewed. First of all, the basic concepts of the standard model of particle physics are described in Section 2.1. Among the model, the strong interaction plays an important role in the particle production in hadronic collisions. Therefore, the detailed introduction of Quantum Chromodynamics (QCD) which describe the strong interaction is put in Section 2.2. Further detail of the particle production via parton fragmentation is discussed in Section 2.3 and it is separated into three components, parton distribution function, elementary QCD subprocess and fragmentation function. These three components are addressed in Section 2.3.2 to Section 2.3.4. In addition to the fragmentation, the direct hadron production is predicted by the QCD and it is introduced in Section 2.3.5. Furthermore, the multiple parton interaction which is a key phenomenon at LHC is introduced in Section 2.4.

2.1 Standard Model of Particle Physics

The Standard Model of particle physics (SM) is the theory that describes the electromagnetic, weak and strong interactions among the elementary particles. These three interactions, together with the gravitation interaction which is not included in the SM, describe the all known interactions.

In the SM, each interaction is mediated by the force carriers, Gauge-Boson. The strong interaction between color-charged particles is mediated by eight gluons that carry combinations of color charges. The electromagnetic interaction between charged particles is mediated by photons. The weak interaction between particles of different flavors is mediated by the massive particles $W^{\pm}$ and Z^0. It is expected that the gravitation interaction between particles with a mass is mediated by the graviton, but up to now, it has not been observed yet.

In the SM, there are elementary particles which make up the material in the universe besides the gauge bosons of the interactions, so-called quarks and leptons of which spins are $\frac{1}{2}$. The quarks and leptons are divided into three categories called generations. Each generation contains two quarks or leptons. In quark sector, first generation has up (u) and down (d) quarks, the second generation contains charm (c) and strange (s) and the third generation is top (t) and bottom (b). For each quark, there is the anti-quark which has the same mass, opposite electric charge, and opposite baryon number. In lepton sector, each generation comprises the electron (e), the muon (μ) and the tau (τ) of which the charges are $-e$. In addition to the charged leptons, each generation has neutral leptons, the electron neutrino (ν_e), the muon neutrino (ν_μ) and the tau neutrino (ν_τ). Anti-leptons also exist as well as the quarks, same mass, opposite

electric charge and opposite lepton number. The quarks and leptons are summarized in Table 2.1 together with their electrical charge and mass.

Three generations of matter (fermions)

	I	II	III		
Mass: Charge: Spin: Name:	2.5 MeV 2/3 1/2 **u** up	1.3 GeV 2/3 1/2 **c** charm	173 GeV 2/3 1/2 **t** top	0 0 1 **g** gluon	125 GeV 0 0 **H** Higgs
	5 MeV -1/3 ½ **d** down	100 MeV -1/3 ½ **s** strange	4.2 GeV -1/3 ½ **b** bottom	0 0 1 **γ** photon	
	< 2 eV 0 1/2 **ν**e Electron neutrino	<0.2MeV 0 1/2 **ν**μ muon neutrino	<18MeV 0 1/2 **ν**τ tau neutrino	91 GeV 0 1 **Z** z boson	
	0.5 MeV -1 1/2 **e** electron	105 MeV -1 1/2 **μ** muon	1.8 GeV -1 1/2 **τ** tau	80.4GeV ±1 1 **W** w boson	

Figure 2.1: Table of the elementary particles and their mass, spin and charge as described in the standard model of particle physics.

The particles made of quarks are called hadrons. The hadrons are divided into mesons and baryons. The mesons consist of two quarks, a pair of quark and anti-quark. Hence, the baryon number is 0. The baryons are comprised of three quarks, three quarks or anti-quarks and so the baryon number is 1 and -1, respectively.

Furthermore, the standard model predicts the existence of the Higgs boson. The Higgs is introduced to explain why the weak bosons are massive. The mass of the Higgs boson cannot be calculated by the SM. Its mass is a parameter which is determined by only the experiments. It had been searched for a long time and finally, it has been discovered at the LHC experiments in 2012 [3, 4]. It is expected that the particle is the SM Higgs boson, but further data analysis is needed. The all elementary particles predicted by the SM are completed by the discovery.

The SM is very successful in describing many phenomena of the elementary particles induced by three interactions. However, there are still phenomena which are not explained by the SM. The biggest issue is that the SM does not include the gravitation interaction. The dark matter and dark energy cannot be explained by the SM. Also, the SM can not explain the large asymmetry between matter and anti-matter as it is observed in the universe. Furthermore, in the SM, the mass of neutrinos is 0. However, the neutrino oscillation has been discovered and this indicates that the neutrino mass is larger than 0 [9].

To solve the problems introduced above, it has been tried to extend the SM for a long time. For example, the super-symmetric theory (SUSY) which predicts that each fermion and each boson in the SM has a super-symmetric partner is introduced [10]. The string theory is also introduced to solve the problems, in particular, to combine the quantum mechanics with the general relativity. Evidence for these "beyond standard models" are investigated in proton+proton collisions at the LHC.

2.2   Quantum ChromoDynamics (QCD)

2.2.1   Concept

The Quantum Chromodynamics (QCD) is the theory describing the kinematics induced by the strong interaction. It is founded on the gauge field theory of SU(3) component, SU(3)×SU(2)×SU(1). The strong interaction is mediated by gluons coupling with particles which have a color charge. Gluon carries a combination of the color and unti-color charges. Hence, the gluons can couple with gluons. This is in contrast to Quantum Electrodynamic (QED) which describes the kinematics induced by the electromagnetic interaction. The QED describes the interaction between particles which have a charge with photons. Photons do not have a charge and so photons do not interact with photons. The characteristic property of the QCD leads complex phenomena of the particle physics. This is the most important difference between QCD and QED.

The QCD lagrangian density is described as

$$\mathscr{L} = \overline{\psi}_{q,a}\big(i\gamma^\mu\partial_\mu - m_q\big)\psi_{q,a} + g_s\overline{\psi}_{q,a}\gamma^\mu T_C\mathcal{A}^C_\mu\psi_{q,a} - \frac{1}{4}F^a_{\mu\nu}F^{\mu\nu}_a \tag{2.1}$$

where the γ^μ is the Dirac $\gamma-$matrix, $\psi_{q,a}$ quark-field spinors for a quark of flavor q and mass m_q with color index a which is $a = 1$ to $N_c = 3$, there is 3 color quarks. The $\mathcal{A}^C_\mu$ is the gluon field with C which is from $C = 1$ to $N^2_C - 1 = 8$, there are 8 color gluons and T_a are the eight generators of SU(3). The first term is the Dirac equation and expresses a free (non-interacting) quark. The second term expresses interactions between quarks and gluons with one vertex connecting to two quarks and one gluon. The color state of quarks is changed by interaction with a gluon. There are no interactions between only quarks. The interactions have to include at least one gluon. The squared field strength tensor describing the dynamics of the gauge field is described in the third term

$$F^A_{\mu\nu} \;\; = \;\; \partial_\mu\mathcal{A}^A_\nu - \partial_\nu\mathcal{A}^A_\mu - g_sf_{ABC}\mathcal{A}^B_\mu\mathcal{A}^C_\nu, \quad\;\; [T^A, T^B] = if_{ABC}T^C, \tag{2.2}$$

where f_{ABC} is the structure constants of SU(3). In the field strength tensor, the first and second terms express the kinetics of a massless vector field which is similar to the QED. The final term is the particular part of the QCD required by the gauge invariance. It leads to three or four gluon vertices as followings.

- Three gluon interaction

$$-\frac{g}{2}f_{ABC}\big(\partial^\mu\mathcal{A}^A_\nu - \partial^\nu\mathcal{A}^A_\mu\big)\mathcal{A}^B_\mu\mathcal{A}^C_\nu. \tag{2.3}$$

- Four gluon interaction

$$-\frac{g^2}{4}f_{ABC}f_{CDE}\mathcal{A}_{A\mu}\mathcal{A}_{B\nu}\mathcal{A}^\mu_C\mathcal{A}^\nu_D. \tag{2.4}$$

This is completely different from the QED because there is no direct interaction between the gauge bosons (photons). The final term leads that gluons are massless, but the strong interaction is short range force and furthermore, the asymptotic freedom is predicted by the term.

The strength of the interaction is described by the coupling constant. In case of the strong interaction, it is indicated by α_s. The coupling constants are represented with a renormalization scale μ^2_R and it meets the requirement of the renormalization group equation as follows.

$$\mu_R\frac{\partial\alpha_s(\mu_R)}{\partial\mu_R} = \beta\big(\alpha_s(\mu_R)\big) = -\frac{\beta_0}{2\pi}\alpha^2 - \frac{\beta_1}{4\pi^2}\alpha^3 + \frac{\beta_2}{64\pi^3}\alpha^4 + \cdots, \tag{2.5}$$

where β is a beta function. Conventionally, for the estimation of α_s, the four-momentum transfer Q of a given process is chosen to the renormalization scale. In consequence, it is found
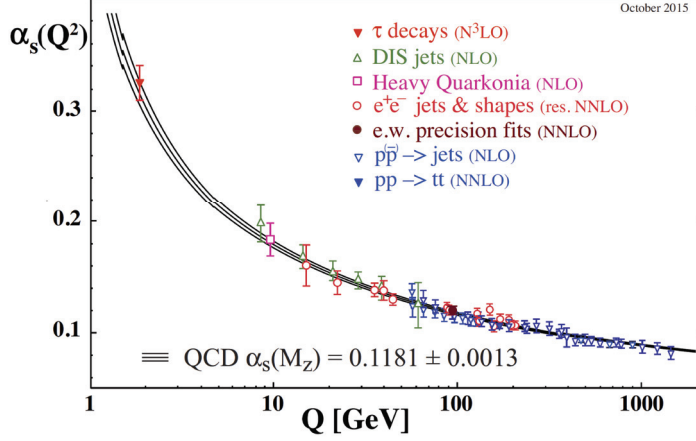
Figure 2.2: The measured and calculated running coupling constant of strong force as a function of the four momentum transfer Q [11].

that α_s strongly depends on Q. The dependence on Q of α_s has been measured by several experiments and the results are shown in Figure 2.2. For large Q, the α_s can be approximated as

$$\alpha_s(Q^2) \approx \frac{12\pi}{(33 - 2n_f)\ln(Q^2/\Lambda_{\mathrm{QCD}}^2)}. \tag{2.6}$$

In this formula, n_f is the number of active quark flavors. The equation introduces the free parameter of Λ_{QCD} called the QCD scale. It can not be obtained by calculations and is evaluated by comparing experimental results with the equation. The value is found to be $\Lambda_{QCD} \sim 200$ MeV.

The coupling constant becomes weaker with increasing momentum transfer. It approaches 0 asymptotically at large four-momentum transfer. This specific character is not seen in the other interactions and it is called "asymptotic freedom". On the other hand, at low four-momentum transfer, the coupling constant increases. Therefore, the perturbative technique cannot be applied to processes with low four-momentum transfer around $Q \approx \Lambda_{\mathrm{QCD}}$.

A phenomenological potential between two quarks as a function of the distance r is given as

$$V_s(r) = -\frac{4}{3}\frac{\alpha_s \hbar c}{r} + kr. \tag{2.7}$$

The potential between two quarks does not vanish for large distances r but becomes large with r. The fact indicates that quarks can never be separated from each other. If the quarks are pulled apart from each other, the energy between the quarks increases until it is energetically more favorable to generate a new pair of quark and anti-quark out of the energy of the string between the quarks. This effect explains why quarks and gluons have not yet been observed as free particles. The effect that two quarks cannot be separated easily is called "color confinement".

2.2.2 Lattice QCD

As explained above, the growth of coupling constant at low four-momentum transfer prohibits applying the perturbative approach. The most effective solution of the problem is the lattice QCD based on the first-principles calculation. In the lattice QCD, four-dimensional Euclidean space-time is discretized into a hypercubic lattice with spacing a, with quark fields and gauge fields placed on sites and links between sites, respectively. The action S is defined on the lattice and the observables are calculated averaging over all the possible configurations of the fields on the lattice. Real physical quantities are obtained by vanishing lattice space ($a \to 0$).

It took an enormous amount of time to obtain real physical quantities with the lattice QCD in the past. However, in recent year, the lattice QCD can reproduce the real physics quantities, e.g. hadron masses within 1% level, due to mushroom development of computers and calculation techniques. The masses of hadron which consists of light quarks (u,d and s) calculated by the lattice QCD is shown in Figure 2.3.

For the most part of hadron mass is generated by the strong interaction. For example, the proton mass is 938 MeV/c^2 and it consists of two u and one d. The masses of u and d by the Higgs mechanism are found to be ~ 2 MeV/c^2 and ~ 5 MeV/c^2, respectively. The total mass of quarks in a proton is only ~ 9 MeV/c^2 and so the rest of proton mass as equal to about 99% is generated by the strong interaction. The mechanism to generate almost all hadron mass is explained by Chiral Symmetry Spontaneously Breaking [22]. As shown in Figure 2.3, the lattice QCD can reproduce this inherent phenomenon of the strong interaction. The lattice QCD is expected to be the very useful tool to understand the QCD which is the complex theoretical system.
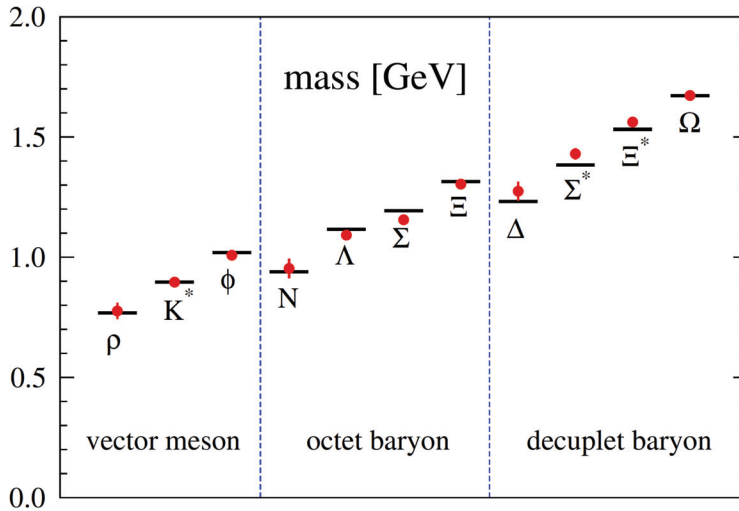

Figure 2.3: Measured and calculated by the lattice QCD hadron masses [11]. The masses of u and d are assumed to be same.

2.2.3 QCD Matter Phase Diagram

The phase diagram of the QCD matter as a function of net baryon density and temperature (T) predicted by lattice QCD is shown in Figure 2.4. Under low temperature and low baryon density condition, quarks and gluons are confined into hadrons. The condition is described as "Hadronis" and the universe around us is under the condition. The lattice QCD predicts that at low temperature and high baryon density conditions which are expected to be formed in a neutron star, the matter is described as a degenerated gas of neutrons. In low temperature and

very large baryon density ($\mu_{\rm B} \to \infty$) environments, a color superconducting matter in which the quarks forms color Cooper pairs is expected to exist [13].
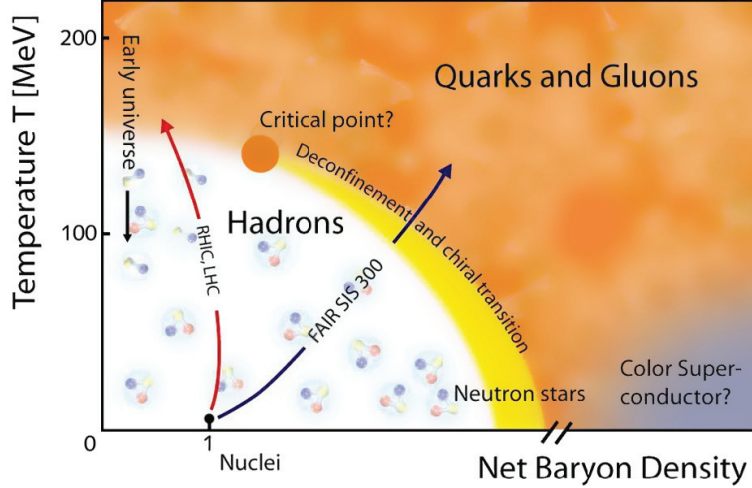

Figure 2.4: The QCD phase diagram as a function of baryon density and temperature. The arrows indicate the regions of the phase diagram that the experiments can explore [12].

The deconfined state of quarks and gluons is predicted by the discovery of the asymptotic freedom before establishing lattice QCD. The state in which quarks and gluons move freely is formed under high-temperature environment and it called Quark-Gluon Plasma (QGP). The equation of state of QGP and the transition from the hadronic matter to a deconfined state can be evaluated by lattice QCD. Lattice QCD predicts also that the transition of the hadronic matter to QGP is associated to the chiral symmetry restoration simultaneously because the chiral condensate decreases due to quarks moving freely. The prediction indicates that mass of hadrons in QGP is different from the mass in the hadronic matter.

When the baryon density is 0, the critical temperature of transition from hadronic phase to the deconfined phase is predicted as $180 < T_{\rm c} < 200$ MeV by lattice QCD. This is corresponding to ~ 1 GeV/fm^3 of the critical energy density. The results of lattice QCD also shows that at the small baryon density region ($\mu_{\rm B} \sim 0$) the transition is a second order phase transition corresponding to a continuous cross-over. The critical point on which first-order phase transition becomes a second order transition is predicted to be $\mu_{\rm B} \sim 0.7$ MeV by lattice QCD.

The QCD phase diagram, especially the phase transition from hadronic matter to the deconfined matter, has been investigated theoretically as well as experimentally. The only tool to create the deconfined matter in the laboratory is heavy-ion collisions at ultra-relativistic energies. If the energy density is achieved the critical density or the temperature exceeds the phase transition temperature, the matter might be formed. Many experiments have tried to attain making the matter at many accelerators and, eventually, many pieces of evidence have been observed at the Relativistic Heavy Ion Collider (RHIC) at Brookhaven National Laboratory (BNL) [14, 15, 16, 17, 18] in the beginning of 2000's [19]. The pieces of evidence which indicate the deconfined matter is a perfect fluid state are found by the experiments placed at RHIC [19]. The search of QGP has been finished by the RHIC experiments and the precise measurement has been started.

2.3   Particle Production in Hadronic Collisions

2.3.1   Factorization Theorem

The high momentum particle production in hadronic collisions at high energies can be described by perturbative QCD with the factorization theorem. The QCD factorization theorem indicates that some processes can be decomposed into independent matrix elements. It is known that the theorem can be applied to the particle production with a high four-momentum transfer in hadronic collisions.

The single hadron production in hadron-hadron hard scattering

$$p_A + p_B \rightarrow h_C + X \tag{2.8}$$

where A and A are the incident hadrons, h_C is outgoing (generated) hadrons and X is anything else, can be described as a parton pair scattering

$$a + b \rightarrow c + x \tag{2.9}$$

where a and b are the incident partons in hadrons A and B, c is a scattered parton which is the origin of hadron h_C. The inclusive hadron h_C production cross section is given by the theorem as

$$\mathrm{d}\sigma^{AB \rightarrow h_C X} = f_a(x_a, \mu_{\mathrm{PDF}}^2) \otimes f_b(x_b, \mu_{\mathrm{PDF}}^2) \otimes \mathrm{d}\hat{\sigma}_{ab \rightarrow cx} \otimes D_c^{h_C}(z_c, \mu_{\mathrm{FF}}^2) \tag{2.10}$$

where $f_a(x_a, \mu_{\mathrm{PDF}}^2)$ and $f_b(x_b, \mu_{\mathrm{PDF}}^2)$ are parton distribution functions which describe the kinematic distribution density for parton a and b with carrying the momentum fractions of x_a and x_b respect to the parent hadrons A and B, $x_{a(b)} = p_{a(b)}/p_{A(B)}$. The term of $\mathrm{d}\hat{\sigma}_{ab \rightarrow cx}(\mu_R^2)$ represents that the cross-section of elementary QCD subprocess of scattering between parton a and b and then at least one parton c is generated. The term of $D_c^{h_C}(z_c, \mu_{\mathrm{FF}}^2)$ is a fragmentation function which expresses the probability that the parton c form an outgoing hadron h_C with a momentum fraction z_c respect to the parent parton c ($z_c = p^h/p^c$). In this formula, the parton distribution function $f(x, \mu_{\mathrm{PDF}}^2)$ and the fragmentation function $D_c^{h_C}(z_c, \mu_{\mathrm{FF}}^2)$ are the long-distance interaction. These functions require experimental inputs and the more details are discussed in Section 2.3.3 for the parton distribution function and Section 2.3.4, respectively. On the other hand, the cross-section with a high four-momentum transfer $\mathrm{d}\hat{\sigma}_{ab \rightarrow cd}$ can be computed by the perturbative QCD. The QCD subprocess is introduced in Section 2.3.2 in more detail.

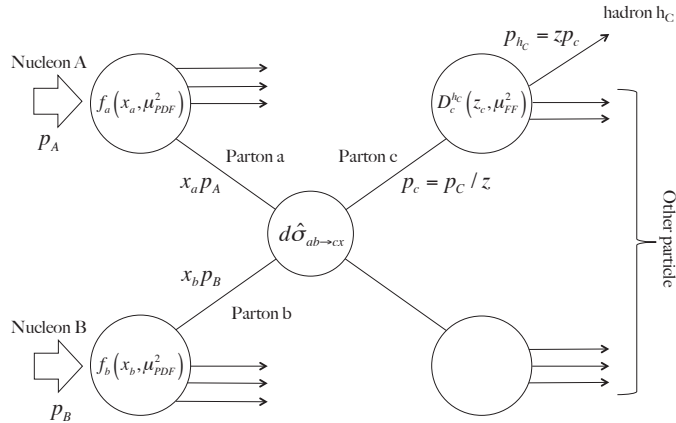Figure 2.5: The total process of generate hadron h_C in nucleus A and B collisions.

2.3.2 The Elementary QCD Subprocesses

The term of $d\hat{\sigma}_{ab\to cx}$ in Equation 2.10 discribes the cross section of subprocess involving partons a and b. The Feynman diagrams of leading-order perturbative QCD related to $a + b \to c + x$ are shown in Figure 2.6. In Figure 2.6, new variables, s, t and u are introduced. These are called Mandelstam variables and they are Lorentz-invariant variables. They can be computed with the initial and final parton momenta as follows.

$$s = (p_a + p_b)^2 = (p_c + p_d)^2 \tag{2.11}$$

$$t = (p_a - p_c)^2 = (p_d - p_b)^2 \tag{2.12}$$

$$u = (p_a - p_d)^2 = (p_c - p_b)^2 \tag{2.13}$$

The cross section of 2→2 processes calculated by the perturbative approach is expressed as

$$d\hat{\sigma}_{ab\to cx} = \mathcal{F} \cdot \left(\overline{\sum} |\mathcal{M}|^2 / g_s^4 \right). \tag{2.14}$$

The subprocesses as a consequence of proton+proton collisions are listed in Table 2.1. In the list, s, t and u are Mandelstam variables and e_q is the charge of the partons. When the subprocess is involving only strong interaction, $\mathcal{F}$ is $\pi\alpha_s^2/s^2$ where α_s is a coupling constant for the strong interaction. On the other hand, in case of the subprocess involving the electromagnetic interaction (last two in the Table 2.1), $\mathcal{F}$ is $\pi\alpha_s\alpha_e/s^2$ where α_e is a coupling constant for the electromagnetic interaction. The $\overline{\sum}|\mathcal{M}|^2/g_s^4$ parts of several 2→2 subprocesses are also summarized in Table 2.1.

Subprocess $ab \to cd$	$\overline{\sum}|\mathcal{M}|^2/g_s^4$
$qq' \to qq'$	$\frac{4}{9}\frac{s^2+u^2}{t^2}$
$qq \to qq$	$\frac{4}{9}\left(\frac{s^2+u^2}{t^2} + \frac{s^2+t^2}{u^2}\right) - \frac{8}{27}\frac{s^2}{tu}$
$q\bar{q} \to q'\bar{q}'$	$\frac{4}{9}\frac{t^2+u^2}{s^2}$
$q\bar{q} \to q\bar{q}$	$\frac{4}{9}\left(\frac{s^2+u^2}{t^2} + \frac{u^2+t^2}{s^2}\right) - \frac{8}{27}\frac{u^2}{st}$
$gq \to gq$	$-\frac{4}{9}\left(\frac{s}{u} + \frac{u}{s}\right) + \frac{s^2+u^2}{t^2}$
$q\bar{q} \to gg$	$\frac{32}{27}\left(\frac{t}{u} + \frac{u}{t}\right) - \frac{8}{3}\frac{t^2+u^2}{s^2}$
$gg \to q\bar{q}$	$\frac{1}{6}\left(\frac{t}{u} + \frac{u}{t}\right) - \frac{3}{8}\frac{t^2+u^2}{s^2}$
$gg \to gg$	$\frac{9}{2}\left(3 - \frac{tu}{s^2} - \frac{su}{t^2} - \frac{st}{u^2}\right)$
$gq \to \gamma q$	$-\frac{1}{3}e_q^2\left(\frac{u}{s} + \frac{s}{u}\right)$
$q\bar{q} \to \gamma g$	$\frac{8}{9}e_q^2\left(\frac{u}{t} + \frac{t}{u}\right)$

Table 2.1: The lowest-order hard scattering subprocesses in QCD for quarks (q) and gluons (g) where q' represents a different flavor quark from q. The s, t and u indicate the Mandelstam variables.

2.3.3 Structure Function in Nucleon

Parton Model and Bjorken Scaling

The internal structure of the proton has been investigated via electron-proton Deep Inelastic Scattering (DIS). The cross-section of the DIS can be described as below.

$$\frac{d^2\sigma}{d\Omega dE'} = \left(\frac{d\sigma}{d\Omega}\right)_{\text{Mott}} \cdot \left[W_2(\nu, Q^2) + 2W_1(\nu, Q^2)\tan^2\frac{\theta}{2}\right] \tag{2.15}$$
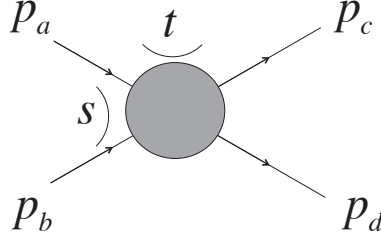
Figure 2.6: Definitions of variables for a two-body final state.

here $(d\sigma/d\Omega)_{\text{Mott}}$ is Mott scattering cross section, $W_1(x, Q^2)$ and $W_2(x, Q^2)$ are structure functions, θ is the scattered angle of the electron with four momentum transfer squared Q^2 and energy loss ν. In the asymptotic limit, $Q^2 \to \infty, \nu \to \infty$ with the ratio Q^2/ν held constant (Bjorken-limit), the structure functions is expressed with new variable x as

$$\nu W_2(Q^2, \nu) = M F_2(x), \quad W_1(Q^2, \nu) = F_1(x) \tag{2.16}$$

where x is called Bjorken-x defined as following

$$x \equiv \frac{Q^2}{2M\nu}. \tag{2.17}$$

Under this limit, the stracture functions have no dependence on Q^2. This scaling behavior is called "**Bjorken-scaling**". This fact that the structure function doesn't depend on the Q^2 indicates that the nucleon consists of point-like charged objects.

Furthermore, if the point-like particle has a spin $1/2$, the structure functions have following relationship (Callan-Gross relationship [20]),

$$2x F_1(x) = F_2(x). \tag{2.18}$$

The ration of $2x F_1/F_2$ has been measured by SLAC-MIT group [21] and the ration is found to be 1 within uncertainties. Therefore, the point-like particle is found to be spin $1/2$. From these results, the fact that a nucleon consists of the point-like particles which have charge and spin $1/2$ is figured out. The point-like particle is named "parton". A model that nucleon consists of partons and Bjorken scaling is applicable is called the "**Parton Model**". As of now, the parton is known as quark and gluon. Furthermore, the scaling is violating due to QCD higher order effects which are explained in more detain in next section.

The variable x has an important relevance to partons in a nucleon as followings. If the fraction of the momentum carried by one parton is ξ ($0 < \xi < 1$), the parton momentum is $p_q \simeq \xi P$ of which P is the nucleon momentum. The fraction of ξ can be converted as below, under the assumption that the partons in a proton don't interact with each other and can move freely in the proton (Pulse approximation).

$$P_q^2 \simeq (\xi P)^2 = (q + \xi P)^2 \tag{2.19}$$

$$\xi \simeq \frac{-q^2}{2P \cdot q} = \frac{Q^2}{2M\nu} = x \tag{2.20}$$

The result means that the variable x is same as the momentum fraction to the total nucleon momentum.

Parton Distribution Function

The Bjorken-scaling is approximate scaling and, in fact, it is violating due to the higher order effects of QCD. The effects can be calculated by perturbative QCD, DGLAP evolution equation

[23, 24]. The equation can extend the function toward Q^2 direction. However, it can calculate the relative value, so at least one data point is needed to estimate the evolution for a given x region.

The structure function as a function of the Q^2 of given x is shown in Figure 2.7. The strike Q^2 dependence is seen in the figure, but perturbative QCD calculation estimates the data very well at all x region.

The structure function can be expressed as

$$F_2(x, Q^2) = x \sum_q e_q^2 \big(f_q(x, Q^2) + \overline{f}_q(x, Q^2)\big) \tag{2.21}$$

where q is a kind of parton and $f_q(x)$ ($\overline{f}_q(x)$) indicates the probability density of the (anti-)parton with the momentum fraction of x. The probability density of the partons with x within a nucleon is called as "**Parton Distribution Functions**". The kind of parton can be gluon, but it can not be measured by DIS because it is the interaction between charged particles. Therefore, the gluon distribution function is extracted indirectly by the fitted results of perturbative QCD. The parton distribution functions of each parton of given Q^2 calculated by MSTW group [25] are shown in Figure 2.8. At very low x region, the gluon contribution becomes very large because gluon is the massless particle and gluon can emit gluons by self-coupling.

The parton distribution functions bounded by a nucleus are modified. The nuclear parton distribution functions (nPDFs) in a nucleus $A(f_q^A(x, Q^2))$ are defined as

$$f_q^A(x, Q^2) \equiv R_q^A(x, Q^2) f_q(x, Q^2) \tag{2.22}$$

where $R_q^A(x, Q^2)$ is the nuclear modification factor which represents the difference of parton distribution function between in a free nucleon and a nucleon bounded by a nucleus. An illustration of the nuclear effects $R_q^A(x, Q^2)$ as a function of x is shown in Figure 2.9. There are four effects to modify the distribution. At low x region ($x < 2 \times 10^{-2}$), the parton density in a nucleus is smaller than free nucleons due to the shadowing effect [26]. The shadowing effect is understood as interactions between partons in different nucleons. Gluons with small x overlap with other gluons in different nucleons and then the gluons can disappear by the pair annihilation. Hence, the parton density in a nucleus is smaller than free nucleons. In contrast, at high x ($2 \times 10^{-2} < x < 2 \times 10^{-1}$), the parton density in a nucleus is larger than a free one, which is called anti-shadowing effect [26]. Due to momentum conservation, the reduction of the small x partons leads the enhancement of the large x partons. Therefore, partons with these region increase in a nucleus. Even higher x, the EMC effect is seen and it affects to decrease the density in a nucleus again. Indeed, the origin of the EMC effect is still not understood [27]. The European Muon Collaboration (EMC) has observed the effect [28] and so it is named the EMC effect. Finally, there is the Fermi motion effect [29]. The parton around $x \sim 1$ vanishes in free nucleons, but nucleons bounded by a nucleus are moving known as the Fermi motion. Thus, the nuclear modification factor becomes large. The nuclear modification factors for a lead nuclear parametrized by EPS09 collaboration [26] of give four-momentum transfers for valence quarks (R_V^{Pb}), sea quarks (R_S^{Pb}) and gluons (R_G^{Pb}) are shown in Figure 2.9.

2.3.4 Jet and Fragmentation Function

Jet

The scattering between partons with the high four-momentum transfer Q^2 causes two back-to-back partons which have same energy (Figure 2.10). The scattered parton has a color, but it cannot exist freely due to the color confinement which allows only color-singlet. The colored parton generates the other colored parton to create color-singlet bound states, e.g. hadrons. Therefore, the initial scattered parton forms the group of the hadrons along the scattered
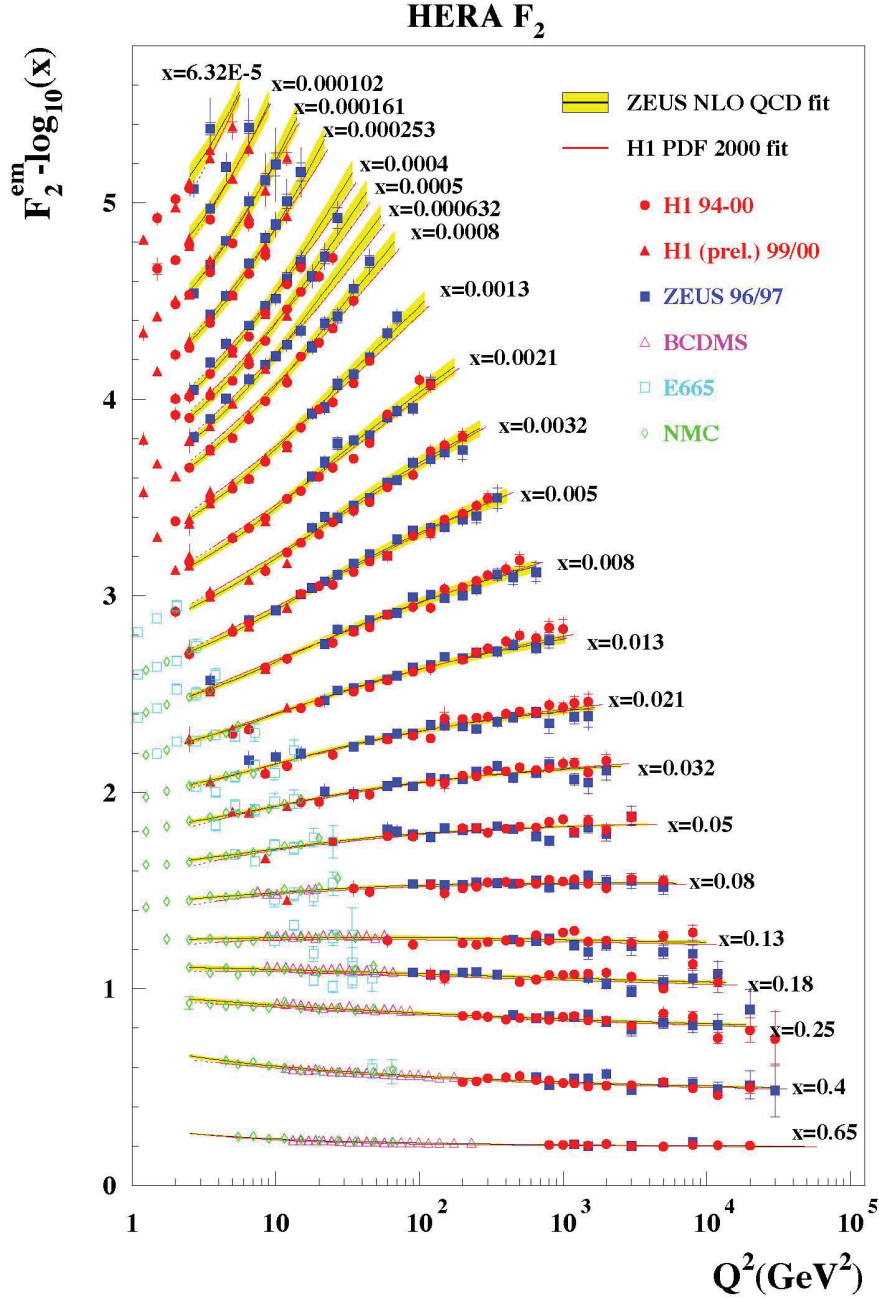
Figure 2.7: The stracture function as a function of Q^2 of each x measured by H1 [94, 95], ZEUS [96], BCDMS [97] and NMC [98]. At high x region the stracture function decreases with larger Q^2. In contrast, at low x region, the larger Q^2, the larger value. The band is calculated result of the perturbative QCD with DGLAP evolution equation.
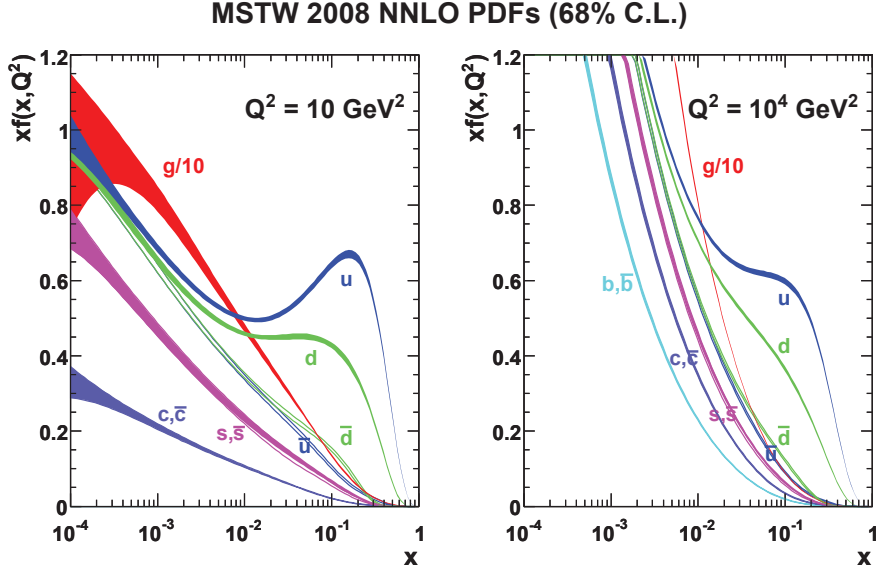
Figure 2.8: The parton distribution function of each parton including gluon calculated by NNLO pQCD with DGLAP revolution equation [25].

direction. The hadron group along the initial scattered parton is called "**Jet**". The longitudinal momentum of each hadron $p_{||}^h$ is proportional to the scattered parent parton momentum. On the other hand, the transverse momentum of each hadron p_T^h has about ~300 MeV fluctuations caused by the uncertainty principle.

The jets are classified by two types, quark jet and gluon jet. When the first scattered parton is a quark, the consequence is quark jet and the other case is a gluon jet. The radius of gluon jet is wider than the quark jet due to the Casimir factor. It is from the magnitude of color charge. The Casimir factors of gluon and quark are $C_A = 3$ and $C_F = 4/3$, respectively. Therefore, it is easier to generate new gluons for gluons than quarks. As a result of this, the gluon jet has the wider radius and more particles than the quark jet. At LHC collision energies, QCD jet is almost gluon jet because first scattered parton depends on the PDF. (Section 2.3.3).

Fragmentation Function

The scattered parton decay into many hadrons and form a jet as explained above. The process in which a parton forms hadrons is called "**Hadronization**". This process is described by "**Fragmentation Function (FF)**", $D_f^h(z)$, which is the probability distribution for a hadron h carrying a momentum fraction of

$$z_T = \frac{p_T^h}{p_T^f} \tag{2.23}$$

where p_T^h is each hadron momentum and p_T^f is the initial parton momentum. The fragmentation function has a following relational expression due to the momentum conservation.

$$\sum \int z D_f^h(z, \mu^2) \mathrm{d}z = 1 \tag{2.24}$$

The fragmentation function has been measured by the previous experiments with e^+e^- colliders via the process of $e^+e^- \to \gamma^*/Z \to q\bar{q} \to h + X$. In case of back-to-back jet (di-jet) event, the
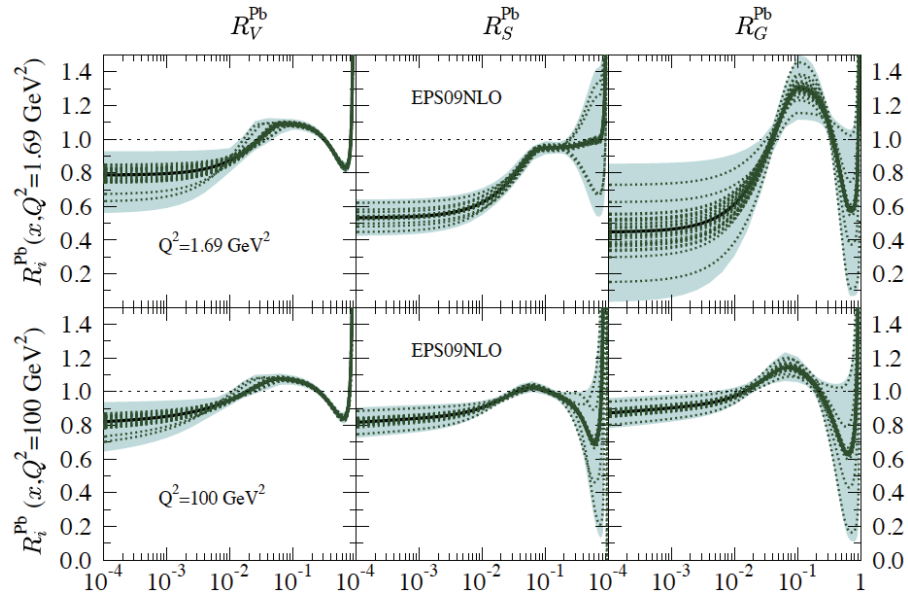
Figure 2.9: The nuclear modification factos in lead for valence, sea quarks and gluons at the given four-momentum transfer calculated by EPS09 [26].
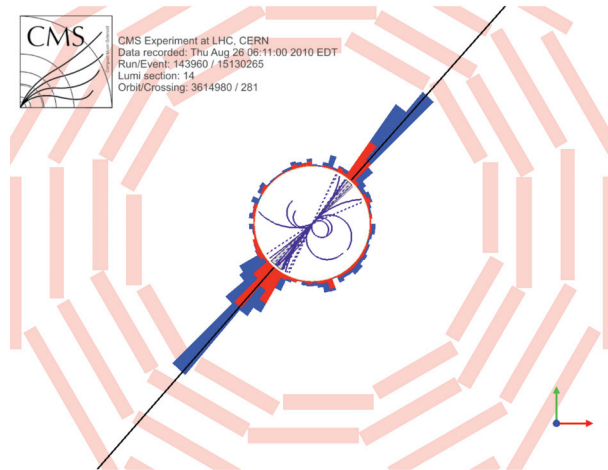

Figure 2.10: Jet event display in proton+proton collisions at $\sqrt{s} = 7$ TeV by the CMS collaboration [30].

fragmentation function from a quark to hadrons can be measured. While the fragmentation function of gluon to hadrons can be measured via the three jets event. However, the three jet event is the rare event in previous e^+e^- collider experiments, hence the measurement of gluon to hadron fragmentation function is the important subject of study. The scale dependence of fragmentation function can be described with DGLAP equation [23, 24] as well as the parton distribution function.

The inclusive single particle transverse momentum spectrum from jet fragmentation is dominated by the fragmentation with large z_T because the scattered parton transverse momentum spectrum decreases steeply in a power-law function (Section 2.3.2). The cross-section of the inclusive single hadron is described as

$$\frac{1}{\hat{p_\mathrm{T}}}\frac{\mathrm{d}^2\sigma_h(\hat{p_\mathrm{T}}, z_\mathrm{T})}{\mathrm{d}\hat{p_\mathrm{T}}\mathrm{d}z_\mathrm{T}} = \frac{1}{\hat{p_\mathrm{T}}}\frac{\mathrm{d}\hat{\sigma}}{\mathrm{d}\hat{p_\mathrm{T}}} \times D_f^h(z_\mathrm{T}) \tag{2.25}$$

$$= f(\hat{p_\mathrm{T}}) \times D_f^h(z_\mathrm{T}) \tag{2.26}$$

where p_T is the hadron transverse momentum, $\hat{p_\mathrm{T}}$ is the initial parton transverse momentum which is also jet transverse momentum ($\hat{p_\mathrm{T}} = p_\mathrm{T}^{Jet}$), $f(\hat{p_\mathrm{T}}) = \mathrm{d}\hat{\sigma}/\hat{p_\mathrm{T}}\mathrm{d}\hat{p_\mathrm{T}}$ represents the scattered parton spectrum and $D_f^h(z_\mathrm{T})$ indicates the fragmentation function for the parton f to hadron h with the fragmentation variable $z_\mathrm{T} = p_\mathrm{T}/\hat{p_\mathrm{T}}$. The Equation 2.26 can be changed by simple variable deformation as follows.

$$\frac{1}{p_\mathrm{T}}\frac{\mathrm{d}^2\sigma_h(p_\mathrm{T}, z)}{\mathrm{d}p_\mathrm{T}\mathrm{d}z} = f\left(\frac{p_\mathrm{T}}{z}\right) \times D_f^h(z) \times \frac{1}{z^2} \tag{2.27}$$

The final inclusive single hadron can be found within $p_\mathrm{T} < \hat{p_\mathrm{T}} < \sqrt{s}$ which is corresponding to the value of $x_\mathrm{T} = 2p_\mathrm{T}/\sqrt{s}$ to 1. Therefore, the final inclusive spectrum as a function of its transverse momentum can be calculated as

$$\frac{1}{p_\mathrm{T}}\frac{\mathrm{d}\sigma_h}{\mathrm{d}p_\mathrm{T}} = \int_{x_\mathrm{T}}^1 f\left(\frac{p_\mathrm{T}}{z}\right)D_f^h(z)\frac{\mathrm{d}z}{z^2}. \tag{2.28}$$

The parton scattering cross section in hard process can be calculated with the perturbative technique (Section 2.3.2) and it is expressed as

$$\frac{1}{\hat{p_\mathrm{T}}}\frac{\mathrm{d}\sigma_f}{\mathrm{d}\hat{p_\mathrm{T}}} = f(\hat{p_\mathrm{T}}) = A \cdot \left(\frac{1}{\hat{p_\mathrm{T}}}\right)^n \tag{2.29}$$

where A is a constant and n is a power-law variable and depends on the subprocess. From above formulas, final inclusive single-particle spectrum can be estimated as

$$\frac{1}{p_\mathrm{T}}\frac{\mathrm{d}\sigma_h}{\mathrm{d}p_\mathrm{T}} = \int_{x_\mathrm{T}}^1 A \cdot D_f^h(z)\left(\frac{p_\mathrm{T}}{z}\right)^{-n}\frac{\mathrm{d}z}{z} \tag{2.30}$$

$$= \frac{1}{p_\mathrm{T}^n}\int_{x_\mathrm{T}}^1 A \cdot D_f^h(z)z^{n-2}\mathrm{d}z. \tag{2.31}$$

The last integral in Equation 2.31 depends only on the hadron momentum p_T because of the small x_T. Furthermore, Equation 2.31 is also indicating that the measured inclusive single particle is affected by the factor of z^{n-2}. From this point, the inclusive single-particle spectrum carries the major portion of its parent parton momentum.

2.3.5 x_T Scaling and Higher-Twist Process

In the conventional pQCD calculation, the hard subprocess invariant cross section in the factorized form (Equation 2.10) is expressed as

$$E\frac{\mathrm{d}^3\sigma^{ab\to cd}}{dp^3} = \frac{\mathrm{d}^3\sigma^{ab\to cd}}{p_\mathrm{T}\mathrm{d}p_\mathrm{T}\mathrm{d}y\mathrm{d}\phi} = \frac{1}{p_\mathrm{T}^{n_{\mathrm{eff}}}}F\left(\frac{p_\mathrm{T}}{\sqrt{s}}\right) \tag{2.32}$$

where F is the dimensionless scaling function. The parameter n_{eff} is influenced by the number of elementary fields (active fields) which are participating the hard subprocess, n_{active}, and expressed as

$$n_{\text{eff}} = 2n_{\text{acvive}} - 4. \tag{2.33}$$

For example, in case of the leading-twist $(2 \to 2)$ subprocess (Figure 2.11(a)), the number of participating active field is 4 and the n_{eff} is calculated as $2\times4-4=4$.

The invariant cross section (Equation 2.32) multiplied by $\sqrt{s}^{n_{\text{eff}}}$ can be deformed as

$$\sqrt{s}^{n_{\text{eff}}} E\frac{d^3\sigma^{ab\to cd}}{dp^3} = \left(\frac{\sqrt{s}}{p_{\text{T}}}\right)^{n_{\text{eff}}} F\left(\frac{p_{\text{T}}}{\sqrt{s}}\right) \tag{2.34}$$

$$= \left(\frac{2}{x_{\text{T}}}\right)^{n_{\text{eff}}} F'(x_{\text{T}}) = G(x_{\text{T}}) \tag{2.35}$$

with new parameter of $x_{\text{T}} = 2p_{\text{T}}/\sqrt{s}$. The Equation 2.35 indicates that the invariant cross-section multiplied by the $\sqrt{s}^n$ depend on only x_{T} and not the collision energy. This scaling is called "$\mathbf{x_T}$ **scaling**". In the figure, the multiplied invariant cross sections at high transverse momentum region are consistent with each other. The lower transverse momentum region, the scaling is violated due to soft QCD effect.
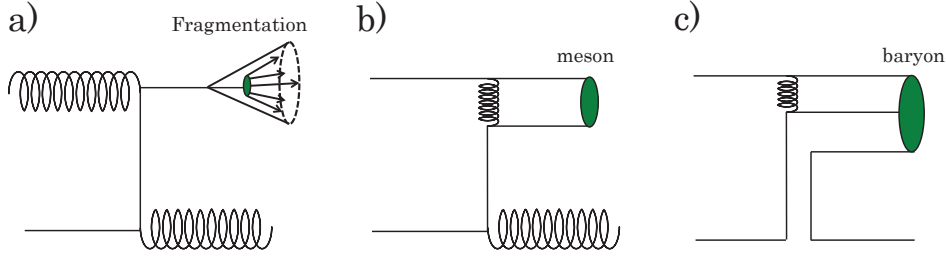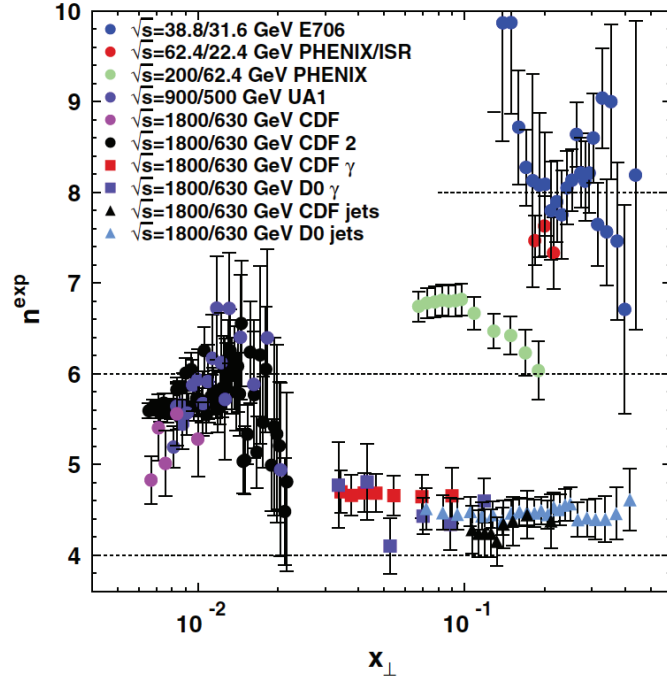

Figure 2.11: The Feynman diagrams: (a) the leading-twist subprocess for jet production, (b) the higher-twist process for meson production, (c) the higher-twist process for baryon process.

The production of a hadron with a large transverse momentum in several hadronic collisions is assumed to arise from the leading-twist subprocess. However, one more mechanism, **Higher-Twist**, contributes the high transverse momentum hadron production. The mechanism produces hadrons without any fragmentations. The process produces hadrons directly in the hard subprocess and its diagram is shown in Figure 2.11(b). The number of participating active fields in the higher-twist process is different from the leading-twist process. Therefore, the n_{eff} of the higher-twist process is different from the leading-twist process.

The n_{eff} can be obtained by comparing two different collision energies, $\sqrt{s_1}$ and $\sqrt{s_2}$, with Equation 2.35 and it is found to be

$$n_{\text{eff}}(x_{\text{T}}, \sqrt{s_1}, \sqrt{s_2}) = -\frac{\ln\left[\sigma^{\text{inv}}(x_{\text{T}}, \sqrt{s_1})/\sigma^{\text{inv}}(x_{\text{T}}, \sqrt{s_2})\right]}{\ln\left[\sqrt{s_2}/\sqrt{s_1}\right]} \tag{2.36}$$

where σ^{inv} indicates the invariant cross section. In case of the leading-twist process, as written above, n_{eff} is found to be $n_{\text{eff}} = 4$. On the other hand, for the higher-twist process, it is found to be $n_{\text{eff}} = 6$ for mesons and $n_{\text{eff}} = 8$ for baryons becuase the number of active fields is $n_{\text{active}} = 5$ and $n_{\text{active}} = 6$, respectively, as shown in Figure 2.11(b)(c).

The n_{eff} of hadrons, direct γ and jet in proton-(anti)proton collisions measured by previous experiments are shown in Figure 2.12. The isolated photon, as well as jet productions, are

originated from the leading-twist process. Therefore, their n_{eff} should be $n_{\text{active}} = 4$. However, the isolated photon and jet results are $n_{\text{eff}} \simeq 4.5$. This is slightly larger than the LO-pQCD expectation because there are several effects which are not considered in LO-pQCD, e.g., the intrinsic partonic transverse momentum, the QCD running coupling constant, scaling violation of the parton distribution function and the fragmentation function. The deviation is expected as $\delta = \mathcal{O}(1)$ by NLO-pQCD calculations [31]. On the other hand, the hadron results are $n_{\text{eff}} = 5 \sim 6$ and larger than the isolated photon and jet results. The higher value of the n_{eff} than direct phton as well as jet indicates the presence of the higher-twist process.

Figure 2.12: The Feynman diagrams: (a) the leading-twist subprocess for jet production, (b) the higher-twist process for meson production, (c) the higher-twist process for baryon process [31].

2.4 Multiple Parton Interaction (MPI)

2.4.1 Concept

The phenomenon that more than one parton pair takes part in one event is called "**Multi Parton Interaction (MPI)**". The occurrence of the MPI depends strongly on the density of partons inside the colliding hadrons. At the LHC, the particles originating from small x partons are dominant. The smaller x becomes, the larger parton density becomes. Consequently, the MPI at LHC is expected to play the more important role than previous experiments.

The simplest MPI interaction is called Double Parton Scattering (DPS) and its Feynman diagram is illustrated in Figure 2.13. The DPS cross section is calculated with the Single Parton Scattering (SPS) cross section by

$$\sigma_{A+B}^{\text{DPS}} = \frac{m}{2} \frac{\sigma_A^{\text{SPS}} \sigma_B^{\text{SPS}}}{\sigma_{\text{eff}}} \tag{2.37}$$
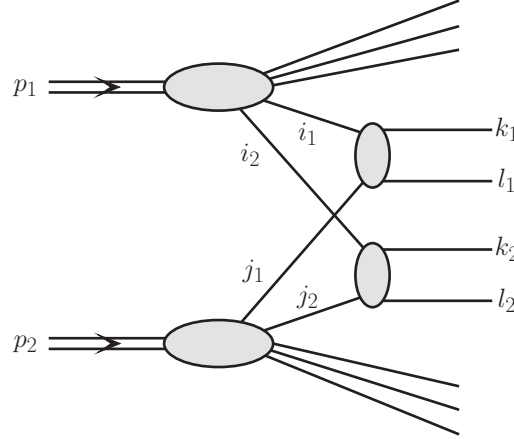
Figure 2.13: Mechanism of Double Parton Scattering in which the partons of the first proton are labelled i_1 and i_2 and of the second proton j_1 and j_2. The two hard scattering subprocess are A($i_1 j_1 \rightarrow k_1 l_1$) and B($i_2 j_2 \rightarrow k_2 l_2$) [32].

where $\sigma_{A+B}^{\mathrm{DPS}}$ indicates the cross-section of the occurrence of independent process A and B simultaneously, $\sigma_{A}^{\mathrm{SPS}}$ and $\sigma_{B}^{\mathrm{SPS}}$ are the cross-section of the independent SPS processes A and B, the factor m indicates the distinctness from the final states and σ_{eff} is the effective cross-section makes a quantitative prediction of the transverse distribution of partons in a hadron collision.

The MPI depends on not only the longitudinal momentum fraction of the two partons (x_1 and x_2), but also the transverse distance between the two partons **b**. The probability density including the momentum fraction and distance between partons is called the double (multi) parton distribution. The double parton distribution is written as

$$F(x_1, x_2, \mathbf{b}) = f(x_1)f(x_2)G(\mathbf{b}) \tag{2.38}$$

where $f_{1(2)}$ is the parton distribution function which has the momentum fraction $x_{1(2)}$ and $G(\mathbf{b})$ is the overlapping funtion which expresses the transverse component.

2.4.2   Color Reconnection

In small collision system, e.g. proton+proton and proton-lead collisions, the collectivity which is a well-known phenomenon as "flow" in the heavy ion physics [19] is observed at LHC. This is not expected phenomenon in the small collision systems. In these days, "**Color Reconnection (CR)**" model which has been invented in 1980 [33] is attracted the attention again to resolve the collectivity in the small systems.

The sketch of the CR in the DPI is shown in Figure 2.14. (a): One parton pair scattering occurs and scattered partons are going out. These outgoing partons connect to other partons including the partons in the remnants in such a way that the total string length becomes as short as possible. (b): The independent parton pair scattering occurs and these partons connect to the other partons induced by the second scattering in the same way as first scattering. This is the MPI scenario. The CR is following process. (c): The partons scattered by the first and second subprocesses connect with each other in a way that the total string length becomes as short as possible. Without CR, the final stage hadrons induced by the first and second scattering don't correlate with each other. However, with the CR, the hadrons get correlations and consequently the correlation is observed as the collectivity. The strength of the correlation

is proportional to the number of parton scattering because the probability of parton connecting becomes large.

The CR has one more important expectation for hadron spectra at mid-rapidity. In the normal hard scattering, the scattered parton going toward mid-rapidity is pulled by the remnant partons of protons moving forward. In case of the CR scenario, the partons induced by MPI connect with each other as short as possible and consequently the partons at mid-rapidity is moving the same direction and boosted. Consequently, the hadrons at mid-rapidity can have larger transverse momentum than without the CR scenario. The boost effect is also expected to be large when a large number of parton scattering occurs.
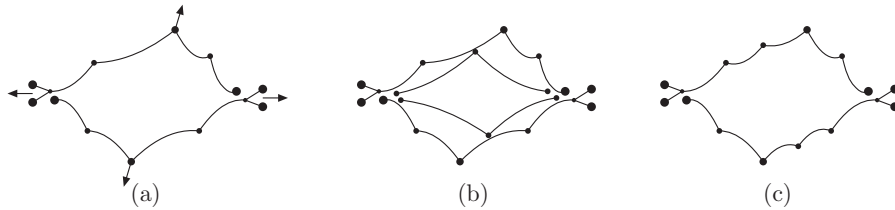
Figure 2.14: (a) In a hard gluon-gluon subcollision the outgoing gluons will be colourconnected to the projectile and target remnants. Initial state radiation may give extra gluon kinks, which are ordered in rapidity. (b) A second hard scattering would naively be expected to give two new strings connected to the remnants. (c)In the fits to data the gluons are colour reconnected, so that the total string length becomes as short as possible [33].

Chapter 3

Experimental Setup

3.1   Large Hadron Collider (LHC)

The Large Hadron Collider (LHC) located at CERN (European Organization for Nuclear Research) is a 26.7 km superconducting hadron accelerator situated from 45 m to 175 m below the surface of the ground [5]. The tunnel installed the LHC was constructed for the Large Electron-Positron (LEP) accelerator which had been operated from 1984 to 2000 [34]. It is constituted of eight straight and eight arc sections. Four straight sections have two beams crossing point, each.

In the proton-proton mode, it is designed to accelerate protons energy of $E_{beam} = 7$ TeV with instantaneous luminosities of $\mathscr{L} = 10^{34} \text{cm}^{-2}\text{s}^{-1}$. These parameters are 7 times higher energy and 60 times higher luminosity compared to the proton-antiproton collider, the Tevatron at Fermilab. In the heavy ion (Pb-Pb) mode, the designed luminosity is $\mathscr{L} = 10^{27} \text{cm}^{-2}\text{s}^{-1}$ and highest collision energy per nucleon is $\sqrt{s_{\text{NN}}} = 5.5$ TeV. This collision energy is 28 times higher than the Relativistic Heavy Ion Collider (RHIC) at BNL [14].

The LHC is composed of CERN's accelerator complex [6, 7, 8]. The LHC is the final stage of machines used to accelerate the beams. The protons and lead ions are initially obtained from hydrogen and lead ion atoms stripped electrons by the electric field. The continuous protons and lead ions are formed into bunches by radio-frequency quadrupoles (RFQ). The first accelerator chain is Linac 2 for protons and Linac 3 for lead ions and it accelerates them to an energy of 50 MeV and 4.2 MeV/u for proton beams and lead ion beams, respectively. After the Linac 3, the lead ions beams are boosted in the Low Energy Ion Ring (LEIR) to the energy of 72.2 MeV/u and then injected into Proton Synchrotron Booster (PSB). While the proton beams are injected into the PSB directory just after Linac 2. Both beams are accelerated to the energy of 1.4 GeV for proton beams and 94 MeV/u by the PSB. The Proton Synchrotron (PS) raises the energy of beams received from PSB to 25 GeV for the proton beams and 5.9 GeV/u for the lead ion beams. The PS shapes the final beam bunches structure. The bunch structure is splitted into 72 bunches for proton beams and 54 bunches for lead ion beams with a length of 4 ns (1.2 m) by the PS. The beams are sent to the Super Proton Synchrotron (SPS) and accelerated to the energy of 450 GeV and 177 GeV/u for proton beams and lead ion beams respectively. Finally, the LHC receives these beam bunches accelerated by SPS. The LHC takes about 20 minutes to achieve the final collision energies $\sqrt{s} = 14$TeV for proton-proton collisions and $\sqrt{s_{NN}}$=5.52 TeV for Pb-Pb collisions. The chain is summarized and shown in Figure 3.1. The LHC has 1232 superconducting dipole with a field of 8.33 T and 858 quadrapole magnets with 223 T/m [35]. The dipole magnets are 14.3 m each and covering the arc sections to bending the beam. The magnet is kept very low temperature (1.9 K) to produce extream magnetic field (8.33 T) by the superconducting magnet with a current of 11,850 A. The quadrupole magnets are located at straight sections to control the beam width.
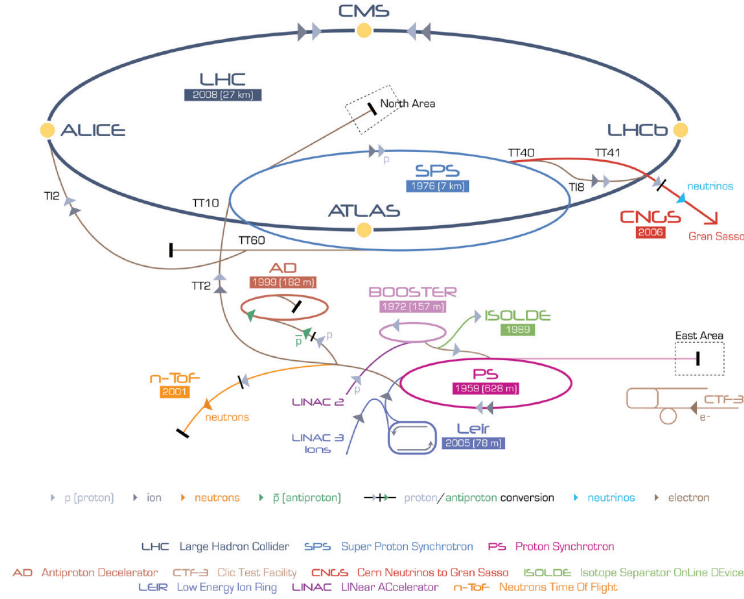
Figure 3.1: Shematic of the CERN accelerator complex [6, 7, 8].

The multipole magnets, sextupole, octupole and so on, are used to focus the beam. Normally, several multipole magnets are combined to focus the beams. The basic multipole magnetic set (FODO [5]) which is the combination of the several multipole magnets is shown in Figure 3.2. In addition to above multipole magnet sets, there are inner triplet magnets to focus on the collision points upstream of the four interaction points. By using FODO, the beam width is squeezed in 0.2 mm, while this inner triplet magnet squeezes the beam width to the size requested by each experiment (minimum size is 16μm).

The ALICE (A Large Ion Collider Experiment), the ATLAS (A Toroidal Lhc ApparatuS), the CMS (Compact Muon Solenoid) and the LHCb (Large Hadron Collider beauty) experiments are major experiments and installed at four interaction points in the LHC. In addition to these main experiments, there are three small experiments, LHCf (LHC forward), TOTEM (TOTal Elastic and diffractive cross section Measurement) and MoEDAL (Monopole and Exotics Detector At the LHC) experiments.

ALICE The ALICE experiment [1] is dedicated to the strong interaction QCD matter induced by heavy ion collisions. The detail of this experiments is explained in Section 3.2.

ATLAS and CMS The ATLAS experiment [36] and the CMS experiment [37] are general purpose detectors and designed primarily for proton-proton physics with the highest energy and instantaneous luminosity. Main physics goals of these experiments are searching for the Higgs boson, the precise test of the standard model and investigation of the beyond the standard model, e.g. the extra dimension and the supersymmetry. The ATLAS and the CMS experiments are located at LHC-IP1 and LHC-IP5, respectively.

LHCb The LHCb experiment [38] is located at LHC-IP8 and covers forward rapidity with focussing on the proton-proton physics. It is designed to specialize in the heavy flavor physics, especially CP-violation with the b-quark decay.
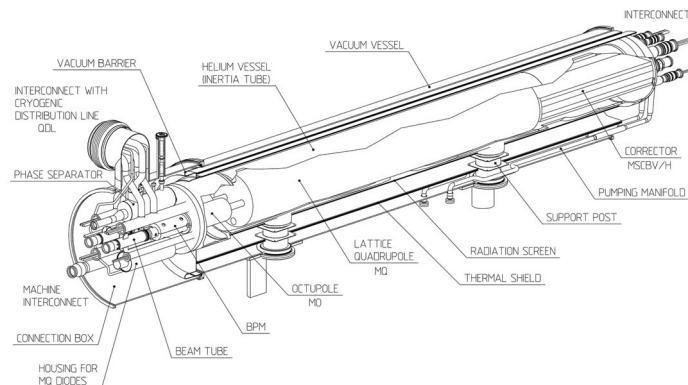
Figure 3.2: The multipole magnets sector (FODO) for squeezing the beam width to 0.2 mm [5].

LHCf The LHCf experiment [39] is designed to measure particles emitted in the very forward region ($|\eta| > 8.4$) in proton-proton collisions. This physics goal is to provide new information for the hadron interaction models used in the study of Extremely High-Energy Cosmic-Rays. The detector is installed at ±140m far away from ATLAS/IP1.

TOTEM The TOTEM [40] is dedicated to measuring the proton-proton elastic and inelastic cross sections including the diffractive interactions at LHC collision energies. Tracking detector is installed at either side of the CMS/IP5 collision point far away from ±9 m and ±13.5 m covering the pseudorapidity range of $3.1 < |\eta| < 6.5$.

MoEDAL The MoEDEL experiment [41] is designed to search for magnetic monopoles and highly charged exotic particles. The detector is deployed around the intersection region at LHCb/IP8.

3.2 ALICE experiment overview

ALICE (A Large Ion Collider Experiment) is one of a major experiment at the LHC which is focusing on the study of QCD matter induced by high energy heavy ion collisions. The ALICE detector is designed to deal with the condition created by central heavy ion collisions at LHC energies in which ~8000 charged particles are generated. The experiment consists of many subsystems to cover wide pseudorapidity and momentum ranges with very good particle identification capabilities. The systems can be classified into three categories central-barrel detectors, forward and trigger detectors and Muon spectrometer. The central-barrel detectors are embedded in the L3 solenoid magnet [1, 42]. The magnet is operated with the lower magnetic field (0.2∼0.5 T) than the other LHC experiments to measure very low transverse momentum particles precisely.

Tracking in the central-barrel region ($|\eta| < 0.9$) is executed by the Inner Tracking System (ITS), the Time-Projection Chamber (TPC) and the Transition Radiation Detector (TRD) with a very wide transverse momentum range ($0.1 < p_{\mathrm{T}} < 100\mathrm{GeV}/c$). In addition to these detectors, the Time-of-Flight (TOF) and the High Momentum Particle Identification Detector (HMPID) dedicate to the particle identification. These detectors cover different particles
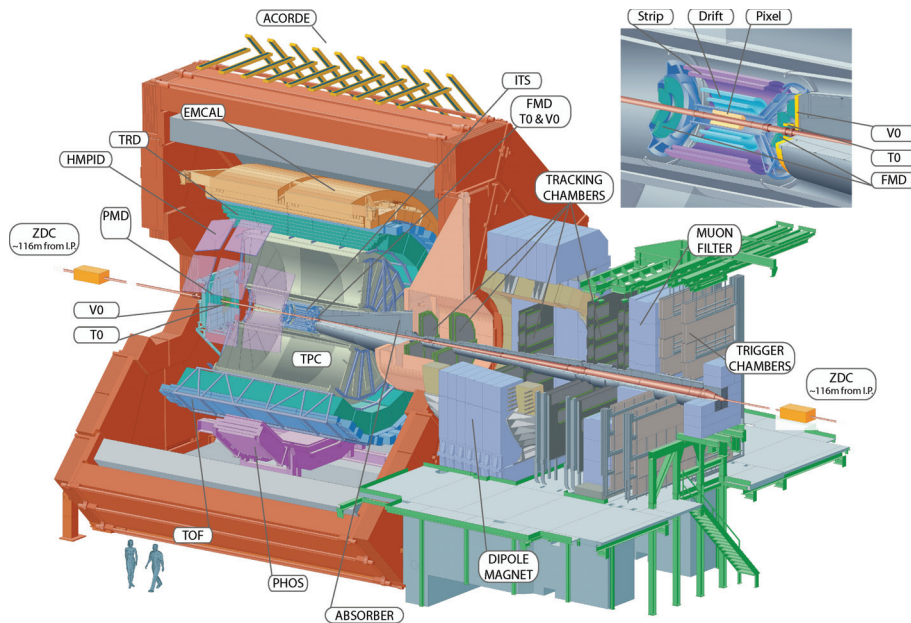
Figure 3.3: The ALICE detector overview [1].

and momentum ranges. In addition to these tracking detectors, two types of electromagnetic calorimeters, the ElecroMagnetic CALorimeter (EMCAL) and the PHOton Spectrometer (PHOS), are also installed at central-barrel and they can measure photons up to 80 GeV. Not only the photon measurement, electrons/positrons can be identified from E/p ratio, E is the energy measured by electromagnetic calorimeters and p is the momentum measured by the tracking system. The forward and trigger detectors are designed to decide global event characteristics. The VZERO (V0) detector is used minimum-bias trigger, reduction of background collisions and the event plane determination. The event time is measured by the TZERO (T0) detector with very good timing resolution (< 25 ps). The Zero Degree Calorimeter (ZDC) placed at far away from the collision point (~ 112 m) is used for an event trigger and the centrality determination in heavy ion collisions. Muon spectrometer is covering the forward rapidity ($-2.5 < \eta < -4.0$) to measure muons. There is muon tracking system which is constituted of a hadron absorber and tracking chamber called Muon CHamber (MCH) for reduction of hadron contamination and tracking. After the tracking chamber, there is the Muon TRigger Chamber (MTR) to identify muon and to trigger events which have single muon and/or dimuons. The overview of each sub-system is summarized in Table. 3.1.

3.3 Central barrel detectors

3.3.1 Inner Tracking System (ITS)

The innermost detector located closest to the interaction point is the Inner Tracking System (ITS) detector which is based on a silicon semiconductor [1, 43].

The main purposes of the detector are to measure the location of the interaction point with the resolution $< 100\mu$m, to the reconstruction of the secondary vertices created by long lifetime particles, e.g. hyperons and heavy flavor hadrons, to track and improve the momentum and angler resolution, and to identify the charged particles.

The detector is formed of six cylindrical layers with different detector technologies at radii

Detector	Acceptance		Position	Description
	Polar	Azimuthal		
SPD layer 1	$\|\eta\|$ <2.0	Full	$r = 3.9$ cm	Tracking, Vertex
SPD layer 2	$\|\eta\|$ <1.4	Full	$r = 7.6$ cm	Tracking, Vertex
SDD layer 1	$\|\eta\|$ <0.9	Full	$r = 15.0$ cm	Tracking, PID
SDD layer 2	$\|\eta\|$ <0.9	Full	$r = 23.9$ cm	Tracking, PID
SSD layer 1	$\|\eta\|$ <0.9	Full	$r = 38$ cm	Tracking, PID
SSD layer 2	$\|\eta\|$ <0.9	Full	$r = 43$ cm	Tracking, PID
TPC	$\|\eta\|$ <0.9	Full	$85 < r/\text{cm} < 247$	Tracking, PID
TRD	$\|\eta\|$ <0.8	Full	$290 < r/\text{cm} < 368$	Tracking, PID ($e^{\pm}$)
TOF	$\|\eta\|$ <0.9	Full	$370 < r/\text{cm} < 399$	PID
PHOS	$\|\eta\|$ <0.12	$220° < \phi < 320°$	$460 < r/\text{cm} < 478$	Photon
EMCal	$\|\eta\|$ <0.7	$80° < \phi < 187°$	$430 < r/\text{cm} < 455$	Photon and Jet
HMPID	$\|\eta\|$ <0.6	$1° < \phi < 59°$	$r = 490$ cm	PID
ACORDE	$\|\eta\|$ <1.3	$30° < \phi < 150°$	$r = 850$ cm	Cosmic
PMD	$2.3< \eta$ <3.9	Full	$z = 367$ cm	Photon
FMD1	$3.6< \eta$ <5.0	Full	$z = 320$ cm	Charged particle
FMD2	$1.7< \eta$ <3.7	Full	$z = 80$ cm	Charged particle
FMD3	$-3.4< \eta$ <-1.7	Full	$z = -70$ cm	Charged particle
VZERO1	$2.8< \eta$ <5.1	Full	$z = 329$ cm	Charged particle
VZERO2	$-3.7< \eta$ <-1.7	Full	$z = -88$ cm	Charged particle
TZERO1	$4.6< \eta$ <4.9	Full	$z = 370$ cm	Charged particle
TZERO2	$-3.3< \eta$ <-3.0	Full	$z = -70$ cm	Charged particle
ZDC (ZN)	$\|\eta\|$ >8.8	Full	$z = \pm113$ cm	Forward neutron
ZDC (ZP)	$6.5< \|\eta\|$ <7.5	$\|\phi\| < 10°$	$z = \pm113$ cm	Forward proton
ZDC (ZEM)	$4.8< \|\eta\|$ <5.7	$\|2\phi\| < 32°$	$z = \pm7.3$ cm	Forward Photon
MCH	$-4.0< \eta$ <-2.5	Full	$-14.2 < r/\text{m} < -5.4$	Muon tracking
MTR	$-4.0< \eta$ <-2.5	Full	$-17.1 < r/\text{m} < -16.1$	Muon trigger

Table 3.1: The overview of the ALICE detectors [1, 2].

between 3.9 to 43 cm from the beam line. The innermost two layers are the Silicon Pixel Detector (SPD) with a spatial resolution of 12 μm in z and 100μm in $r\phi$. The first and second layers cover full azimuthal and pseudo-rapidity of $|\eta|$ <2.0 and $|\eta|$ <1.4, respectively. The third and fourth layers are the Silicon Drift Detector (SDD), which has a resolution of 25×35 μm^2 in $r \times \phi$. It covers full azimuthal and $|\eta| < 0.9$. The outermost two layers are the Silicon Strip Detector (SSD) with a resolution of 830×20 μm^2 in $r \times \phi$.

The interaction point, primary vertex, is measured as the space point with the largest level of convergence of tracklets reconstructed by the SPD. The tracklets are defined as the lines joining pairs of hits in the first and second layers of the SPD. If the assumption that the number of tracklets depends on the number of primary charged tracks is considered, the tracklets are also used for the estimation of multiplicity event-by-event.

The SDD and SSD provide the PID information via specific energy loss (dE/dx) in the silicon material. The PID performance of the ITS as a function of track momentum is shown in Figure 3.4. From the figure, particles can be separated up to $\sim$0.2 GeV/c for electrons and pions, up to $\sim$1 GeV/c for kaons and pions, and up to $\sim$2 GeV/c for protons and pions.

3.3.2   Time Projection Chamber (TPC)

The Time-Projection Chamber (TPC) is the main tracking and particle identification detector of the ALICE experiment at central-barrel [1, 44]. The TPC covers the full azimuth and pseudo-rapidity of $|\eta|$ <0.9 for tracks with full radial track length and pseudo-rapidity $|\eta|$ <1.5 for tracks with 1/3 radial track length. Tracks with a wide transverse momentum range of from 0.1 GeV/c to 100 GeV/c with good momentum resolution, 6.5% for 10 GeV/c and 1% for
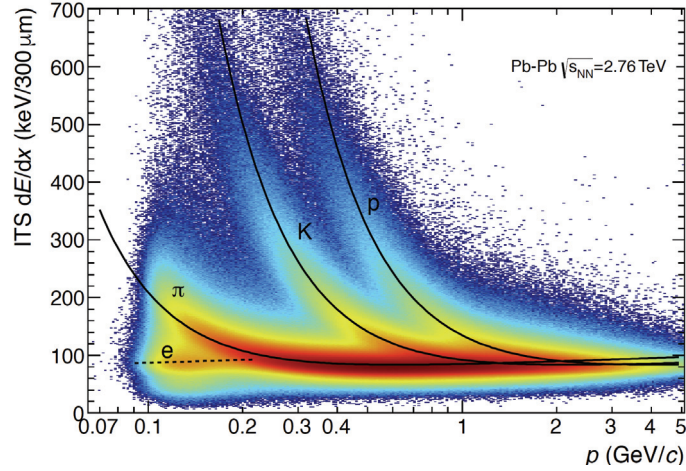
Figure 3.4: Distribution of energy loss in the ITS as a function of the track momentum with the expectation lines of each particle [2].

1 GeV/c, can be reconstructed by the TPC. The position resolution of each track is 1100-800 μm in $r\phi$ and 1250-1100 μm in z. The excellent transverse momentum and space resolution can be achieved by combining with ITS track information. A shape of the TPC is a hollow cylinder with the inner radius of about 85 cm, the outer radius of about 247 cm for an active volume filled with the mixture counting gas of Ne/CO_2 (90/10). The length of the beam axis is about 500 cm and divided into two drift regions by the central high voltage (HV) electrode. The drift voltage of -100 kV is applied to the central electrode and creates a 400 V/cm drift field toward the central electrode. A charged particles are traversing the active gas volume with ionizing the gas and generate electron and ion pairs form gas atoms. In the drift field, the electron and ion are separated and the electrons drift towards the end-plates with a drift speed of 2.65 cm/μm. While the ions drift towards the central plates with 1000 times slower drift speed. The arrival points on the end-pad plates are measured as a two-dimensional position (x and y) with the Multi-Wire Proportional Chambers (MWPC).

The read-out pad plates consist of 18 trapezoidal sectors, each covering 20° in azimuth. The radial track density is in proportion to $1/r^2$ where r is the distance from the center of the coordinate. The cluster occupancy on the read-out plate at innermost is very high. Therefore, one trapezoidal sector is divided into the Inner Read-Out Chambers (IROCs) and the Outer Read-Out Chambers (OROCs). Each IROC has 5504 read-out pads which are 4×7.5 mm^2 (63 padrows). OROCs have two different size pads, 6×10 mm^2 (64 padrows) and 6×15 mm^2 (outermost 32 padrows).

The charged particle energy loss dE/dx in the crossing active gas volume is proportional to the detected signal amplitude on the readout pads. The energy loss dE/dx as a function of track momentum with the Bethe-Bloch parametrization of each particle species is shown in Figure 3.5.

3.3.3 Transition Radiation Detector (TRD)

The main purpose of the Transition Radiation Detector (TRD) is to identify electrons/positrons above 1 GeV/c [1, 45]. Furthermore, the tracking information of the TRD improves the momentum resolution by combining the inner tracking detectors, especially at high transverse momentum region.

The TRD is located outside of the TPC at a distance of 290< r <368 cm and covers a full azimuth with a pseudo-rapidity of $|\eta| < 0.84$. The detector is segmented into 18 super modules,
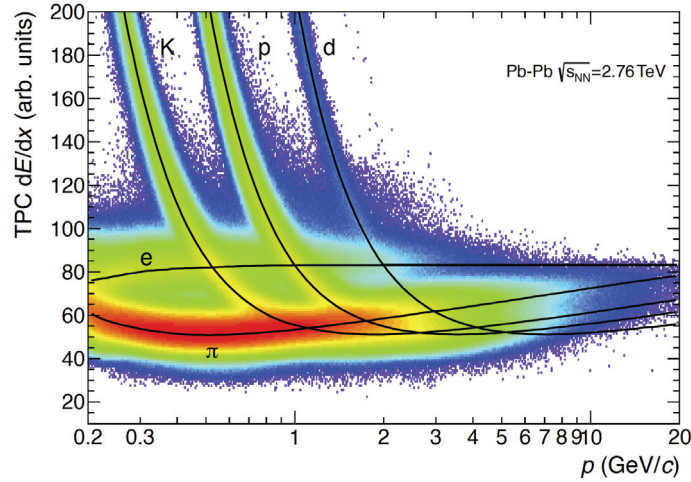
Figure 3.5: Distribution of energy loss dE/dx as a function of the tracking momentum. The lines represent that theory (Bethe-Bloch) expectation for several particle species [2].

each containing 30 chambers arranged in five stacks along the beam axis and six layers in the radial direction. Each chamber has a radiator of 48 mm thickness made of a carbon fiber laminated Rohacell/polypropylene fiber sandwich structure followed by 37 mm MWPC filled with Xe/CO_2 (85/15) mixture counting gas. The MWPC contains a 30 mm drift region and 7 mm amplification region with cathode pad read-out.

In addition to the ionization, transition radiation X-ray energy photons induced by the transition radiation are measured by the detector. The transition radiation photons are created at the beginning of the drift region where is the boundary between two media with different dielectric constants, but the normal ionization is created all drift region along the track direction. The intensity of the emitted transition radiation photons is proportional to the Lorentz factor $\gamma \sim p/m$. Therefore, electrons/positrons produce $m_\pi/m_e \sim 280$ times larger transition radiation photons than charged pions with the same momentum. The difference leads us to separate electrons/positrons from pions. The measured signal by the TRD as a function of $\beta\gamma$ is shown in Figure 3.6. Over $\beta\gamma \sim 4 \times 10^2$, the effect of transition radiation, TR, can be seen in the figure.

3.3.4 Time-Of-Flight (TOF)

The Time-Of-Flight (TOF) detector is designed to identify the charged particles with the intermediate momentum region, below about 2.5 GeV/c for pions and kaons, up to 4 GeV/c for protons [1, 46]. The TOF is placed outside of the TRD (370< r <399 cm) and covers the central pseudo-rapidity of $|\eta| < 0.9$ and full azimuthal angle. The detector measures the velocity β of the charged particles via the time required to travel from the collision point to the detector with a resolution of better than 40 ps. The start time of a collision is issued by the Cherenkov counter,T0 detector (introduced in Section 3.4.2).

The detector is segmented into 18 sectors in azimuth and to 5 segments in z direction. The Multi-gap Resistive Plate Chamber (MRPC) technology is used in the detector. The MRPC is a stack of resistive glass. When the charged particle traverses the chambers, it generates an avalanche electrons between the stacks. These electrons are measured to determine the passing timing.

The relationship between the track momentum and velocity allows estimating its mass. The mass is calculated with track velocity β which is inversely proportional to time measured
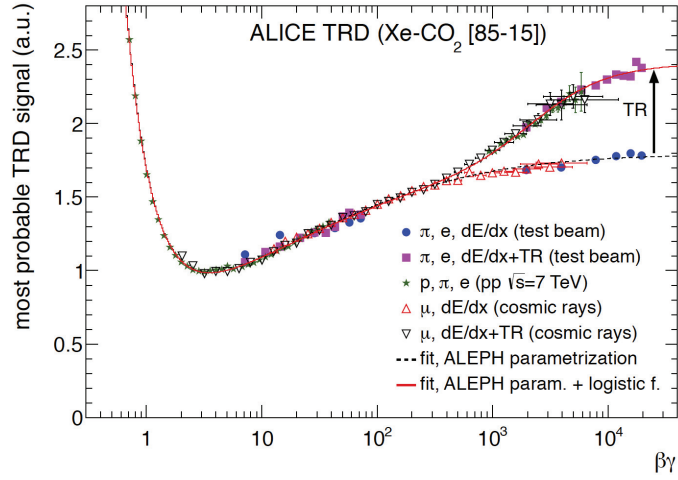
Figure 3.6: The most probable TRD signal as a function of $\beta\gamma$ [2].

by the TOF as

$$m_0 = \frac{p}{\gamma\beta c} \tag{3.1}$$

where p is track momentum, γ is the Lorentz factor and c is the speed of light. The particle velocity β as a function of the track momentum measured by the TPC is shown in Figure 3.7.
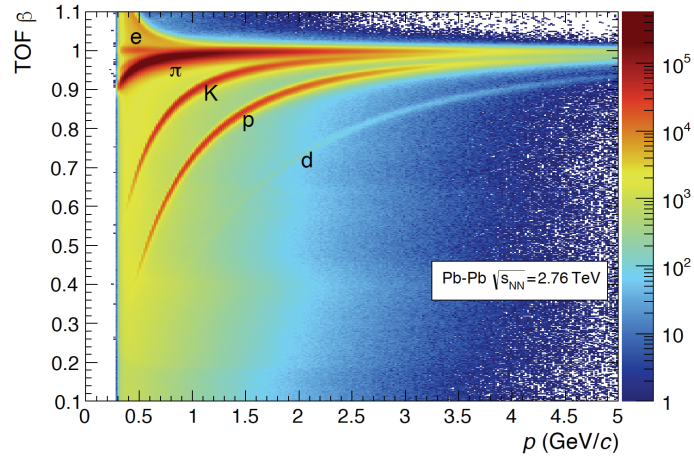
Figure 3.7: The track velocity β measured by TOF as a function of track momentum measured by TPC [2].

3.3.5 High-Momemtum Particle Identification Detector (HMPID)

The High Momentum Particle Identification Detector (HMPID) is dedicated to identify the charged particles especially at high transverse momentum region, over 1 GeV/c [1, 47]. The

detector is optimized to extend the discrimination of π/K and K/p, on track-by-track bias, up to 3 GeV/c and 5 GeV/c, respectively The HMPID covers a pseudo-rapidity of $|\eta| < 0.6$ and an azimuthal angle $1.2° < \phi < 58.8°$ and it is installed outside of the TOF (r=490 cm). The detector consists of 7 identical proximity-focusing Ring Imaging Cherenkov (RICH) modules of 1.5×1.5 m² each. The radiator is a 15 mm thick layer of C_6F_{14} liquid with n=1.2989 at λ= 175 nm. This value of the index of refraction is corresponding to $\beta_{min} = 0.77$. The momentum threshold is $1.21 \times m$, where m is the mass of the charged particle.

Cherenkov photons emitted by the fast charged particle traversing the radiator are detected by a photon counter with the novel technology of a thin layer of CsI deposited onto the pad cathode of a MWPC. The Cherenkov angle of the ring is given by

$$\cos\theta = \frac{1}{n\beta} \tag{3.2}$$

where n is the refractive index of the radiator introduced above and β is the track velocity. The relationship between the angle and track momentum is shown in Figure 3.8 with the expectations of respective particle species.
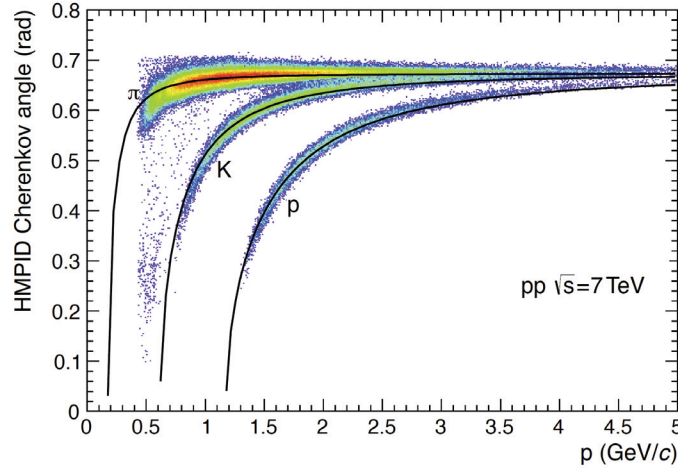
Figure 3.8: Mean Cherenkov angle measured by HMPID as a function of track momentum measured by the TPC. The lines represent the parametrization of Equation 3.2 for each species [2].

3.3.6   PHOton Sectrometer (PHOS)

The PHOton Spectrometer (PHOS) is a homogeneous electromagnetic calorimeter designed to measure direct photon and γ-jet [1, 48].

The PHOS is located at distance of 460 cm from the primary interaction point and is covering in a pseudo-rapidity of $|\eta| < 0.12$ and an azimuthal angle of $220° < \phi < 320°$. The detector is segmented into 5 modules. Each module is 3584 detection cells (56×64). The detection cell consists of a 22×22×180 mm³ lead-tungstate crystal PbWO$_4$ (PWO) attached to a 5×5 mm² Avalanche Photo-Diode (APD). The PWO crystal enhances the scintillation light yield under the low temperature. The increasing rate is 2% per °C. Therefore, the PHOS detector is operated at a temperature of -25±0.3°C.

The high-energy resolution and two-photon separation are obtained by using dense material

PWO crystal with a radiation length of $20X_0$. The energy resolution is measured as

$$\frac{\sigma_E}{E[\text{GeV}]} = \sqrt{\left(\frac{0.0130 \pm 0.0007}{E[\text{GeV}]}\right)^2 + \left(\frac{0.0130 \pm 0.0007}{\sqrt{E[\text{GeV}]}}\right)^2 + (1.12 \pm 0.3)^2}. \tag{3.3}$$

The high spacial resolution is obtained by selecting small Moliere radius scintillator. The spatial resolution is described as

$$\sigma_{x,y}[\text{mm}] = \sqrt{\left(\frac{3.26}{\sqrt{E[\text{GeV}]}}\right)^2 + 0.44^2}. \tag{3.4}$$

To cover a large dynamic range (0.005 - 80 GeV), two gains, high-gain (HG) and low-gain (LG) are implemented in the front-end electronics. The HG covers low energy region which is from 5 MeV to 5 GeV. While the LG covers the energy of 80 MeV to 80 GeV. When the ADC count is saturated with HG, the LG is switched on.

3.3.7 ElectroMagnetic CALorimeter (EMCal)

The primary goal of the ElectroMagnetic Calorimeter (EMCal) is the physics of jet quenching [1, 49]. Furthermore, the EMCal is used for electrons identification with the energy deposition in EMCal compared to its momentum measured by the TPC, especially at high transverse momentum from heavy flavor hadrons. It covers the large acceptance ($|\eta| < 0.7$ and $80° < \phi < 187°$) and located at 440 mm from the primary interaction point. The covering area is just opposite side of the PHOS detector. Therefore, γ-jet can be measured by combining the γ detected by the PHOS and jet detected by the EMCal.

The EMCal uses the technology of layered Pb-scintillator sampling calorimeter. The longitudinal pitch of Pb and scintillator are 1.44 mm and 1.76 mm, respectively. One sampling tower size is $6.0 \times 6.0 \times 28$ cm^2 with a radiation length of about 20.1 X_0 coupled to a 5×5 mm^2 Avalanche Photo-Diode (APD) which is same as PHOS APD. The 2×2 towers constitute one module. The super module covering $\Delta\eta = 0.7$ and $\Delta\phi = 20°$ consists of 12×24 modules.

The energy resolution is found to be

$$\frac{\sigma_E}{E[\text{GeV}]} = \frac{4.8\%}{E[\text{GeV}]} \oplus \frac{11.3\%}{\sqrt{(E\text{GeV})}} \oplus 1.7\%. \tag{3.5}$$

The EMCal is using two type of gain ranges, high gain and low gain. The high gain is covering from 16 MeV to 16 GeV. The dynamic range of the other one is from 250 MeV to 250 GeV.

3.3.8 ALICE Cosmic Ray Detector (ACORDE)

The ALICE COsmic Ray DEtector (ACORDE) is used to issue the fast trigger for the cosmic rays [1, 56]. It is placed on the upper surface of the L3 magnet and covering in the pseudo-rapidity of $|\eta| < 1.3$ and in the azimuthal angle of -60° $< \phi <$ 60°. The ACORDE consists of 60 modules which are made of two scintillator counters, each with 190×20 cm^2. The efficiency of the cosmic rays, especially muons, is over 90%. The cosmic rays triggered by the ACORDE are used for checking the detector alignment, calibration and performance of several ALICE tracking detectors, ITS, TPC, TRD and TOF.

3.4 Forward detectors

3.4.1 VZERO detector (V0)

The VZERO (V0) detector is designed as a small angle detector consisting of two arrays of scintillator counters installed on either side of the ALICE interaction point [1, 55]. The detector provides several trigger signals, minimum-bias (MB), multiplicity trigger and centrality

dependence trigger. In addition to the trigger, it is also used for the event multiplicity (centrality for heavy ion collisions) determination and remove the beam-induced background. The detectors cover 2.8< η <5.1 (V0A) and -3.7< η <-1.7 (V0C) with a full azimuth. Each side detector is segmented into 4 rings in the radial direction. The 4 rings are partitioned into 8 sectors in azimuth. The counter is using disk-shaped arrays of plastic scintillator connected to photomultiplier tubes via wavelength shifting fibers. The timing resolution is 1 ns. This timing resolution can distinguish the beam-beam interaction from the beam-gas interaction.

The scintillator light yield is proportional to the number of charged particles penetrating the detector. Therefore, the total charge induced by the scintillator light measured by the detector is used to estimate the multiplicity of the event. This multiplicity measurement is extended to estimate centrality in Pb-Pb collisions. Furthermore, the event plane is provided by measuring charged particle distribution in azimuth.

3.4.2   TZERO detector (T0)

The TZERO (T0) detector is the fastest trigger detector and it is designed to use the minimum bias trigger, and determination of a collision time which is used for the start time of TOF [1, 55]. The detector consists of two arrays of Cherenkov counter installed on either side of the ALICE interaction point. The T0 covers 4.6< η <4.9 (T0A) and -3.3< η <-3.0 (T0C) with a full azimuth.

The 12 counters compose an array. Each counter is a fine-mesh photomultiplier tube PMT coupled to a quartz radiator 20 mm in diameter and 20 mm thick.

The timing resolution is achieved about 50 ps. The correlation of the sum of the timing measured by T0A and T0C and difference between the timing of T0A and T0C is used to select the event which has the nominal vertex position.

3.4.3   Forward Multiplicity Detector (FMD)

The Forward Multiplicity Detector (FMD) is to provide charged particle multiplicity at forward rapidity [1, 55]. The FMD has three sectors and covers -3.4< η <-1.7 and 1.7< η <5.0 each. The detector is designed to measure the charged particle multiplicity with the silicon strip detector technology. The strip size is segmented finely to operate under very high particle multiplicity in Pb-Pb collisions.

The FMD is segmented into three rings. Two rings have outer and inner parts and one ring has an only inner ring. The inner ring is segmented into 20 sectors in a azimuth and into 512 strips in a radial direction. While the outer ring is segmented into 40 sectors in a azimuth and into 256 strips in a radial direction. The three inner rings are located at 320 cm, 83.4cm and -62.8 cm from the nominal interaction point along the beam axis. The two outer rings are placed at 75.2 cm and -75.2 cm from the nominal interaction point along the beam axis.

The charge particles deposit their energy as MIP in the silicon strip. The number of charged particles traversing the detector is estimated by total deposit energy in the detector. The coverage areas are partially overlapping with the SPD to allow to measure charged particle multiplicity with a large rapidity.

3.4.4   Photon Multiplicity Detector (PMD)

The Photon Multiplicity Detector (PMD) measures the multiplicity and spatial distribution of the photons at forward rapidity [1, 53]. The PMD is covering in a pseudo-rapidity of 2.3< η <3.7 and a full azimuth with a distance of 3.64 m from the ALICE interaction point.

The detector is segmented into 24 modules. Two different types of modules are installed and divided into 48×96 honeycomb cells. The calorimetric technique to measure photons at forward rapidity is not feasible due to the high density of the particles. Therefore, the PMD employs the pre-shower method with a thick converter consists of 1.5 cm thick lead with a

0.5 cm stainless steel backing ($3X_0$) sandwiched between two highly granular gas proportional counters filled with Ar/CO_2 (70/30). When charged particles penetrate the detector, there are signals in both proportional gas chambers before and after the converter. While, for the photons, there are tracks only after the converter. Therefore, with this difference, the number of photons is measured by the detector.

3.4.5 Zero Degree Calorimeter (ZDC)

The main goal of the Zero Degree Calorimeter (ZDC) detector is to estimate collision centrality in Pb-Pb collisions [1, 51]. The method to estimate the number of nucleons participating the collision is counted the number of spectator nucleons. The spectator nucleons move towards beam axis ($\sim 0°$) as protons and neutrons. By measuring the total energy of the participant protons and neutrons at forward rapidity, the centrality and collision geometry can be estimated.

The ZDC consists of the electromagnetic calorimeter (ZEM) covering $4.8 < \eta < 5.7$ and two hadron calorimeters for protons (ZP) and neutrons (ZN) covering $6.5 < |\eta| < 7.5$ and $|\eta| > 8.8$, respectively. The ZP and ZN are the quartz fibers sampling calorimeters. The shower generated in a dense absorber (passive material) produces the Cherenkov radiation in quartz fiber (active material) of ZP and ZN. There is a space limitation for ZN. The very dense material, W-alloy is employed as the passive material for ZN ($7.04 \times 7.04 \times 100$ cm^3). On the other hand, there is no space limitation for ZP and the spectator protons have a wide spatial distribution. Therefore, the ZP covers the large area ($12 \times 22.4 \times 150$ cm^3) and made of brass. The ZEM is designed to measure photons emitted from neutral pion and uses lead plate as a passive material ($7.0 \times 7.0 \times 20.4$ cm^3). The energy resolution of ZN and ZP are described as

$$(\sigma/E)^2 = \left(\frac{2.57 \pm 0.03}{\sqrt{E[\text{GeV}]}} \right)^2 \oplus (0.163 \pm 0.006)^2, \tag{3.6}$$

$$(\sigma/E)^2 = \left(\frac{2.37 \pm 0.02}{\sqrt{E[\text{GeV}]}} \right)^2 \oplus (0.125 \pm 0.002)^2, \tag{3.7}$$

and ZEM energy resolution is as

$$\frac{\sigma}{E} = \frac{0.69}{\sqrt{E[\text{GeV}]}}. \tag{3.8}$$

The spectator neutrons are not deflected by the LHC bending magnets and are detected by ZN located between two beam pipes. On the other hand, spectator protons are deflected by the magnet and go out of the beam pipe, they are detected by the ZP located side of the beam pipe. The ZEM is monitoring the number of the particle generated by the primary hadronic interaction and is used to distinguish the hadronic interaction and the ultra-peripheral interactions.

3.5 Muon spectrometer

The Muon spectrometer consists of the front absorber followed by a dipole magnet of 3 T/m with the Muon Chamber (MCH) and the Muon Trigger (MTR) [1, 50, 52]. The system is located at a forward rapidity of $-4.0 < \eta < -2.5$ to measure and identify the muons with wide transverse momentum range. The front absorber made of predominantly out of carbon and concrete with $\sim 10\lambda_{int}$ corresponding to $\sim 60X_0$ is placed in front of the MCH to reduce the hadron contamination. The MCH has five stations of the tracking chambers: first and second stations are placed before the dipole magnet, the third chamber is set in the dipole magnet and fourth and fifth are installed after the magnet. Some tracks measured by the MCH are

the origin of the particle generated in the front absorber and including particles which are not muons. To remove these not muon tracks, there is a wall made of an iron with $\sim 7.2\lambda_{int}$ placed at after the MCH. If the particle penetrating the wall, the tracks are regarded as muons. To check if the tracks measured by the MCH penetrate the wall or not, the MTR is placed at behind of the wall.

Each station has two chambers. The technology used in the MCH is the cathode pad chamber filled with Ar/CO_2 (80/20). The various size pads are used in the MCH. The smallest pad (4.2×6.3 mm^2) is installed in the innermost part of the first station because the occupancy is the highest. The slat structure cathode chamber is installed in the third, fourth and fifth station. The largest cathode pad with 5×100 mm^2 is used in the last station. The MTR is used the Resistive Plate Chambers (RPCs) with streamer mode. The MTR consists of two stations which have two chambers each. The 18 RPC modules constitute one chamber. The typical RPC module size is 70×300 cm^2. The space resolution of ~ 1 cm is achieved by the RPC filled with $Ar/C_2H_2F_4/$i-buthane$/SF_6$ (50.5/41.3/7.2/1) and with one gas gap of 2 mm. The transverse momentum threshold is calculated by using the length the track point measured by the third station of the MCH from the straight line between the point measured by the MTR and the nominal collision position.

The MTR can distinguish the event which has only one muon from more than two muon tracks. Furthermore, it can identify $+-$, $++$ and $--$ muon combinations. The Muon Spectrometer is operated separately and can take data at higher rate and luminosity compared to the central-barrel detectors.

3.6   Trigger, Readout

3.6.1   Trigger System: Central Trigger Processor (CTP)

The trigger decision is provided by the Central Trigger Processor (CTP) of ALICE based on the trigger detectors and the LHC filling scheme [1, 54]. The trigger detectors are listed in Table. 3.2. The CTP collects the trigger signals from trigger detectors every LHC-machine clock of 25 ns. The Level-0 (L0) trigger decision is made within $\sim$0.9 μs after the collision with SPD, V0, T0, TOF, PHOS, EMCal and MTR trigger inputs. The event accepted by the L0-trigger criteria further evaluated by the Level-1 (L1) trigger algorithm in the CTP. The L1-trigger latency is $\sim$6.5 μs after L0-trigger due to computation time for TRD and EMCal and propagation time for ZDC. The L0- and L1-trigger decision is delivered to the detectors within $\sim$300 ns latency after each level trigger evaluated by the CTP. The final stage of the trigger is the Level-2 trigger which decides if the data is recorded or not. The L2-trigger is made within $\sim$90 μs corresponding to drift time of the TPC after the collision. The event data triggered by the L2-trigger is sent to the Data Acquisition system (DAQ) to record the event data, in parallelly, to the High-Level Trigger system (HLT). The CTP makes a decision which detectors will readout and provides the information to the DAQ explained in Section 3.6.2.

The most important trigger configurations are listed in Table.3.3. The minimum-bias trigger (MB$_{or}$ and MB$_{and}$) are used in proton-proton collisions. The MB$_{or}$ is high efficiency, but it also collects the background interactions, e.g. beam-gas interactions. Therefore, under high luminosity and background level conditions, high purity minimum-bias trigger MB$_{and}$ is used. The central trigger is based on the number of total hits on the V0 detector. The electromagnetic calorimeters (PHOS and EMCal) provide L0-trigger by requiring energy detection above the threshold. In addition to L0-trigger, several L1-triggers for photons (EGA) and jets (EJE) are provided by the EMCal. The TRD produces the L1-trigger for electrons and jets. The jet trigger provided by the TRD (TJE) requires least three tracks above 3 GeV/c in the TRD. The Muon Spectrometer provides the four types L0-triggers with two different thresholds. The MSL, MUL and MLL are the lower threshold triggers (0$\sim$1.0 GeV/c). The MSL is the single muon trigger. The other MUL and MLL are dimuon trigger, the former one is unlike-sign two

Detector	Function	Level
SPD	hadronic interaction trigger, hit-multiplicity trigger	L0
V0	non-single diffractive interaction minimum bias trigger	L0
T0	event vertex selection minimum bias trigger	L0
TRD	electron trigger, high-p_T particle trigger, charged-jet trigger	L1
TOF	topological trigger, cosmic-ray trigger	L0
PHOS	photon trigger	L0
EMCal	photon trigger, neutral-jet trigger	L0/L1
ACORDE	cosmic-ray trigger	L0
ZDC	minimum-bias trigger and EM dissociation trigger in Pb-Pb	L1
MTR	single-muon trigger, dimuon-trigger	L0

Table 3.2: Trigger detectors

muons $(+-)$ and the latter one is like-sign two muons $(++, --)$. The MSH is using the higher threshold $(1.0\sim4.2\ \mathrm{GeV}/c)$ trigger for single muon. Several additional triggers are implemented to enhance the events related to diffractive in pp, ultraperipheral in Pb-Pb collisions and the cosmic-ray physics. The diffractive event has a large rapidity gap. The DG trigger requires at least one hit in the SPD but no hit in the V0 detector. The trigger for central ultra-peripheral (CUP) requires the large rapidity gap same as the DG trigger criteria. On the other hand, the forward ultra-peripheral event has a few particles in the forward rapidity and no particle in the central rapidity. The MUP is the trigger for the events and requires the muon tracks in forward rapidity and no hit in the SPD. The cosmic ray event triggered by the ACORDE detector (COS) and used to calibrate and align the detectors.

Trigger	Descreption	Criteria
MB-type triggers		
MB$_{or}$	minimum bias	signals in V0 and SPD
MB$_{and}$	minimum bias	signals in V0A and V0C
MBZ	minimum bias	MB and signals in both ZDC's
SPI	multiplicity trigger	n hits in SPD
Centrality triggers		
CENT	central	V0 based centrality trigger for Pb-Pb (0-10%)
SEMI	semicentral	V0 based semicentrality trigger for Pb-Pb (0-50%)
EMCal triggers		
E0	EMCal L0	EMCal L0 trigger with MB
EJE	neutral jet primary	EMCal L1 jet trigger following E0
EJE2	neutral jet secondary	EJE with lower threshold
EGA	photon primary	EMCal L1 photon trigger following E0
EGA2	photon secondary	EGA with lower threshold
TRD trigger		
TJE	charged jet	n charged particles in TRD with MB
TQU	electron for quarkonia	electron with $p_T > 2$ GeV/c with MB
TSE	electron for open beauty	electron with $p_T > 3$ GeV/c with MB
Muon trigger		
MSL	single muon low	single muon in MTR with MB
MSH	single muon high	MSL with high threshold
MUL	dimuon unlike sign	two muons with low threshold, unlike sign with MB
MLL	dimuon like sign	two muons with low threshold, like sign with MB
miscellaneous trigger		
HM	high multiplicity	high multiplicity in SPD with MB
PH	photon by PHOS	PHOS L0 trigger with MB
EE	single electron	electron signal in TRD sector 6-8 and EMCal
DG	diffractive	charged particle in SPD and no signal in V0, p-p
CUP	barrel ultraperipheral	charged particle in SPD and no signal in V0
MUP	muon ultraperipheral	muons in MTR and no signal in V0
ZED	electromagnetic dissociation	signal in ZN
COS	cosmic trigger	signal in ACORDE

Table 3.3: Trigger configurations

3.6.2 Readout: Data Acquisition (DAQ)

The ALICE Data Acquisition system (DAQ) takes the signal from the CTP containing which detectors data will be recorded [1, 54]. Each detector send their data via the Detector Data Links (DDLs) to buffering space in the DAQ Local Data Concentrators (LDCs). In case that the data size exceeds the buffer size, the DAQ sends the back-pressure (busy) signal to the CTP. In one triggered event, the information comes from different detectors. The DAQ collects these all information and combines them in the Global Data Collectors (GDCs) to form a full event.

The busy time of the data taking is mainly fixed by the CTP waiting time for the completion of the readout of all detectors. The typical busy time of each detector in each collision system is shown in Tab.3.4. The busy time depends on the collision system due to the event data size. By the ability of event buffering, SPD, TOF, T0 and V0 have not busy time.

Detector	pp		Pb-Pb		p-Pb	
	Busy time (μs)	Data size (kB)	Busy time (μs)	Data size (kB)	Busy time (μs)	Data size (kB)
SPD	0	7	0	26	0	7
SDD	1024	22	1024	143	1024	16
SSD	265	46	265	180	265	42
TPC	500	6676	500	25740	350	15360
TRD	300	181	450	3753	270	350
TOF	0	23	0	63	0	23
PHOS	850	25	850	72	850	35
EMCal	270	22	300	53	270	25
HMPID	220	15	300	22	220	18
ACORDE	116	0.1	116	0.1	116	0.1
PMD	170	10	220	50	170	8
FMD	190	14	350	55	190	13
V0	0	6	0	6	0	6
T0	0	0.4	0	0.7	0	0.6
ZDC	122	-	122	0.8	122	0.7
MCH	300	35	300	61	250	18
MTR	160	7	160	7	160	7

Table 3.4: Busy time of each detectors shown in [2, 54]

Chapter 4

Data Analysis

In this chapter, the data analyses for the measurement of π^0 production cross section in proton+proton collisions at $\sqrt{s} = 8$ TeV with PHOS detector are explained. The analysis procedure is divided broadly into five steps. The Section 4.1.1 is the selection of good events which is adequate for the π^0 measurement. The next step is the reference cross section measurement. This reference cross section is the basis of not only π^0 measurement but also all other measurements. The third step is the event characterization of event activity according to multiplicity. The fourth step is photon measurement and identification by using the PHOS which is an electromagnetic calorimeter. The Section 4.4 is the π^0 reconstruction from two photons detected by the PHOS with the invariant mass method.

4.1   Data Condition

4.1.1   Beam Condition

This analysis is based on the experimental data taken in 2012, proton+proton collisions at $\sqrt{s} = 8$ TeV. The ALICE detector is located at the interaction point IP2 of LHC. In 2012 runs, the bunch intensity achieves 2×10^{14} protons/beam. This intensity is too high for ALICE detectors to operate safely. The collision rate including beam-beam and beam-gas collisions should be around 700 kHz for the ALICE detectors. From this point, the target luminosity is set $\mathscr{L} \sim 10^{29} \mathrm{s}^{-1} \mathrm{cm}^{-2}$ corresponding to collision probability of around 4% per one bunch crossing. For the satisfaction of the luminosity, a "main-satellite" bunch collision scheme is adopted for proton+proton runs at IP2. This is the encounter of the main bunches of one beam with the satellite bunches of the other beam. The satellite bunches sit between two main bunches, 25 ns away from the main bunches. The intensity of the satellite bunches is about 0.1% of that of main bunches, 1.6×10^{11} protons/beam. The collision rate is reduced by the same factor.

The filling scheme in 2012 is **50ns_1374_1368_0_1262**. This means that the closest space between main bunches is 50 ns, the number of main-main bunch crossing at IP1 (ATLAS), IP4 (CMS), IP2 (ALICE) and IP8 (LHCb) are 1374, 1368, 0 and 1262, respectively. The number of main-main bunch collisions never occur at IP2 because the LHC provided the main-satellite bunch collisions at IP2 as explained above. Hence, the number of main-main bunch collisions at IP2 is 0.

4.1.2   Global Event Selection

The primary vertex is measured by using two layers silicon pixel detector (SPD) installed innermost place, the distance of 3.9 cm and 7.6 cm away from the nominal interaction point.

The primary vertex resolution measured by only SPD is about 300μm in proton+proton collisions. When the primary vertex exists at the edge of the SPD, the primary vertex cannot be measured correctly. Therefore, the cut related to the primary vertex position along to the beam axis (Z_{vtx}) is applied to select more reliable measured vertex events. In this analysis, the events of which the primary vertex position is within 10 cm from the nominal point are used. Of course, these should be more than one particle detected by the SPD to determine the vertex.

The collision probability per one bunch crossing, μ, is about 0.04. In this condition, inter-bunch pileup event is taken into account. The inner-bunch pileup is the event that more than one proton pair collides in the one bunch crossing, which is called as "pile-up". The pile-up event can be identified by the SPD and these events are rejected from the analysis at all.

The machine induced backgrounds, e.g. beam-gas interaction, contaminate the measurements. These events can be identified and removed by using the V0 detector placed on both sides of the nominal collision points. The detail of the procedure to reject the event will be explained in Section 4.1.7.

4.1.3 Event Trigger Selection

The ALICE experiment equips many event selection triggers to collect interesting events which are shown in Table 3.3. It is easy to select events which have specific character particles, e.g high transverse momentum and heavy particles which raise jets and specific event topology. On the other hand, it is difficult to trigger light particles and/or low transverse momentum particles effectively. One method to measure low transverse momentum and/or light particles is the minimum-bias event trigger. This trigger collects the event which generates at least two particles toward forward and backward directions. This requirement may add the bias to select the event, but it is expected to be very small. Therefore, it is called "minimum"-bias.

To cover a wide momentum range of neutral pion, two type triggers, minimum-bias trigger and high energy photon trigger, are used. As explained above, the minimum-bias trigger is suitable for measurement of low transverse momentum region. The other event selection trigger is specified to select the events which have at least one high energy photon is used to measure high transverse momentum region. These two triggers used in this analysis are explained below.

Minimum-Bias Trigger (MB$_{\text{AND}}$)

In 2012 proton+proton running program, the ALICE Minimum-Bias trigger, MB$_{\text{AND}}$, requiring hits in the both V0-A and V0-C arrays [2] is operated. The MB$_{\text{AND}}$ is sensitive to 77% of the total inelastic cross section in proton+proton collisions. The trigger is used as a reference trigger for all other specific trigger equipped with ALICE. Therefore, the trigger cross section measurement is important for the other measurement (see Section 4.1.4).

4.1.4 Luminosity Determination

The luminosity of a particle collider, $\mathscr{L}$, is simply expressed as

$$\mathscr{L} = \frac{R}{\sigma} \tag{4.1}$$

where R is the collision rate and σ represents the cross section for the collision process. For colliders with a bunched beam, such as the LHC, the luminosity of the accelerator is a sum of the luminosity of each colliding bunch pair $\mathscr{L}_{\text{BC}}$. Each colliding bunch pair luminosity can be calculated as

$$\mathscr{L}_{\text{BC}} = f_{\text{rev}}^{\text{LHC}} n_1 n_2 \int \rho_1(x,y)\rho_2(x,y)\mathrm{d}x\mathrm{d}y \tag{4.2}$$

here $f_{\mathrm{rev}}^{\mathrm{LHC}}$ is the bunch revolution frequency, n_i is the number of particles in bunch i, and $\rho_i(x, y)$ is the normalized particle density profile of bunch i. The luminosity in Equation 4.2 can be calculated by the observed, or visible, proton+proton interaction rate per bunch crossing, μ_{vis} with the unknown cross section, σ_{vis}, as

$$\mathscr{L}_{\mathrm{BC}} = f_{\mathrm{rev}}^{\mathrm{LHC}} \frac{\mu_{\mathrm{vis}}}{\sigma_{\mathrm{vis}}}. \tag{4.3}$$

The unknown visible cross section σ_{vis} can be measured by combining Equation 4.2 and Equation 4.3. The overlap integral in the Equation 4.2 can be estimated by using a method developed by Simon van der Meer [58] without any prior knowledge of the bunch density profile, $\rho_i(x, y)$.

In the ALICE experiment, the minimum-bias triggered event is defined as the reference event. Therefore, for following sections, the visible collision means the event triggered by the minimum-bias trigger.

4.1.5   Beam Separation Scan Technique

Under the assumption that the bunch density profiles can be factorized into independent horizontal and vertical components, the Equation 4.2 can translate as

$$\mathscr{L}_{\mathrm{BC}} = f_{\mathrm{rev}}^{\mathrm{LHC}} n_1 n_2 \int \rho_{x1}(x)\rho_{x2}(x)\mathrm{d}x \int \rho_{y1}(y)\rho_{y2}(y)\mathrm{d}y. \tag{4.4}$$

To estimate the profile term, $\int \rho_{x1}(x)\rho_{x2}(x)\mathrm{d}x$, the two beams are separated in the horizontal (x) direction, and then the relationship between the separation length and the minimum-bias trigger rate is measured. This beam separation procedure is known as a van der Meer (vdM) scan [58]. The minimum-bias trigger rate, μ_{MB}, as a function of the separation length, h, is expressed as

$$\mu_{\mathrm{MB}}(h) = A \int \rho_{x1}(x)\rho_{x2}(x+h)\mathrm{d}x \tag{4.5}$$

where A is an unknown proportionality constant. By integrating Equation 4.5 with respect to separation is expressed as

$$\int \mu_{\mathrm{MB}}(h)\mathrm{d}h \;=\; A \int \left\{ \int \rho_{x1}(x)\rho_{x2}(x+h)\mathrm{d}x \right\}\mathrm{d}h \tag{4.6}$$

$$=\; A \int \left\{ \int \rho_{x1}(x)\rho_{x2}(a)\mathrm{d}x \right\}\mathrm{d}a \tag{4.7}$$

$$=\; A \int \rho_{x1}(x)\mathrm{d}x \int \rho_{x2}(a)\mathrm{d}a = A \tag{4.8}$$

under the assumption the μ_{MB} is very small at the large beam separation, which is expressed as the substitution $x + h \to a$ and $\mathrm{d}h \to \mathrm{d}a$. The normalize beam profile part can be obtained with ratio of the Equation 4.8 and the minimum-bias trigger rate with no separation as

$$\frac{\int \mu_{\mathrm{MB}}(h)dh}{\mu_{\mathrm{MB}}(0)} \;=\; \frac{A}{A \int \rho_{x1}(x)\rho_{x2}(x)\mathrm{d}x} \tag{4.9}$$

$$=\; \frac{1}{\int \rho_{x1}(x)\rho_{x2}(x)\mathrm{d}x} = \sqrt{2\pi}\Sigma_x \tag{4.10}$$

By performing a same procedure for the beam separation in the vertical direction, the Σ_y is also obtained. The luminosity formula (Equation 4.4 can be expressed with the Σ_x and Σ_y which is written by the interaction rates (Equation 4.10) instead of the beam profile as

$$\mathscr{L}_{\mathrm{BC}} = \frac{f_{\mathrm{rev}}^{\mathrm{LHC}} n_1 n_2}{2\pi \Sigma_x \Sigma_y}. \tag{4.11}$$

The minimum-bias trigger cross section can be obtained with above formula and it is rewritten as

$$\sigma_{\text{MB}_{\text{AND}}} \quad = \quad \mu_{\text{MB}}(0)\frac{2\pi\Sigma_x\Sigma_y}{n_1 n_2} \tag{4.12}$$

$$= \quad \frac{1}{n_1 n_2 \mu_{\text{MB}}(0)} \int \mu_{\text{MB}}(h_x)\mathrm{d}h_x \int \mu_{\text{MB}}(h_y)\mathrm{d}h_y \tag{4.13}$$

where h_x and h_x is the separation length for vertical and horizontal direction.

Each parameter, the bunch population product $n_1 n_2$ and the minimum-bias trigger rate without separation $\mu_{\text{MB}}(0)$ can be different from each pair of colliding bunches. However, the differences are canceled out and the same value of $\sigma_{\text{MB}_{\text{AND}}}$ is measured for each colliding bunch pair. The property enables a consistency check on the vdM scan procedure.

4.1.6 Scan Procedure

A special run was requested to implement vdM-scan in July 2012. The beam filling scheme during the scan is **Multi_50b_3_31_16_4bpi13inj** (fill 2852). This means there are 13 beam trains and 4 bunches exist in each train and bunches are crossing 3, 31, and 16 times per one circle at the IP1/IP5 (ATLAS/CMS), IP2 (ALICE) and IP8 (LHCb), respectively. The additional several parameters at IP2 are, the β^* value was 10 m, and the vertical beam crossing angle is -212 μred, in which the minus sign indicates that the beam crossing position exists in the negative y coordinate with the respect beam axis. The maximum beam separation during the scan was about 0.6 mm corresponding to about six times the RMS of the nominal transverse beam profile.

The process of the one scan is divided into two parts, the horizontal scan (SX) and vertical scan (SY). In the horizontal scan, the beams are moved in the horizontal direction and they are kept at center in the vertical axis. By the procedure, the parameter Σ_x related to the beam profile can be extracted (as expressed in Equation 4.5). Then, the moving direction is changed from horizontal direction to vertical direction and the parameter Σ_y is obtained. One scan set is these horizontal and vertical scans and two sets are implemented. The beams are moved in 25 steps, each step length is 25 μm, in one direction scan and it takes 30 seconds to take data for each step. To check each step separation length, a length-scale calibration scan is also performed, which will be shown in Section 4.1.8. The analysis details are introduced in following sections.

4.1.7 Minimum-Bias Trigger Rate

The raw rate of the minimum-bias trigger R_{Raw} during a time interval i is defined as

$$R_i^{\text{Raw}} \quad = \quad f_{\text{rev}}^{\text{LHC}}\frac{C_i}{O_i} \tag{4.14}$$

where C_i is the number of triggers counted and O_i is the number of orbits during the given time interval. The measured rate as a function of time is shown in Figure 4.1. The filled regions are vdM scan periods. First two filled periods are the first scan for horizontal and vertical direction, and second two are the second scan. The raw rate indicated by Equation 4.14 and shown in Figure 4.1 is affected by (1) beam intensity decay, (2) machine induced background and (3) pile-up. These contributions have to be removed and are explained by following.

Machine Induced Background

In the beam pipe, the air pressure is kept very low ($\sim 10^{-6}$ mbar). However, there is machine-induced background gas induced by interacting of the beam with the accelerator matter. The background rate depends on the residual gas pressure and on the collimator cleaning efficiency.
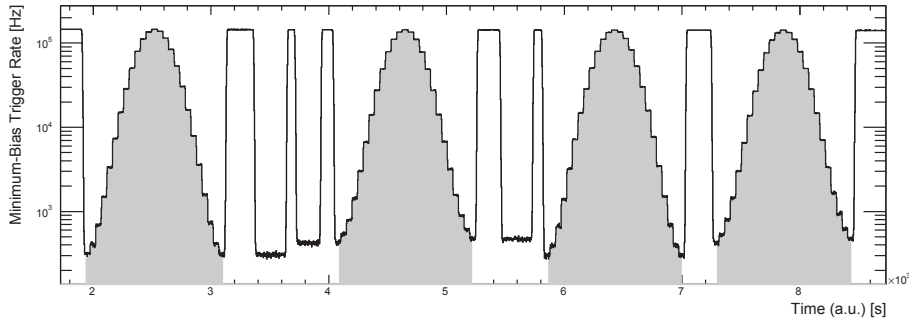
Figure 4.1: The minimum-bias trigger raw rate. The rate is affected by three contamination, beam intensity decay, machine induced background and pile-up.

The interactions between the beam and the gas may be a possible and the effect works to enhance the trigger rate. Unfortunately, the ALICE detectors are located close to the injection point of the Beam1 Transfer Line TI2 [8]. Therefore, the main component of the beam background for ALICE is produced by inelastic beam-gas interactions during the beam injection.

In addition to the machine induced background, one more effect induced by the satellite-charges should be taken into account. The crossing angle of the two beams at IP2 is in the vertical plane. As the beam separation increases in the vertical direction, the two main bunches move in opposite directions. Consequently, the satellite-charges which are captured in the next to the center of the RF bucket start to collide with particles in the central bucket. This effect also works to enhance the trigger rate, in particular, when the separation length becomes larger.

Above two background interaction sources can be identified and rejected by using the sum and difference of arrival times in the two V0 arrays. The nominal interaction time t_0 is given by LHC (LHC-clock). The nominal signal arrival time of beam-beam interaction is 11.3 ns and 3.0 ns after t_0 for V0A and V0C respectively. Therefore, sum and difference of the arrival time is around $(t_{V0A}-t_{V0C}, t_{V0A}+t_{V0C})$ = (8.3 ns,14.3 ns). While, when the beam-gas interactions occur at behind the V0A ($z > 340$ cm), the arrive time of V0A about 11.3 ns before t_0 and arrive at V0C about 3.0 ns after t_0. On the other hand, the particles coming from the beam-gas interaction behind the V0C ($z < 90$ cm) arrive at V0C about 3.0 ns before t_0 and arrive at V0A about 11.3 ns after t_0. The sum and difference arrival time of these interactions are around $(t_{V0A}-t_{V0C}, t_{V0A}+t_{V0C})$ = (-14.3 ns, -8.3 ns) for the behind V0A and $(t_{V0A}-t_{V0C}, t_{V0A}+t_{V0C})$ = (14.3 ns, 8.3 ns) for the behind V0C. The satellite-charge contribution can be identified by the same method because the satellite-charges exist in the next RF bucket and the collisions happen 2.50 ns later or earlier in time compared to t_0. Therefore, these contributions can be identified and removed with the particle arrival time of the V0A and V0C. A correlation between difference of the arrival time of the V0A and V0C ($t_{V0A}-t_{V0C}$) and sum of the arrival time of the V0A and V0C ($t_{V0A}+t_{V0C}$) are shown in Figure 4.2.

The background from beam-gas and beam-satellite interactions are estimated by using the sum and difference arrival time of V0A and V0C detector. The interactions which fulfill the sum of arrival time between 10 ns$< t_{V0A} + t_{V0C} <$18 ns and the difference of arrival time between 4 ns$< t_{V0A} - t_{V0C} <$12 ns are selected as beam-beam interactions. The correction factor for the background, F^{BB}, is calculated as

$$F_i^{\mathrm{BB}} \quad = \quad \frac{A_i}{T_i} \tag{4.15}$$

where T_i is the total number of triggered counts and A_i is the number of counts within the V0 timing window registered during the given time interval i. The interaction rate corrected by
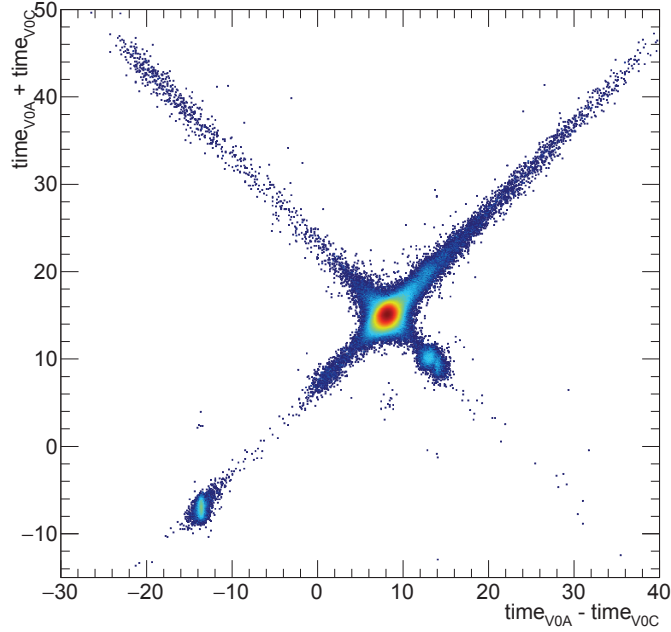
Figure 4.2: Correlation between the sum and difference of signal times in V0A and V0C. Three classes of events collisions at (8.3 ns, 14.3 ns), background from Beam 1 at (-14.3 ns, -8.3 ns), and background from Beam 2 at (14.3 ns, 8.3 ns) can be clearly distinguished.

the beam background correction factor, R_{BB}, is expressed by

$$R_i^{\mathrm{BB}} = F_i^{\mathrm{BB}} R_i^{\mathrm{Raw}}. \tag{4.16}$$

The correction factor F^{BB} results of the minimum-bias trigger as a function of beam separation are shown in Figure 4.5 (blue circles). The contribution of the background with large separation is larger than the small separation because the beam-beam interaction rate gets smaller with large separation, on the other hand, the beam-gas interaction rate is not influenced by the beam separation length. Furthermore, the shape of the vertical scan is different from the horizontal scan because, for the vertical scan, the satellite-charge effect also contributes the measured trigger rate.

Pile-up

The interaction rate is calculated as

$$R = \mu \cdot n_{\mathrm{BC}} \cdot f_{\mathrm{rev}}^{\mathrm{LHC}} \tag{4.17}$$

here μ is the average number of interactions per one bunch crossing and n_{BC} is the number of bunch crossing in one round. The probability of collisions in each bunch crossing is independent. Therefore, the probability is governed by Poisson statistics. Subsequently, when the number of interactions is a certain k, the probability follows

$$P(X = k) = \frac{\mu^k e^{-\mu}}{k!}. \tag{4.18}$$

From this point, the measured interaction rate is described as

$$R^{\mathrm{BB}} = (1 - e^{-\mu_{\mathrm{BB}}}) \cdot n_{\mathrm{BC}} \cdot f_{\mathrm{rev}}^{\mathrm{LHC}} \tag{4.19}$$
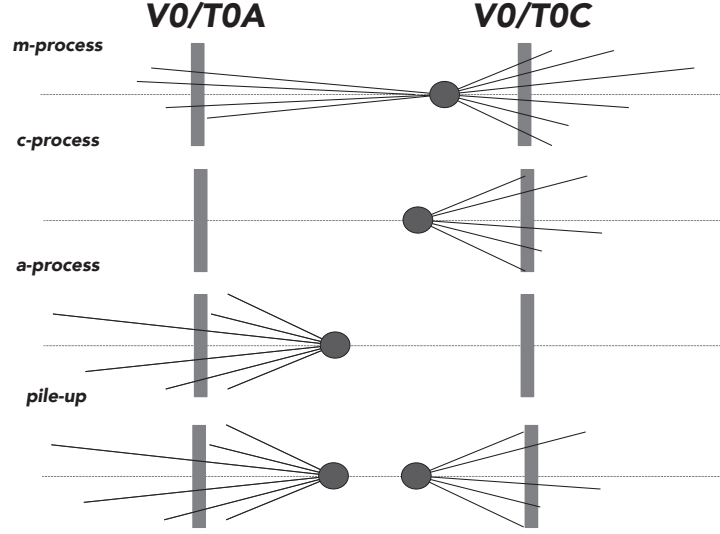
Figure 4.3: The interaction scenarios.

where R^{BB} and μ_{BB} are the trigger rate and probability corrected by the background correction factor (Equation 4.16). Hence, the following correction factor is applied to rate to correct the pile-up effect.

$$F_i^{\mathrm{pile-up}} = \frac{\mu_{\mathrm{BB}}}{(1 - e^{-\mu_{\mathrm{BB}}})} \tag{4.20}$$

In addition to the simple pile-up effect, there is one more effect related to the pile-up. The interaction scenarios are shown in Figure 4.3. The top three configurations are all single collision event per one bunch crossing. The top one, m-process can fulfill the minimum-bias trigger requirement. On the other hand, second and third, c-process and a-process, indicate that one collision occurs but the particles hit only one side array, e.g. single-diffractive event. These two processes can not fulfill the trigger requirements. However, when these both processes occur simultaneously and one hits the A-side and the other hits the C-side (fourth figure in Figure 4.3), the event fulfills the trigger requirements. The additional pile-up effect like the fourth configuration is not considered in the simple pile-up correction. The probability of the "true" m-process can be calculated as

$$R_i^{\mathrm{m}}/f_{\mathrm{rev}}^{LHC} = 1 - e^{\mu_{\mathrm{BB}}} + e^{\mu_{\mathrm{BB}}}(1 - e^{\mu_a})(1 - e^{\mu_c}) \tag{4.21}$$

where the subscript of BB, c and a indicate the rate of trigger corrected by the background correction factor, c- and a- processes, respectively. Naturally, the relationship between ratio of the triggered process, BB, and the other c-process, a-process holds

$$\frac{\mu_{c(a)}}{\mu_{\mathrm{BB}}} = \frac{\sigma_{c(a)}}{\sigma_{\mathrm{BB}}} = \frac{R_{c(a)}}{R_{\mathrm{BB}}} = r_{c(a)} \ (const.) \tag{4.22}$$

The m-process rate can be expressed with above ratios as

$$R_i^m/f_{\mathrm{rev}}^{\mathrm{LHC}} = 1 - e^{-\mu_{\mathrm{BB}}} + e^{-\mu_{\mathrm{BB}}}\left(1 - e^{-r_c\mu_{\mathrm{BB}}}\right)\left(1 - e^{-r_a\mu_{\mathrm{BB}}}\right). \tag{4.23}$$

These r_c and r_a are measured by using the very low intensity run and they are found to be $r_c = 0.0725$ and $r_a = 0.0725$ with negligible uncertainty. The interaction rate corrected by the all pile-up effect, R_i^{PU}, is written as

$$R_i^{\mathrm{PU}} = F_i^{\mathrm{pile-up}} R_i^m. \tag{4.24}$$

The total pile-up effects are shown in Figure 4.5 (red circle). The large pile-up contribution can be seen at small separation because the pile-up probability is proportional to the density of the overlapping region.

Beam Intensity Decay

The population of protons in bunches decreases with time due to collisions. Therefore, the event rate becomes smaller over time. The event rate has to be normalized by the time-dependent correction factor.

The population in a bunch is described as the intensity. The intensity is defined as the number of particles per unit time and per unit area. The decreasing of the beam intensity is called the beam intensity decay. The intensity of each bunch is measured by the LHC and ATLAS instrumentation. In case of the LHC, a DC current transformer (DCCT [60]) measures the total beam charge. Then, a fast beam current transformer (fBCT [60]) measures the fraction of the charge in each bunch. The charge fraction in each bunch is also measured by the ATLAS beam pick-up system (BPTX [59]). The difference between fBCT and BPTX is taken into account for the systematic uncertainty. The intensity measured by DCCT and fBCT of each beam is shown in Figure 4.4.
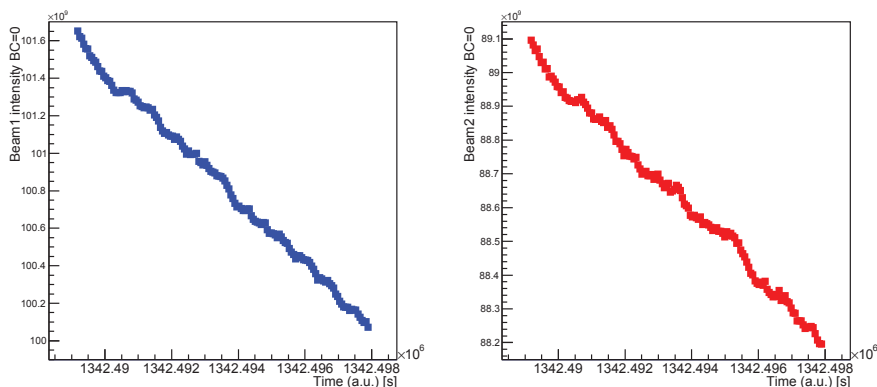
Figure 4.4: Bunch intensity as a function of time for a representative bunch crossing.

In the measurement of beam intensity, the contribution of satellite-charge and ghost-charge should be taken into account. The radio-frequency (RF) configuration of the LHC is divided into 3564 slots of 25 ns each. Each slot is further divided into 10 so-called buckets of 2.5 ns each. All particles in one slot are supposed to be captured in the central bucket. However, some particles are put in the other buckets. The charges in the wrong bucket are called satellite-charges, and the charges in the bunch slot which is supposed to be empty are called ghost-charges. The measured intensity includes these satellite and ghost charges, but these charges don't participate in the collisions. From this standpoint, a fraction of ghost-charges and satellite-charges have to be known.

These charges are measured quantitatively by the LHCb collaboration and the LHC during the operating the scan. The LHCb collaboration measures ghost-charges via the rate of collisions occurring in nominally empty bunch slot crossings. The LHC measures satellite-charges via synchrotron radiation photons emitted by the beams by Longitudinal Density Monitor (LDM) [61]. The ghost-charges and satellite-charges correction factors to the bunch intensity are 0.989±0.002 and 0.9930±0.0003, respectively.

The assumption that the decay can be described by an exponential distribution (F_{exp}) is

considered to correct this effect. The correction factor for the decay intensity, F_i^{ID}, is given by

$$F_i^{\mathrm{ID}} \quad = \quad \frac{F_{exp}(t_N)}{F_{exp}(\bar{t})} \tag{4.25}$$

where $\bar{t}$ is the average time in the time period i and t_N is the time to chosen to normalize the rate. The timestamp between the horizontal scan and vertical scan are chosen to normalize t_N. This correction factor is applied to R_i^{PU} as below.

$$R_i^{\mathrm{DC}} = F_i^{\mathrm{ID}} R_i^{\mathrm{PU}}. \tag{4.26}$$

The correction factor F^{ID} results as a function of the separation are shown in Figure 4.5 (green circles).
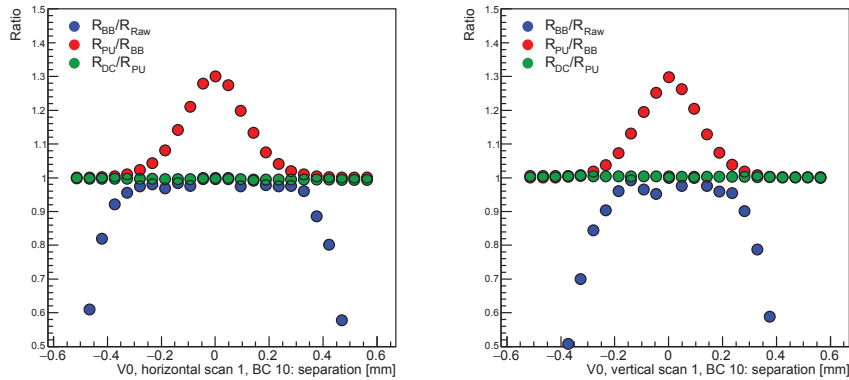
Figure 4.5: Ratios for the rate before and after each correction for a typical interacting bunch crossing during the horizontal scan (left) and vertical scan (right). The ratio of background corrected rate to the raw rate is shown in blue, the ratio of the pile-up corrected rate to the background corrected rate in red and the ratio of the decay corrected rate to the pile-up corrected rate is in black.

4.1.8   Beam Separation

Length Scale Calibration

The value of the nominal separation of the beam centres during the scan is given by the LHC. During the horizontal and vertical scans, there are 25 steps in each scan. However, these values are estimated by calculating with information of the steering magnet current. Therefore, the special run to measure a correlation between nominal separation (reported by the LHC) and real separation is needed (LSC: Length Scale Calibration). During the scan beam 1 and beam 2 are moved to opposite direction each other, but during LSC run beam 1 and beam 2 are moved in the same direction. When both beams are moved to the same direction, the beam collision position moves in the same direction. The vertex position as a function of time during the LSC measured by the ALICE detector is shown in Figure 4.6. There are 5 steps in the LSC run for each direction. The correlation between the nominal and real measured by the ALICE detector is shown in Figure 4.7. The correlations are fitted with linear (1st order polynomial) function. The fitting result is used as a conversion factor between the current in the steering magnets and the beam displacement.
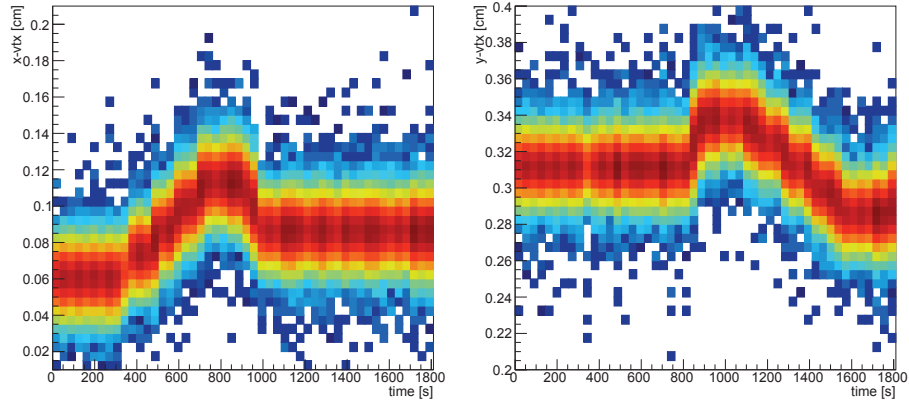
Figure 4.6: Time dependence of measured collision vertex during the horizontal scan (left) and vertical scan (right).
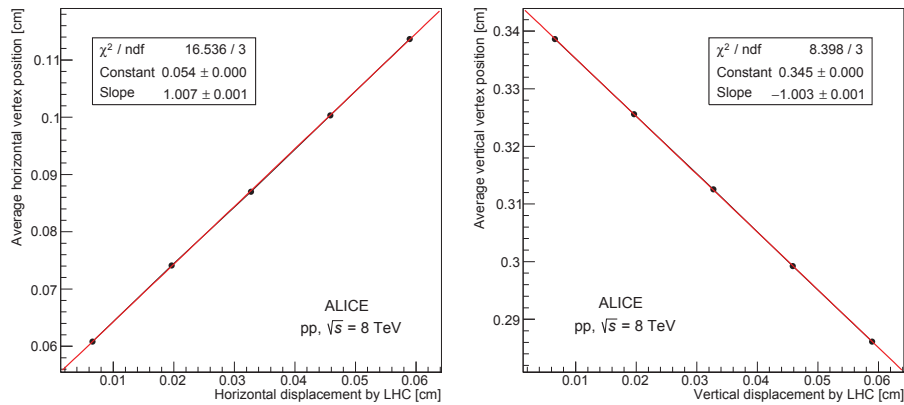
Figure 4.7: Step positions estimated from the fits to vertex distributions as a function of the step reported by the LHC for the period where the beams were displaced in the horizontal (left) and vertical (right) directions.

Orbit Drift

Possible variations of the reference orbit during the scan may lead to wrong beam separation. In order to quantify a possible bias, the data from the LHC Beam Position Monitors (BPM) [62] are used to extrapolate the transverse coordinates of the orbit beams.

The transverse orbit drift is shown in Figure 4.8, black and light-green. The time intervals in the hatched areas where the beam position monitors are unreliable due to vdM-scan. The rest of the points have been used to fit the behavior of the orbit drift. The definition of the functions used in the analysis is

$$\begin{aligned} f_{\text{vertical}} &= p_0 + p_1(t - t_0) + p_2(t - t_0)^2 + p_3(t - t_0)^3 + p_4(t - t_0)^4 & (4.27) \\ f_{\text{horizon}} &= p_0 + p_1(t - t_0) + p_2(t - t_0)^2 & (4.28) \end{aligned}$$

where t_0 is a reference time. The correction of orbit drift is shown in Figure 4.9 (Green).
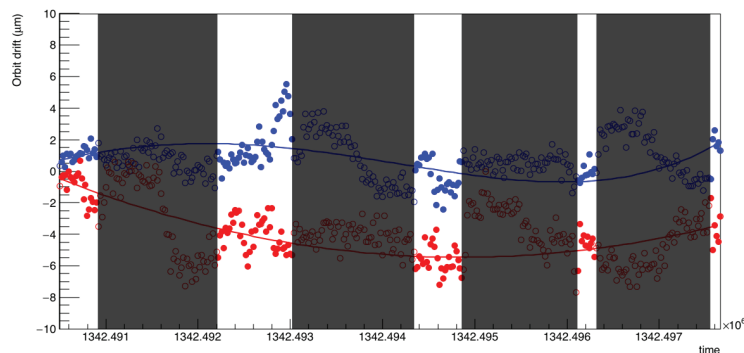
Figure 4.8: Orbit drift as a function of time. The hatched areas signal time intervals where the beam position monitors were not reliable. The lines represent fits to the points.

Beam-Beam Deflection (BBD)

Due to their electric charge, the two beams exert a repulsive force upon each other, modifying slightly the beam separation. The variations of the beam separation are calculated for each pair of interacting bunches with the MAD-X code [63], and using as an input the already orbit-drift corrected separations. The change of the nominal separations when the beam-beam deflection and the orbit-drift corrections are taken into account is shown in Figure 4.9 (blue). The correction factor depends on the magnitude of separation length and so the shape is symmetric with respect to the center.

4.1.9 Effective Beam Width

The area effective beam width, $\Sigma_{x(y)}$, can be calculated with above full corrected trigger rate and separation length. It is the area under the curve given by the corrected rate as a function of the separation of the beam centers Equation 4.10. It can be computed numerically or fitting the data with some model.

Numerical method

In the numerical case, one adds the area of rectangles with height given by the rate at a given separation and a base starting at the mid-point between the given separation and its predecessor and ending at the mid-point between the given separation and the next one. In proton+proton
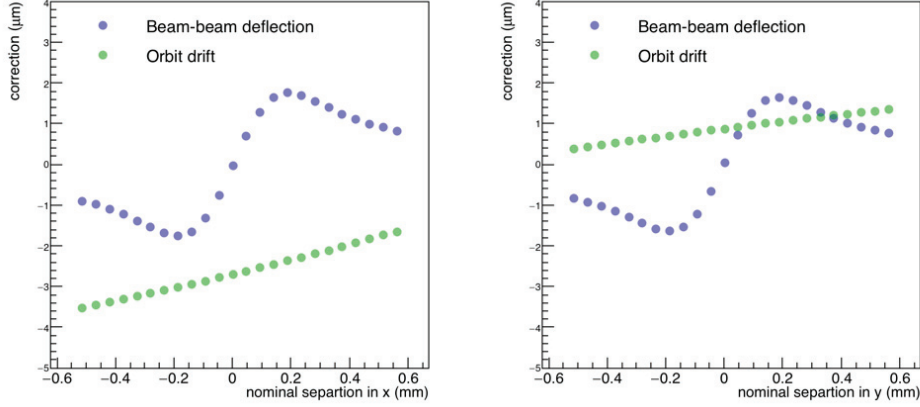
Figure 4.9: Size of corrections from the nominal separations to the orbit-drift corrected separation (green and black markers) and from these last to separations also corrected for beam-beam deflection (blue and red markers) as computed using information from the T0 (blue and black markers) and V0 (red and green markers) reference processes for the horizontal (left panel) and vertical (right panel) parts.

collisions, the precision of this method tends to be smaller than that of fitting, because the subtraction of background may give a large contribution to the error of the individual rates. The statistical error of the rates at each separation is propagated in the standard way to an error in the area.

Fit models

Two models have been used. The one that has proved to be more stable is a product of a Gaussian distribution and a sixth order polynomial (GP6) taking into account only the even coefficients because the fits yield that the even components are compatible with zero:

$$\Sigma_x(x) = N e^{-\frac{(x-\mu_x)^2}{2\sigma}} \left(1 + p_2(x-\mu_x)^2 + p_4(x-\mu_x)^4 + p_6(x-\mu_x)^6 \right), \tag{4.29}$$

where x stands for the separation of the beam centres in x while the coordinate y is fixed, while N, m, s and p_i are given by the fit. A similar formula is valid for $\Sigma_y(x)$. This model provides the central values used in the analysis.

An alternative model is given by the double Gaussian (DG) distribution

$$S_x(x) = N(\omega G_1(x) + (1-\omega)G_2(x)); \tag{4.30}$$

where

$$G_i(x) = \frac{1}{\sqrt{2\pi\sigma}} \exp\left(-\frac{(x-\mu_x)^2}{2\sigma_i^2} \right), \ i = 1, 2 \tag{4.31}$$

and $\sigma_2 = \sigma_1 + \Delta$.

An example of fits using Equation 4.29 to the rate as a function of separation is shown in Figure 4.10. In both cases, the error on the area comes from the error on the integration of the fit function over the range in separations and takes into account the error on the parameters and the correlation among them.
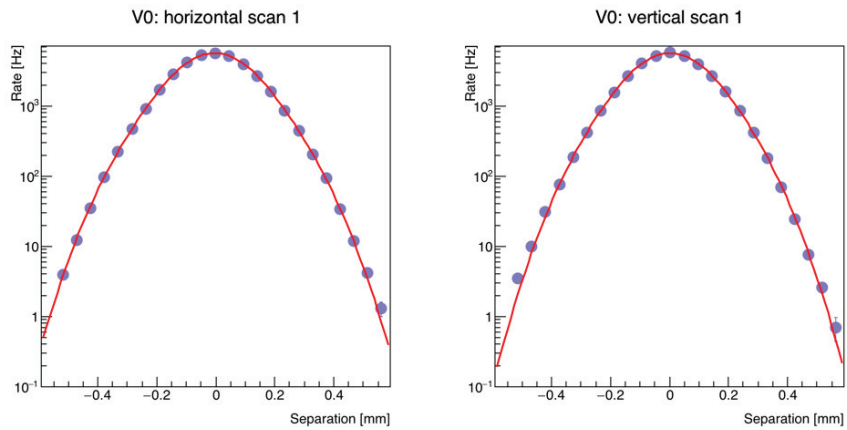
Figure 4.10: GP6 fits, according to Equation 4.29, to the rates as a function of separation, for fully corrected rates and separations, for a typical interacting bunch crossing during the horizontal (left panels) and vertical (right panels) steps of the first scan.

In the numerical method, the head on rate is assumed to be equal to the rates at the separation closest to zero. Using a model, the head-on rates are obtained from the fit. The error on the head-on rates from the numerical method is just the error on the corresponding rate, while for the fit models, the error on the normalization parameter is scaled to correspond to the head-on rate and assigned to it.

4.1.10 Systematic Uncertainty

In this analysis, following systematic uncertainty sources are considered.

Systematic uncertainties related to the bunch intensity

Basically, uncertainties related to the intensity is provided by the LHC and the ATLAS experiment.

- The uncertainty on the factor from the DCCT to normalize the fBCT is 0.3%.

- The bunch intensity is measured by two devices, fBCT and BPTX. The difference between them can be negligible.

- The uncertainty on the correction for ghost charges and satellite charges are 0.04% and 0.03%, respectively, reported by the LHC.

- Due to their electric charges the beams (de-)focus each other, and the strength of this effect, called dynamic β^* depends on the beam separation and may alter the effective beam width. To estimate the potential uncertainty from this effect, the bunch crossing with the largest intensity in fill 2852, bunch slot 3304 is studied. With this procedure correction factors to the rate at each separation are obtained. With these factors, a new cross section for this bunch crossing is computed. The ratios of these new cross section to the cross sections computed without using these factors, 1.00646 (first scan) and 1.00692 (second scan). The uncertainty is thus of the order of 0.7%.

Systematic uncertainties related to the separations

The cross-section has been computed using the beam-beam deflection corrected separations presented in Section 4.1.8. The beam-beam deflection is computed taking into account the orbit-drift correction. The ratio of these cross sections, evaluated using the GP6 model.

- To evaluate the effect of the orbit-drift correction to studies are carried out: The systematic uncertainty related to orbit drift is estimated by the comparison of the cross sections computed with the correction for beam-beam deflection for the cases when the orbit-drift correction is or isn't applied. The average of the parameters for the constant fit for the two scans is 0.3%.

Systematic uncertainties related to the rate

- To study the dependence on the size of the windows chosen to differentiate the signal from the background using the V0 detector. The window is modified to be checked: to cover from 12.0 to 17.0 ns, for the sum of the timing from V0A and V0C, while the time difference was set to be between 6.0 and 11 ns. The uncertainty associated with the window chosen for background reduction is 1.2%.

- To study the dependence on the pile-up correction, the parameters were either increased or decreased by 10% and the resulting cross sections are compared to the default case. The uncertainty associated with this is negligible.

Source	Uncertainty
Non-factorisation	1.2%
Orbit drift	0.3%
Beam-beam deflection	0.7%
Dynamic β^*	0.7%
Background subtraction	1.2%
Pileup	< 0.1%
Length-scale calibration	0.3%
Fit model	0.3%
$h_x h_y$ consistency	<0.1%
Luminosity decay	0.7%
Bunch-by-bunch consistency	<0.1%
Scan-to-scan consistency	< 0.1%
Beam centering	< 0.1%
Bunch intensity	0.4%
Total on visible cross section	2.19%
Stability and consistency	1.4%
Total on luminosity	2.60%

Table 4.1: Relative uncertainties on the measurement of visible cross sections and luminosity in pp collisions at $\sqrt{s} = 8$ TeV.

- To study the dependence on the decay of the bunch intensity the corresponding correction is modified by adding the error obtained from the linear fit to the bunch intensities and the rates are computed using this new correction. The associated uncertainty is negligible.

- In Equation 4.14, it is stated that the rate at zero separation is taken as the average of the head-on rates from the vertical and horizontal parts of the scan. The largest deviation is 0.8% and this is assigned as systematic uncertainty.

Systematic uncertainties related to the computation of the effective beam width

- The uncertainty related to the method to calculate effective beam area is estimated by comparison of the cross-section from the numerical method and the fit model (GP6 and DG). The maximum variation, 0.4% has been assigned as systematic uncertainty.

- To estimate the uncertainty of head-on rate, the fits are also evaluated at nominal zero separation. The associated uncertainty is negligible.

Systematic uncertainties related to cross section variations

- Figure 4.11 shows the cross sections as a function of the product of bunch intensities. In all cases, the bunch intensities from fBCT, the separations corrected for beam-beam deflection and the GP6 model have been used. Fits to constants are also shown for each set of cross sections. To compensate for the large χ^2 we have added a 0.6% uncertainty.

Summary of systematic uncertainties

The systematic uncertainties are summarised in Table 4.1.

4.1.11 Cross-Section of Minimum-Bias Trigger ($\mathrm{MB_{AND}}$)

The cross section is calculated for each interacting bunch crossing for each of the reference process. Then, a cross-section at the scan level is produced, by the weighted average of the cross sections for each interacting bunch crossing, where the weight uses only the statistical uncertainty.

The cross sections are evaluated using the bunch intensities from fBCT, the separations corrected for beam-beam deflection and the GP6 model. The cross sections for the minimum-bias trigger in each scan are

$$\sigma_{\mathrm{MB_{AND}}}(\mathrm{Scan1}) \quad = \quad 55.79 \pm 0.05 \mathrm{mb} \tag{4.32}$$

$$\sigma_{\mathrm{MB_{AND}}}(\mathrm{Scan2}) \quad = \quad 55.70 \pm 0.05 \mathrm{mb}. \tag{4.33}$$

The weighted mean of the cross sections for each scan, adding in quadrature the systematic uncertainty is

$$\sigma_{\mathrm{MB_{AND}}} \quad = \quad 55.75 \pm 0.03(\mathrm{stat.}) \pm 1.4(\mathrm{syst.})\mathrm{mb}. \tag{4.34}$$
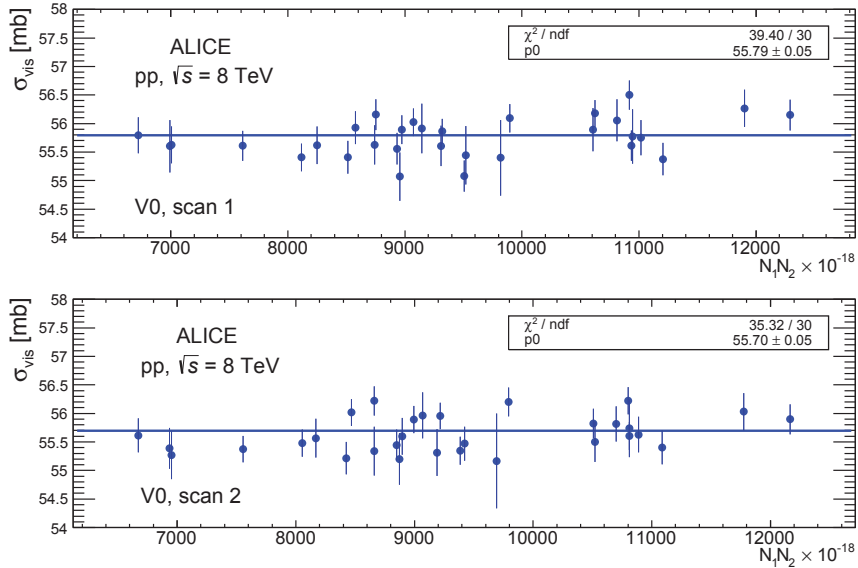
Figure 4.11: Cross sections as a function of the product of bunch intensities for the first (upper panel) and second (lower panel) scans. The lines are fits a constant. In all cases the bunch intensities from fBCT, the separations corrected for beam-beam deflection and the GP6 model have been used.

4.2 Event Multiplicity Estimator

In this analysis, the charged particle multiplicity is used to classify the event. The event is classified the sum of the V0-A and V0-C multiplicity as an event activity. The multiplicity distribution measured by the V0-A and V0-C is shown in Figure 4.12.

The number of tracklets in a unit pseudo-rapidity ($|\eta_{\mathrm{lab}}| < 1.0$) measured by the SPD detector is used to determine the multiplicity at mid-rapidity. Two layers of SPD are covering
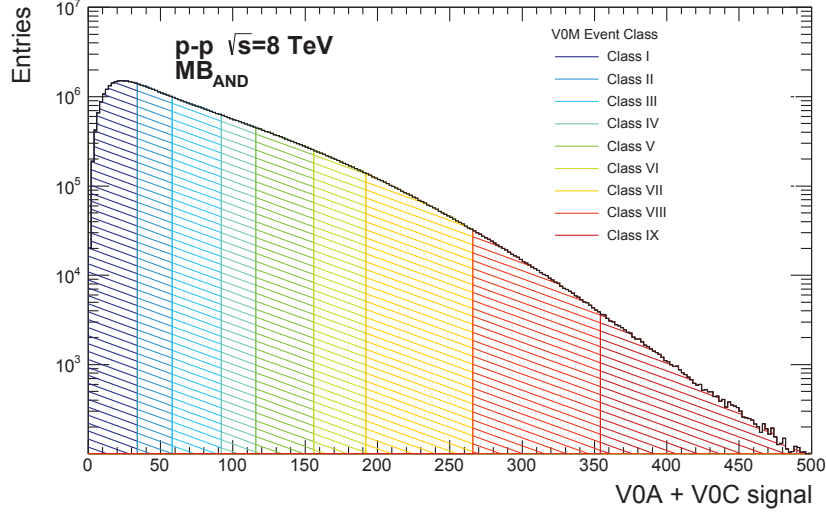
Figure 4.12: Reconstructed tracklets as a function of the event reconstructed Z_{vtx} position and tracklets.

$|\eta| < 2.0$ (first layer) and $|\eta| < 1.4$ (second layer), respectively. However, its covering pseudo-rapidity area depends on the primary vertex position along the beam axis and the detector conditions during the data taking. Therefore, the detector response should be equalized to estimate the multiplicity event-by-event. The variation of the SPD acceptance as a function of the primary vertex position along the beam axis is shown in Figure 4.13. The acceptance is influenced by the z vertex position. Therefore, the event multiplicity dependence on the z vertex position is seen in Figure 4.14 (right). To correct the effect, the correction factor as a function of the reconstructed vertex position is used. The data-driven correction factor is calculated as

$$N_{\text{tracklets}}^{\text{corrected}}(z_{vtx}) \;=\; N_{\text{tracklets}}^{\text{uncorrected}}(z_{vtx}) \cdot \frac{N_{\text{tracklets}}^{\text{ref}}}{\langle N_{\text{tracklets}}^{\text{uncorrected}}(z_{vtx}) \rangle} \tag{4.35}$$

$$=\; N_{\text{tracklets}}^{\text{uncorrected}}(z_{vtx}) + \Delta N \tag{4.36}$$

where

$$\Delta N = N_{\text{tracklets}}^{\text{uncorrected}}(z_{vtx}) \cdot \frac{N_{\text{tracklets}}^{\text{ref}} - \langle N_{\text{tracklets}}^{\text{uncorrected}}(z_{vtx}) \rangle}{\langle N_{\text{tracklets}}^{\text{uncorrected}}(z_{vtx}) \rangle} \tag{4.37}$$

where $N_{\text{tracklets}}^{\text{ref}}$ is the number of tracklets chosen as the reference which is determined by using MC simulation, $\langle N_{\text{tracklets}}^{\text{uncorrected}}(z_{vtx}) \rangle$ is the mean value of the multiplicity as a function of the primary z vertex position which is shown in Figure 4.14. In this procedure, the Poisson statistics are employed to get an integer of ΔN.   The corrected multiplicity distribution estimated by the SPD tracklets of two different triggered data are shown in Figure 4.15. Each value related to the multiplicity is summarized in Table 4.2.

4.3   PHOS Detector Performance

4.3.1   Cluster Finding Algorithm

The PHOS detector is composed of 3 modules, each module has 3584 (64×56) cells. When photons and electrons/positrons enter the PHOS, they generate electromagnetic showers. The
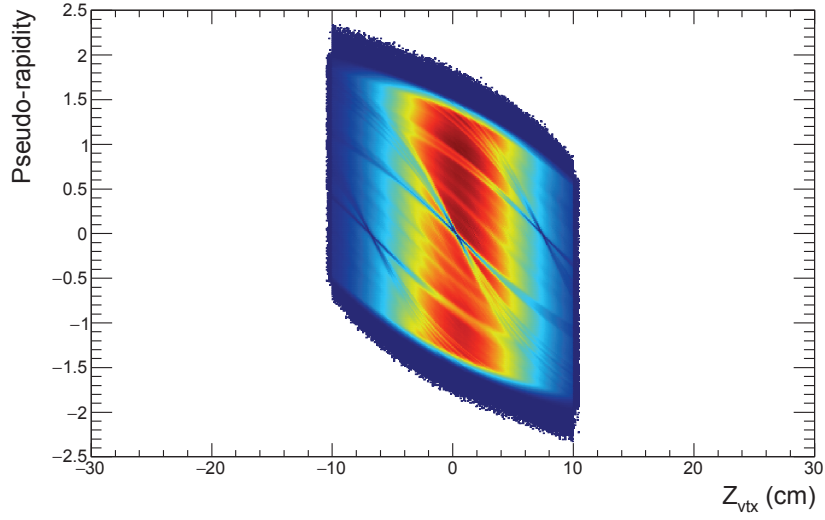
Figure 4.13: Distribution of the V0 amplitude (sum of V0-A and V0-C).
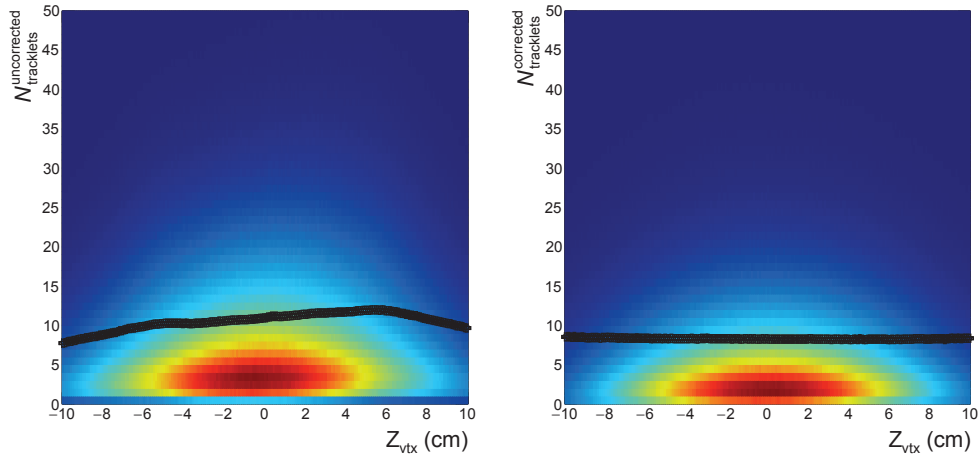
Figure 4.14: Raw multiplicity distribution ($N_{\mathrm{tracklets}}$ measured within $|\eta| < 1.0$) as a function of z_{vtx} (left). Corrected multiplicity distributions ($N_{\mathrm{tracklets}}$ measured within $|\eta| < 1.0$) by Equation 4.36 as a function of z_{vtx} (right).
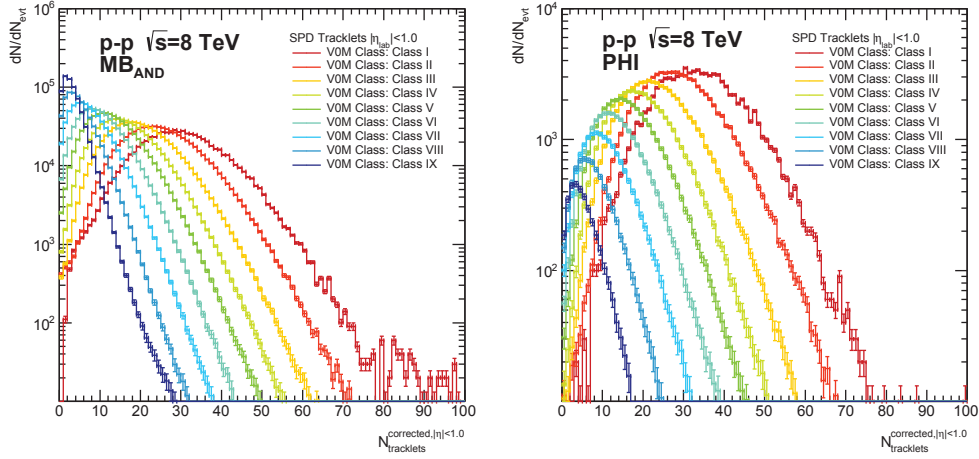
Figure 4.15: Corrected tracklet multiplicity ($|\eta| < 1.0$) in each event class defined by the V0M event class estimator.

V0M Class (%)	$\langle N_{\mathrm{tracklets}} \rangle$	$\langle \mathrm{V0M_{signal}} \rangle (\mathrm{a.u.})$	$\frac{dN_{\mathrm{ch}}/d\eta}{\langle dN_{\mathrm{ch}}/d\eta \rangle}\big|_{central}$	$\frac{dN_{\mathrm{ch}}/d\eta}{\langle dN_{\mathrm{ch}}/d\eta \rangle}\big|_{forward}$
Class I	29.13 ± 0.04	396.57 ± 0.12	3.8 ± 0.4	5.15 ± 0.12
Class II	24.582 ± 0.011	302.19 ± 0.03	3.2 ± 0.2	3.92 ± 0.04
Class III	19.509 ± 0.005	226.530 ± 0.012	2.53 ± 0.14	2.94 ± 0.02
Class IV	15.869 ± 0.004	177.084 ± 0.006	2.06 ± 0.11	2.30 ± 0.02
Class V	12.654 ± 0.002	138.127 ± 0.004	1.64 ± 0.09	1.794 ± 0.013
Class VI	9.8236 ± 0.002	106.264 ± 0.003	1.28 ± 0.07	1.380 ± 0.010
Class VII	7.0671 ± 0.0012	74.567 ± 0.003	0.92 ± 0.05	0.968 ± 0.007
Class VIII	4.6558 ± 0.0010	46.441 ± 0.002	0.60 ± 0.03	0.603 ± 0.005
Class IX	2.8862 ± 0.0006	21.751 ± 0.002	0.37 ± 0.02	0.282 ± 0.003
MB	7.700 ± 0.007	77.000 ± 0.007	1	1

Table 4.2: Relative uncertainties on the measurement of visible cross sections and luminosity in pp collisions at $\sqrt{s} = 8$ TeV.

showers spread their energies over adjoining cells. The aggregate cells created by one particle is called a cluster.

The cluster-finding algorithm starts from seed cells with energy above the threshold E_{seed} which depends on the event environment. The occupancy of the PHOS detector is low in proton+proton collisions, so the probability of showers overlapping is small. The energy threshold is set to $E_{\text{seed}} = 200$ MeV which is slightly below the MIP in proton+proton collisions. On the other hand, the occupancy of the detector is high in Pb-Pb collisions, higher energy threshold $E_{\text{seed}} = 400$ MeV is applied. After finding the seed, adjacent cells with energy above E_{min} are added to the group. The E_{min} doesn't depend on the event environment and is set $E_{\text{min}} = 15$ MeV in all collision systems. The cluster energy is calculated as

$$E = \sum_{i}^{N_{cell}} e_i, \tag{4.38}$$

where the e_i is amplitude of each cell. The cluster position on the detector surface is calculated by taking the center of gravity with a logarithmic weight into account as,

$$\overline{s} = \frac{\sum s_i w_i}{\sum w_i}, \qquad w_i = \max\left[0, 4.5 + \log\left(\frac{e_i}{E}\right)\right] \tag{4.39}$$

where the $\overline{s}$ is cluster position, s_i is the each cell position (x_i, z_i) and E is the cluster energy represented in Equation 4.38. The value 4.5 is determined empirically by the knowledge of electromagnetic shower profile [2, 48].

4.3.2 Quality Assurance

Good Cell Selection

Three PHOS modules are installed in 2012 and each module has 64×56 cells, totally 10752 cells. The module #2 are not stable during 2012 runs. Therefore, the module #2 is excluded from this analysis at all. Module #1 and #3 have 3584 cells each, but during data taking period, due to several reasons, some cells are not good condition and these cells have to be found and removed from the analysis. The cluster occupancy shown in Figure 4.16 is used to find bad cells with a certain period of time. The cells which greatly differ from the mean occupancy are defined as bad cells. The bad cell maps for module #1 and #3 during a given period are shon in Figure 4.17. The red area indicates a bad cell position which is masked in the analysis. The five bad maps are created for given five periods.

PHOS Stability

After applying global event selection (Section 4.1.2) and bad PHOS maps (Section 4.3.2), the PHOS condition stability is checked with the mean cluster energy $dE_{\text{cluster}}/dN_{\text{cluster}}$ and the average number of clusters per an event $dN_{\text{cluster}}/dN_{\text{evt}}$. These are shown in Figure 4.18. The mean cluster energy of each module is about 0.6 GeV and both modules are stable. On the other hand, there are some bumps in the average number of cluster per one event figure. These are due to bad map difference because the average number of cluster is proportional to the acceptance.

4.3.3 Energy Calibration

The energy calibration is carried out with the E/p ratio method and π^0 mass peak position method. these two methods are explained as follows.
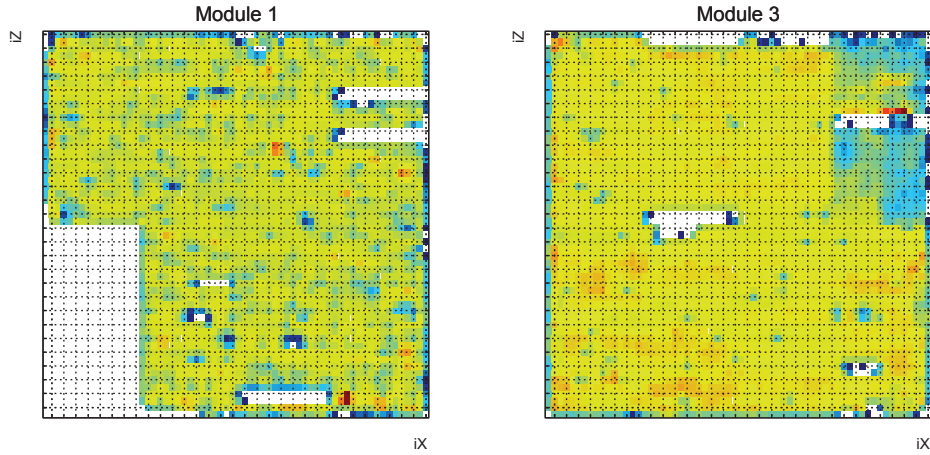
Figure 4.16: Cluster occupancy for a given period (z axis is logarithmic.).   The left one is module 1 and right is module 3.
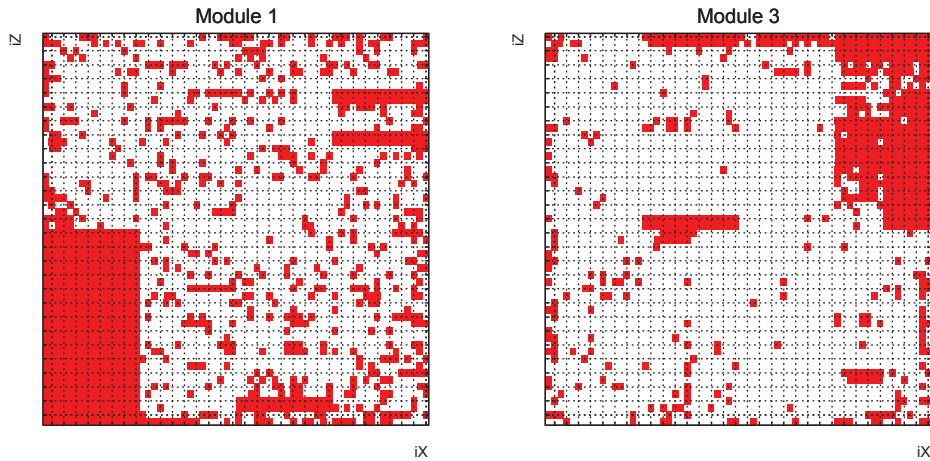
Figure 4.17: Bad maps for a given period. The left one is module 1 and right is module 3.

E/p ratio method

The E/p ratio is the ratio of the cluster energy measured by the PHOS and the track momentum reconstructed by the tracking system. If the track is electrons/positrons, the E/p ratio should be unity because they also deposit their all energy in the calorimeter as well as photons. The tracks are identified by dE/dx (ionizing energy loss) information by the TPC. The deviation from the nominal electron/positron dE/dx as a function of the momentum measured by TPC is shown in Figure 4.19. The tracks used for the study require that they across the over 60 read-out points of the TPC and have at least 60% of findable TPC clusters to ensure good track quality. To select electron/positron tracks, the dE/dx is required to be within $-1< n\sigma_{e^\pm} <3$ where $\sigma_{e^\pm}$ is an expectation of the energy loss by electrons/positrons. The widow size is also shown as dashed line in Figure 4.19.

The E/p ratio given an energy bin is shown in Figure 4.20 (left panel). There is still hadron contamination in the ratio with above criteria. The hadron contributions can be estimated by
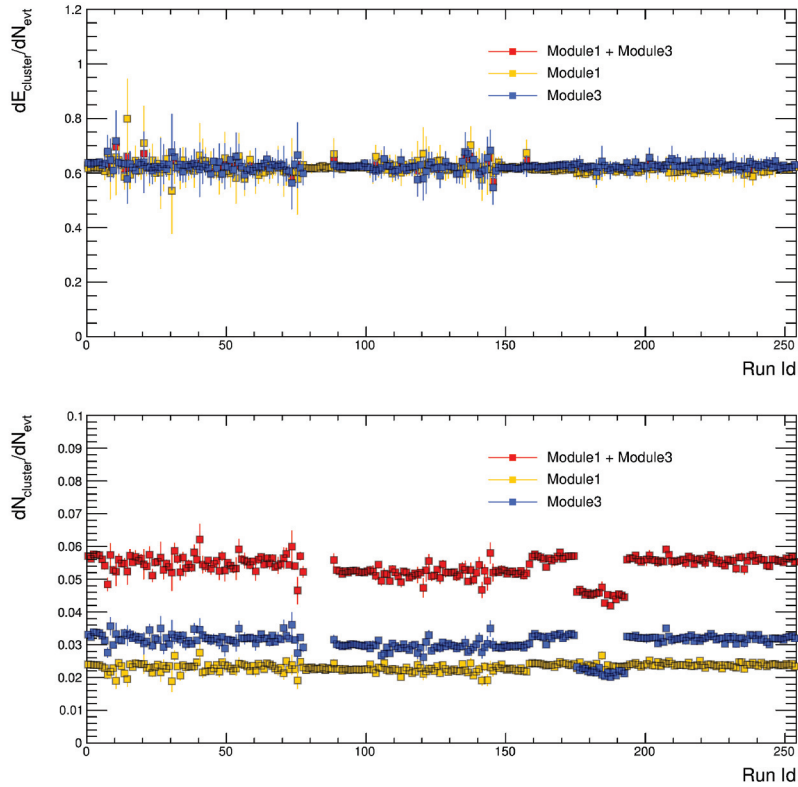
Figure 4.18: The number of cluster per one event and the average energy of cluster energy as a function of run number (time).

using tracks satisfying the deviation from electron energy loss expectation of $n\sigma_{e^\pm} < -3.5$. The estimated contribution of the hadron contamination is shown as the blue histogram in Figure 4.20. After subtraction of the hadron contamination, the electron/positron E/p ratio peak can be seen and is shown as the black histogram.

By fitting the peak with the Crystal Ball function [64] (Equation 4.54), the energy calibration is carried out. The E/p ratio value as a function of the track transverse momentum is shown in Figure 4.20 (right). The value decreases at low momentum region due to calorimeter non-linearity effect. On the other hand, the ratio above 1.0 GeV/c is a little bit lower than unity (~ 0.99) because electrons/positrons lost their energy by the bremsstrahlung in the material between the TPC and PHOS. The resolution of tracking is better than calorimeter at low momentum region, so the non-linearity effect can be studied precisely. However, the electron/positron is a very rare probe, so it is difficult to obtain enough statistics. Furthermore, the material budget in front of the calorimeter related to the energy loss cannot be measured precisely especially between tracking system and the calorimeter.

Neutral Pion Mass Peak Position Method

This method uses invariant mass calculated from two clusters. The full detail of invariant mass calculation with two clusters is addressed in Section 4.4. The true mass of neutral pion is 134.9 MeV/c^2 [65]. The invariant mass distribution from two clusters given a transverse momentum bin is shown in Figure 4.21 (left). The Section 4.4 also gives a detail explanation of the method to estimate the background shape. The peak position of the neutral pion as
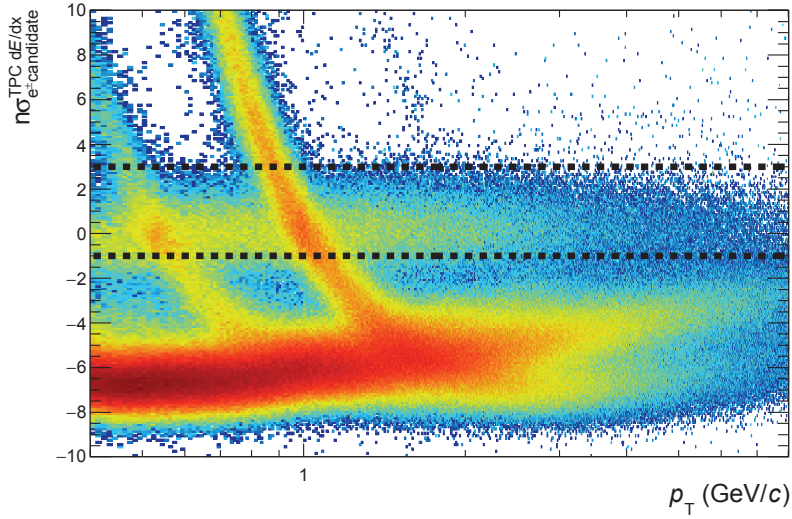
Figure 4.19: The difference of the measured dE/dx value from the hypothesis of the electron/positron energy loss is used for particle identification. The dE/dx of measured charged tracks is required to be within $-1 < n\sigma_{e^\pm} < 3$ of the expected energy loss (dashed lines).
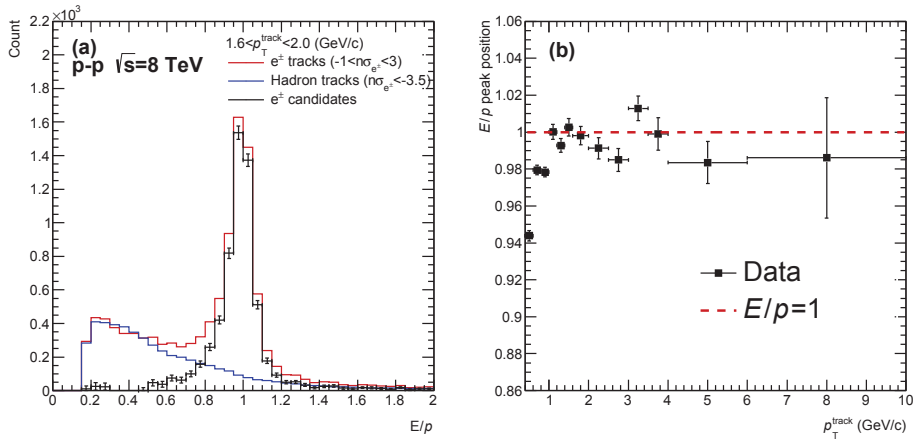
Figure 4.20: The E/p ratio of given transverse momentum bin (left). The peak position of E/p ratio as a function of the transverse momentum of the charged track reconstructed by TPC (right).

a function of transverse momentum is shown in Figure 4.21 (right). The mass peak position at low momentum region is lower than the true mass peak because of the non-linearity effect. Over 1.6 GeV/c, the peak position is consistent with the true mass position (red dashed line). It is easy to obtain enough statistics, so the calibration at high energy region can be improved easily. However, the mass peak position is calculated from two clusters. Therefore, it is difficult to calibrate cluster-by-cluster.
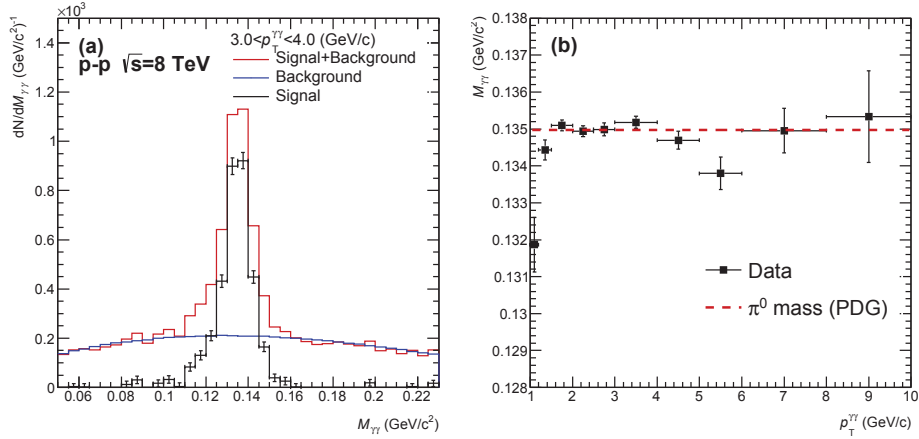
Figure 4.21: Invariant mass distribution calculated from two clusters measured by PHOS (left). Reconstructed mass peak position as a function of calculated transverse momentum (right).

4.3.4 Photon Identification

The clusters are generated by not only photons but also several kinds of particles. Some methods for reduction of contamination are explained below.

Energy and Number of Cells Cut

The energy cut of $E_{\text{cluster}} > 0.3$ GeV is applied to clusters. This cut works to reject the clusters induced by charged particles because the charged particles deposit their energy as MIP. The deposited energy of MIP is around 0.23 GeV in the PHOS. Therefore, the energy cut reduces the contamination of charged particles. The energy distribution of charged particles and neutral particles in MC simulation (Pythia 8 [100] + GEANT3 [71]) are shown in Figure 4.22. The charged particle distribution has a peak below 0.3 GeV, so the cut works to remove the clusters.

The number of cells cut is applied to reduce the exotic clusters. When charged particles enter the detector at right angles, they hit the detector electronics directly and cause nonphysical electric current flows. They create the cluster which is composed of a few cells, but only one cell has huge energy. To remove these clusters, the number of cells cut $N_{\text{cell}} > 3$ is applied. Furthermore, typically, the number of cells composing the cluster induced by electrical noise is below 3. Hence, this cut also reduces the noise contributions. This cut reduces the detection efficiency of photon below 2 GeV, but the photon purity is increased by the cut in these energy region. After applying the cut, the photon purity achieves about 60%. The effect of the cut is introduced in Section 4.3.4.

Cluster Shape Cut

The cluster shape on the detector surface is approximated as an ellipse and is expressed numerically as

$$\lambda_1 = \frac{s_{xx} + s_{zz}}{2} - \sqrt{\frac{(s_{xx} - s_{zz})^2}{4} + s_{xz}^2} \tag{4.40}$$

$$\lambda_2 = \frac{s_{xx} + s_{zz}}{2} + \sqrt{\frac{(s_{xx} - s_{zz})^2}{4} + s_{xz}^2} \tag{4.41}$$
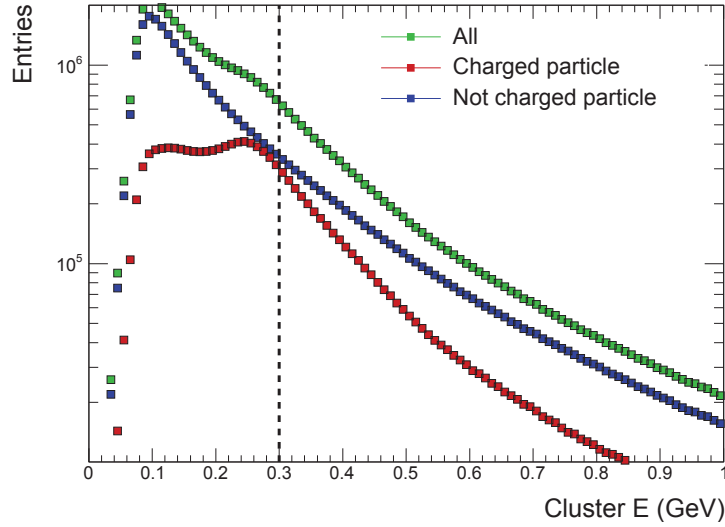
Figure 4.22: Cluster energy of total (green), charged particles (red) and neutral particles (blue).

where

$$s_{xx} = \frac{\sum w_i x_i^2}{\sum w_i} - \left(\frac{\sum w_i x_i}{\sum w_i}\right)^2 \tag{4.42}$$

$$s_{xz} = \frac{\sum w_i x_i z_i}{\sum w_i} - \frac{\sum w_i x_i \times \sum w_i z_i}{\left(\sum w_i\right)^2}. \tag{4.43}$$

here $x(z)_i$ is the position of cells composing the cluster in the $x(z)$ axis and w_i is the weight parameter as explained in Equation 4.39. The charged particles are bent by the ALICE-L3 magnet with a magnetic field of B = 0.5 T, so they enter the PHOS at an angle with the surface. Therefore, the clusters of charged particle tend to be an elliptic shape. On the other hand, the photon clusters tend to create circle shape clusters. To distinguish these clusters, the cluster momentum along the long axis (λ_2) is used. The momentum component along the axis of photons and charged particles is plotted in Figure 4.23. This cut reduces the detection efficiency, but the photon purity is increased at a whole energy region. The effect of the cut is discussed in Section 4.3.4.

Charge Particle Veto Cut

To reduce contamination more, the tracking system can be used. The charged particles can be reconstructed and their hit positions on the PHOS surface can be estimated by extending the tracks. If the track hit position is near the cluster, the cluster may be created by the reconstructed track. Therefore, the cluster created by a charged particle can be identified. The charged particles generate the signal in the calorimeter at a finite depth. Hence, the position of the cluster center is systematically shifted from the hit position of track which is extended to the PHOS surface in the bending coordinate. Knowing the shiftting distance as a function of the transverse momentum of charged track (Figure 4.24 shown in [2]), the clusters induced by the charged tracks can be identified. The cut efficiency and purity for photon are summarized in next section.
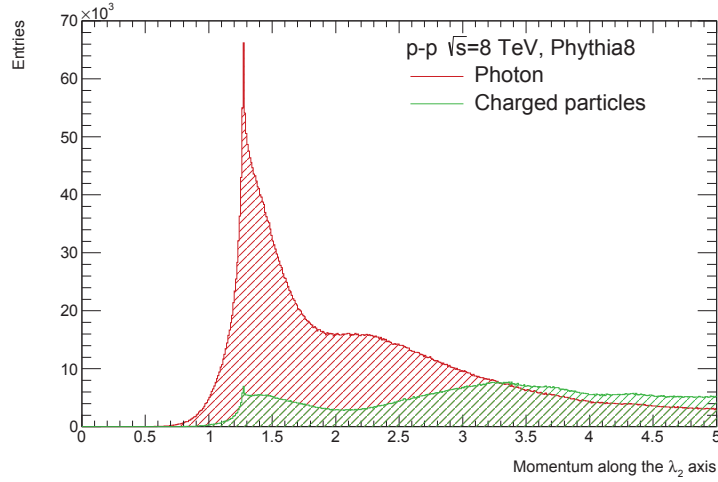
Figure 4.23: The momentum component along the long axis (λ_2) for cluster of photon (red) and charged particles (green).
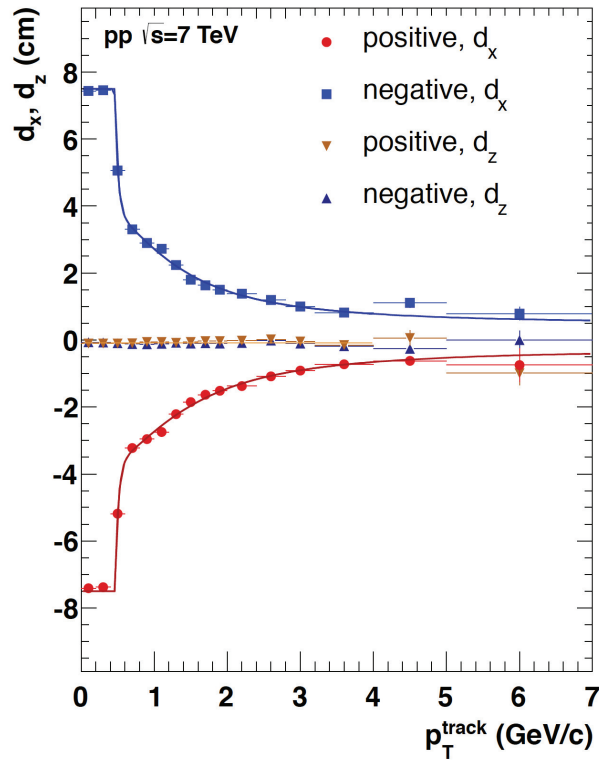
Figure 4.24: Mean track matching distance of PHOS and the lines are fitting results of phenomenological parameterizations [2].

Summary of Photon Identification and Efficiency

The photon detection efficiency and purity with and without above three cuts are shown in Figure 4.25. These are estimated by using MC simulation of the Pythia 8 and GEANT3
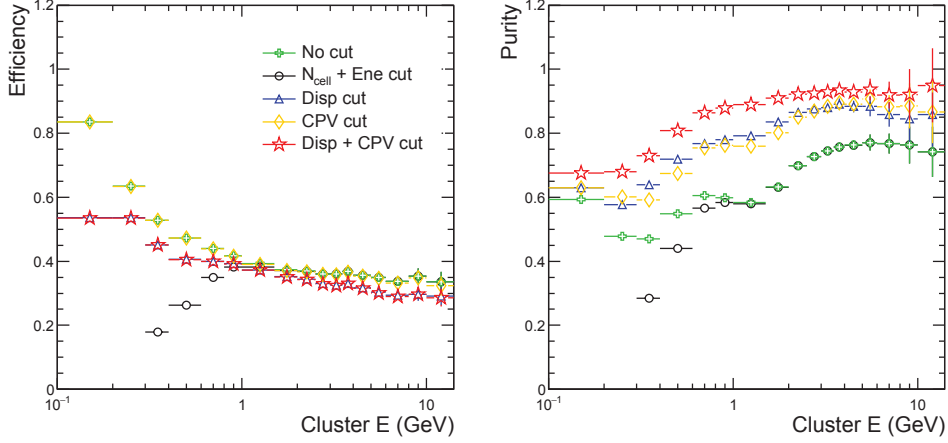
Figure 4.25: The efficiency and purity for photons as a function of reconstructed energy with several cuts.

framework. The efficiency is defined as

$$\varepsilon_{\text{photon}} = N^{\text{photon}}_{\text{cluster}} / N^{\text{photon}}_{\text{PHOS acceptance}} \tag{4.44}$$

and the purity is calculated as

$$\text{Purity} = N^{\text{photon}}_{\text{cluster}} / N_{\text{cluster}}. \tag{4.45}$$

where $N^{\text{photon}}_{\text{cluster}}$ indicates the number of clusters generated by photons, $N^{\text{photon}}_{\text{PHOS acceptance}}$ is the number of photons within the PHOS acceptance ($|\eta| < 0.125$, $260° < \phi < 320°$), and N_{cluster} represents the number of clusters.

The "No cut" means all clusters detected by PHOS (green). The efficiency becomes $30 \sim 40\%$ above 1 GeV region. This is the maximum efficiency without any cuts for clusters. The efficiency is mostly affected by the bad cells. At this time, module 2 is removed from the analysis at all and there are several bad cells in module 1 and module 3 as shown in Figure 4.17. Consequently, the $\sim 55\%$ area can be used for the analysis. Addition to the effect, there is the photon conversion contribution. A photon with energy above 1.02 MeV can decay into an electron-positron pair within the Coulomb field of an atom. The photon conversion probability at high energy is calculated approximatly as

$$P = 1 - \exp\left(-\frac{7}{9}\frac{X}{X_0}\right). \tag{4.46}$$

where X_0 represents the radiation length [99]. The material budget map in front of the PHOS acceptance is shown in Figure 4.26 (obtained with GEANT3). The PHOS acceptance is $260° < \phi < 320°$ and $80° < \theta < 100°$ area. The acceptance area is less material budget compared to the other area because TRD and TOF detectors are not installed (have a hole) in front of PHOS to enhance the photon detection efficiency. Between interaction point and the PHOS ($0 < R < 430$ cm), there is the detector materials corresponding to about $X/X_0 \sim 0.25$. The probability of photon conversion is $P \sim 18\%$. Therefore, finally, the efficiency should be $\varepsilon_{\text{photon}} \sim 37\%$.

The "N_{cell}+Ene cut" indicates the cut of the number of cell and energy, $E_{\text{cluster}} > 0.3$ GeV and $N_{\text{cell}} > 3$. The cut reduces the efficiency up to ~ 3 GeV. In the MC simulation, the noise influence is not installed at all. Therefore, the cut is not seen to have the enormous impact
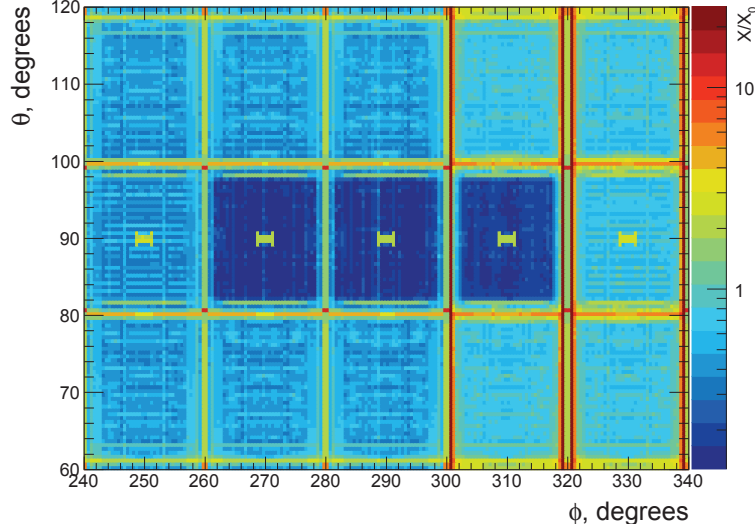
Figure 4.26: The total material budget in front of the PHOS acceptance ($0 < R < 430$ cm, $260° < \phi < 320°$ and $80° < \theta < 100°$).

on the photon selection, but, in the real data, this cut works to reduce the hardware noises without reduction of the efficiency. The "Disp cut" is the result of the dispersion cut. The efficiency is reduced by the cut, but the purity increases by 20%. The "CPV cut" is with the Charged Particle Veto cut. This cut doesn't reduce the photon efficiency, but the purity is enhanced at a whole energy region and it reaches $\sim 80\%$. The "Disp + CPV cut" is the combined result of CPV and Disp cuts. The cut reduces the efficiency same as Disp cut, but the purity gets larger dramatically and it achieves up to $\sim 95\%$.

4.3.5 Trigger Response Curve for Reconstructed Cluster

The trigger response study is very important to not only check the trigger condition, but also the analyses with the PHI data sample. It is defined as

$$\varepsilon_{\text{trigger}} = N_{\text{MB}_{\text{AND}}}^{\text{0PH0 cluster}} / N_{\text{MB}_{\text{AND}}}^{\text{All cluster}} \tag{4.47}$$

where $N_{\text{MB}_{\text{AND}}}^{\text{0PH0 cluster}}$ is the number of clusters which fired the PHOS-Trigger tile (0PH0) in MB$_{\text{AND}}$ sample and $N_{\text{MB}_{\text{AND}}}^{All \text{ cluster}}$ is the number of total clusters in MB$_{\text{AND}}$ sample. The unreliable areas are excluded from the equation at all, so it can achieve up to 100% at high energy region. These numerator and denominator are shown in Figure 4.27, the total cluster passed loose cluster selection criteria (applying the cuts of the number of cells $N_{cell} > 3$ and minimum energy $E > 0.3$ GeV) and fired trigger tile. The calculated trigger efficiency as a function of reconstructed cluster energy is shown in Figure 4.28.

4.3.6 Fake PHOS Triggered Event

Any events recorded as the PHI are fake due to electric noise and several reasons. These fake triggered events lead to make a mistake to calculate the integrated luminosity. The fake PHI event doesn't have fired trigger tiles associated with clusters. Hence, the events with firing trigger tile associated with energy cluster are regarded as "true" PHI event and if not the events are regarded as fake PHI event. The fraction of the true PHI event is studied by

$$f_{\text{true}} = N_{evt}^{\text{true PHI}} / N_{evt}^{\text{total PHI}}, \tag{4.48}$$
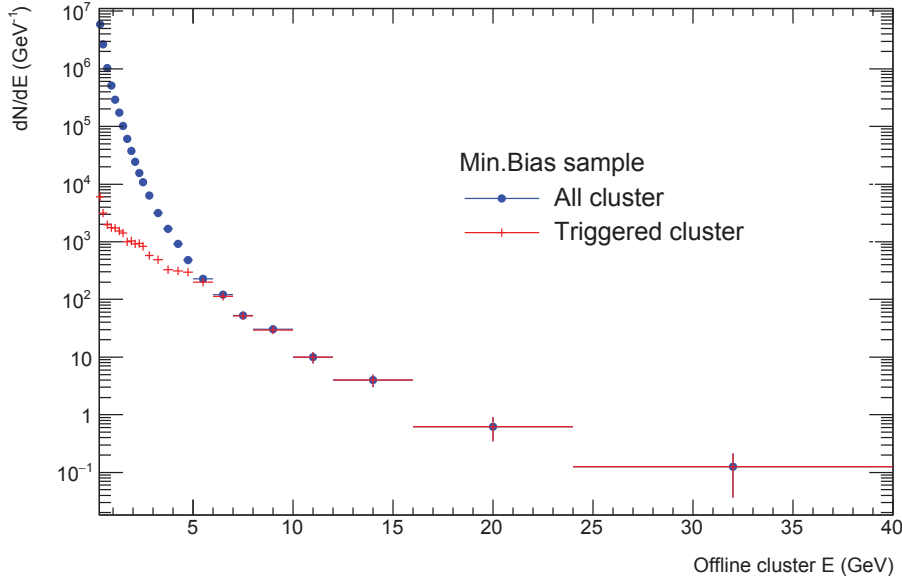
Figure 4.27: The energy distribution in the minimum-bias data sample, total (blue) and fired trigger tile (red).

where $N_{\text{evt}}^{\text{true PHI}}$ is the number of events which has at least one cluster associated with fired trigger tile and $N_{\text{evt}}^{\text{total PHI}}$ is the events labeled as PHI by the hardware level. The fraction is found to be about $f_{\text{true}} \sim 40\%$ and the fake events are removed from the analysis.

4.3.7   Rejection Factor

The rare trigger overlooks the almost all events deliberately except a specific interesting event. For example, the special interesting event for PHOS trigger is the events which have high energy photon(s). One triggered event has a value corresponding to the number of the overlooked events. The average number of the overlooked events between one interesting event and next one is called trigger rejection factor f_{RF}. The rejection factor is used to calculate the analyzed integrated luminosity. The f_{RF} is calculated with MB_{AND} data and the definition is indicated as

$$f_{\text{RF}} = N_{\text{MB}_{\text{AND}}}/N_{\text{MB}_{\text{AND}}\&\&0\text{PH0}}, \tag{4.49}$$

where $N_{\text{MB}_{\text{AND}}}$ is the number of MB_{AND} events and $N_{\text{MB}_{\text{AND}}\&\&0\text{PH0}}$ is the number of MB_{AND} events which has at least one cluster fired trigger tile. It is found to be $(12.4 \pm 1.5) \times 10^3$.

The value strongly depends on the method to select the PHI event as well as the detector condition. In the bad detector condition, the probability of the firing trigger is less than the good condition. The demoninator in Equation 4.49 is varied by the PHI event selection criteria. When the tight criteria are applied to the event selection, the f_{RF} becomes larger than the loose event selection. However, for the integrated luminosity calculation, the dependence of the method to select event is cancelled out. The integrated luminosity is calculated by

$$\int \mathscr{L}\mathrm{d}t = N_{\text{PHI}} * f_{\text{RF}}/\sigma_{\text{MB}_{\text{AND}}} \tag{4.50}$$

here N_{PHI} is the number of analyzed PHI events and $\sigma_{\text{MB}_{\text{AND}}}$ is the cross-section of the minimum-bias trigger. In the formula, the effect of PHI event selection is included in the
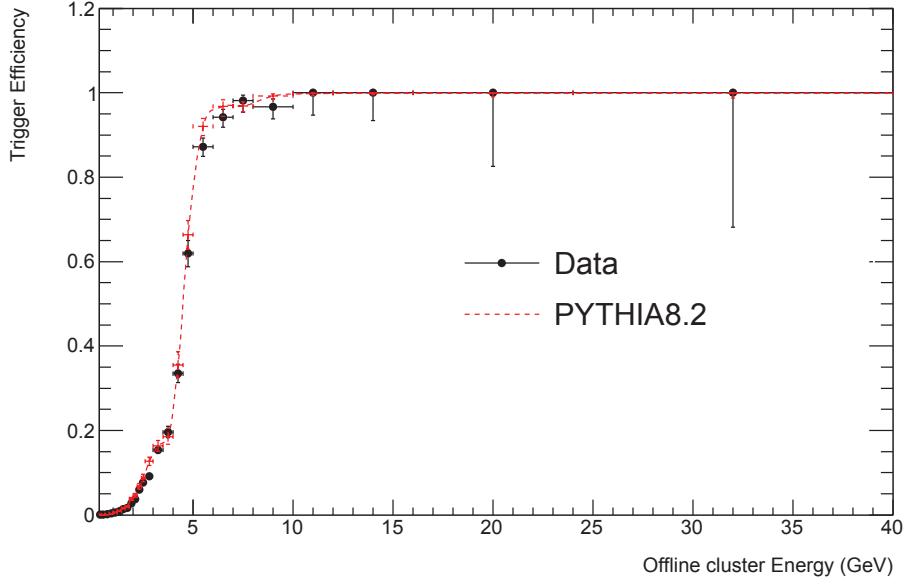
Figure 4.28: The calculated trigger efficiency as a function of reconstructed cluster energy.

numerator of N_{PHI} and in the denominator of f_{RF}. Therefore, eventually, for the integrated luminosity, the effect is removed.

4.4 Neutral Pion Reconstruction

In this section, the method to reconstruct neutral mesons from a photon pair detected by the PHOS will be explained. The loose cluster selection criteria with the cuts of the number of cells $N_{cell} > 3$ and minimum energy $E > 0.3$ GeV are used because the background can be negligible in proton+proton collisions.

4.4.1 Invariant Mass of Photon Pair

Almost all π^0 ($\sim 98\%$) decays into two photons ($\pi^0 \rightarrow \gamma\gamma$). The π^0 is reconstructed with the invariant mass method in this analysis. The invariant mass of two photons is determined as

$$M_{12} \quad = \quad \sqrt{2E_1 E_2 \big(1 - \cos\theta_{12}\big)} \tag{4.51}$$

where E_1 and E_2 are the energy of two photons measured by the PHOS and θ_{12} is the opening angle between the photons. The opening angle θ_{12} is calculated by

$$\cos\theta_{12} = \frac{(\mathbf{r}_1 - \mathbf{V}) \cdot (\mathbf{r}_2 - \mathbf{V})}{|\mathbf{r}_1 - \mathbf{V}||\mathbf{r}_2 - \mathbf{V}|} \tag{4.52}$$

where the vector $\mathbf{r}_1$ and $\mathbf{r}_2$ detected positions of two photons on the PHOS surface estimated by the Equation 4.39 and the vector $\mathbf{V}$ is the primary collision vertex position measured by the SPD. The original position of photons cannot be measured by the ALICE because the photon tracking detector is not installed. Therefore, the photon candidates are assumed that they come from the primary collision vertex. Simultaneously, the momentum of two photons is calculated by

$$\mathbf{p}_{12} = E_1 \cdot \frac{\mathbf{r}_1 - \mathbf{V}}{|\mathbf{r}_1 - \mathbf{V}|} + E_2 \cdot \frac{\mathbf{r}_2 - \mathbf{V}}{|\mathbf{r}_2 - \mathbf{V}|}. \tag{4.53}$$
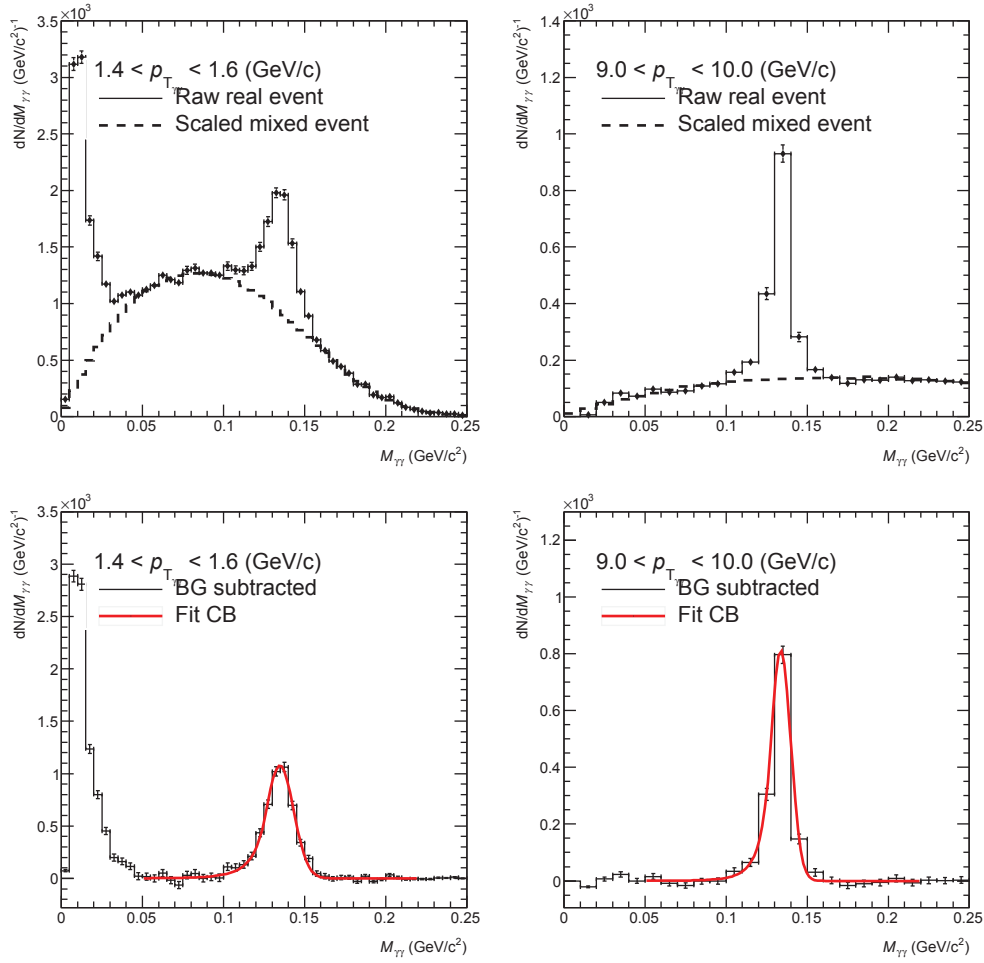
Figure 4.29: Invariant mass distribution in same event (top solid line) and scaled mixed event (top dashed line. Neutral pion signal (black solid line)) and the fitted result with the peak function (red solid line).

The whole combination pair of detected clusters are calculated. When the multiplicity of the cluster in an event is N, the number of combination is $N(N-1)/2$. The combinations of true photon pair contributes to true invariant mass region, $(M_{\pi^0} : 135 \mathrm{MeV}/c^2)$. On the other hand, the wrong combination pair contributes not only true invariant mass region but also all mass region affected by the detector acceptance limitation. The calculated invariant mass distributions given transverse momentum bins are shown in top panels in Figure 4.29 (solid line).

4.4.2 Combinatorial Background

Limited acceptance of the PHOS results in the complicated shape of the combinatorial background around the neutral pion peak. The combinatorial background is divided into correlated and un-correlated groups. The origin of correlated backgrounds may be jet, resonance particle decay, radial flow and so on. The other one is cluster pair which doesn't have any correlations between them. The acceptance effect influences in the same manner the correlated and

un-correlated backgrounds. To account this, the procedure with fitting the ratio of real (same event) and mixed (mixed event) around the peak region with polynomial functions. In this way, the background can be described with simpler functions and incorporate acceptance effects. Then, the mixed distribution scaled with the polynomial is subtracted from the real one and the signal distribution is produced. The procedure to estimate the combinatorial background for the PHOS is summarized as following,

I. Choose two different event A and B which have similar event classified with primary collision vertex and the number of SPD tracklets.

II. Calculate the invariant mass from cluster pairs which are one photon is from event A and one is from event B.

III. Repeat above procedures and accumulate statistics.

IV. Divide the real mass spectrum by the mixed event mass spectrum and fit the ratio with a sum of peak function and second-order polynomial function (the peak function is explained in Section 4.6.1).

V. Scale the mixed event mass spectrum with the second-order polynomial function part obtained by the previous step.

The produced background of two different transverse momenta reneges are plotted in the top panel of Figure 4.29 as the dashed line. At the high transverse momentum plot (right panel), the combinatorial background is reproduced well. On the other hand, at low transverse momentum region (left panel), the peak at very low mass region cannot be reproduced well. This is due to the combination of charged particle clusters from one source, e.g. resonance particle decays $\omega \to \pi^0\pi^+\pi^-$, $K_s^0 \to \pi^+\pi^-$ and so on. These charged particles deposit their energy as MIP (few hundred MeV), so the contributions are only low momentum region.

The background subtracted invariant mass spectra are shown in bottom panels of Figure 4.29 as the black marker. The spectrum of the side of the mass peak is flat. This indicates that the background is subtracted correctly.

4.4.3 Signal Yield Extraction

Naturally, the mass peak shape should be symmetry. However, measured peak shape has a tail at the low mass region. Photons create EM shower and deposits about 80% of their energy in one $PbWO_4$ crystal. The remnant energy leaking the adjacent non-active cells are not counted to calculate the cluster energy. Therefore, the peak has a tail at low mass side. In addition to the above effect, when the photon converts into e^+e^- pair in the material between the TPC and PHOS detector with losing their energy due to Bremsstrahlung, the mass calculated with these clusters is smaller than the real mass. To take into account the low mass tail, the peak function with asymmetry tail at the lower mass region is used. The Crystal Ball (CB) function [64] is adopted. The function is a sum of Gaussian and a power-law tail at higher mass region and lower mass region, respectively, as described in Equation 4.54.

$$f(x, \mu, \sigma, \alpha, n) = N \cdot \begin{cases} \exp\left(-\frac{(x-\mu)^2}{2\sigma^2}\right) & \frac{x-\mu}{\sigma} > -\alpha \\[3mm] A\left(B - \frac{x-\mu}{\sigma}\right)^{-n} & \frac{x-\mu}{\sigma} \leq -\alpha \end{cases} \tag{4.54}$$

where

$$A = \left(\frac{n}{|\alpha|}\right)^n \exp\left(\frac{-|\alpha|^2}{2}\right)$$
$$B = \frac{n}{|\alpha|} - |\alpha|.$$

After subtraction of the scaled mixed event from the real invariant mass spectrum is fitted by above CB function within mass range of $0.08 \leq M_{\gamma\gamma} \leq 0.22$. The fitted results are shown in the bottom panel of Figure 4.29 as red lines.

The number of reconstructed neutral pion is counted by a bin-counting method with the $-5 < \sigma < 3$ window size, where σ is the width parameter of the Gaussian part in CB. The reason of the asymmetry window is to consider the asymmetry peak shape. The number of the reconstructed neutral pion as a function of the reconstructed transverse momentum of two trigger analysis are shown in Figure 4.30. These plots are normalized by the number of analyzed events in consideration of the rejection factor explained in Section 4.3.7 for PHI analysis.
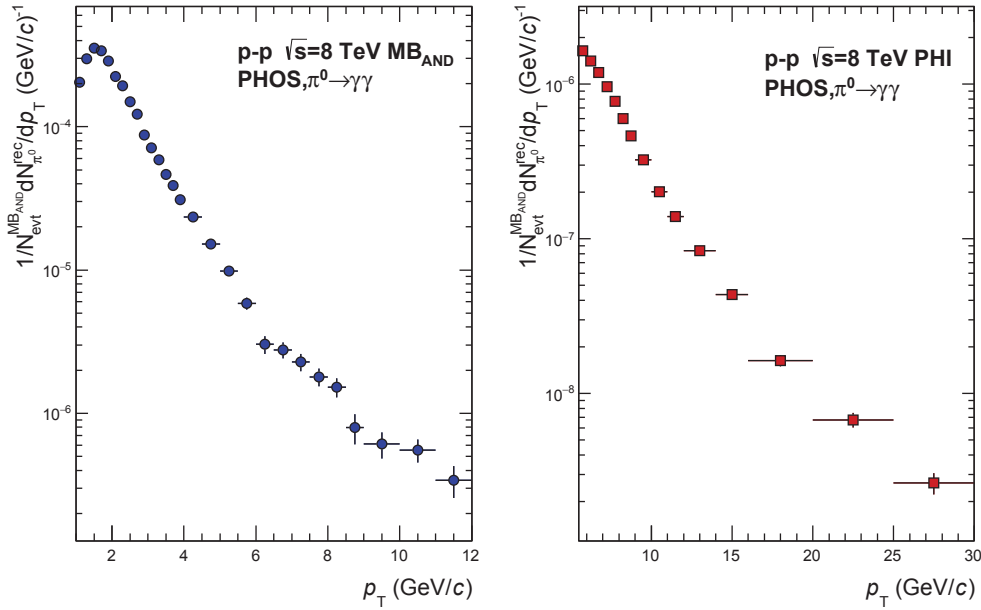
Figure 4.30: The number of reconstructed neutral pion spectrum scaled by analyzed events of MB$_{\mathrm{AND}}$ and PHI.

The mass peak position and width are plotted in Figure 4.33. The peak position above 1.5 GeVc is consistent with the true mass value within 1%, but at low transverse momentum region, the peak position decreases due to the non-linearity effect. The high energy resolution of $\delta E \sim 4\%$ is achieved, so the peak width is 6 MeV/c^2 above transverse momentum of 2 GeV/c.

4.5   Efficiency Corrections

In this section, several efficiencies used to calculate the invariant cross-section with the number of reconstructed neutral pion extracted in the previous section are explained. Most of the efficiencies will be estimated by Monte-Carlo (MC) simulation with realistic event generator and detector response simulator.

4.5.1   Event Generator

In this analysis, Pythia 8 [100] with minimum-bias and jet processes are used. Pythia 8 simulates the subsequent steps, such as initial- and final state parton showers, multiple parton-
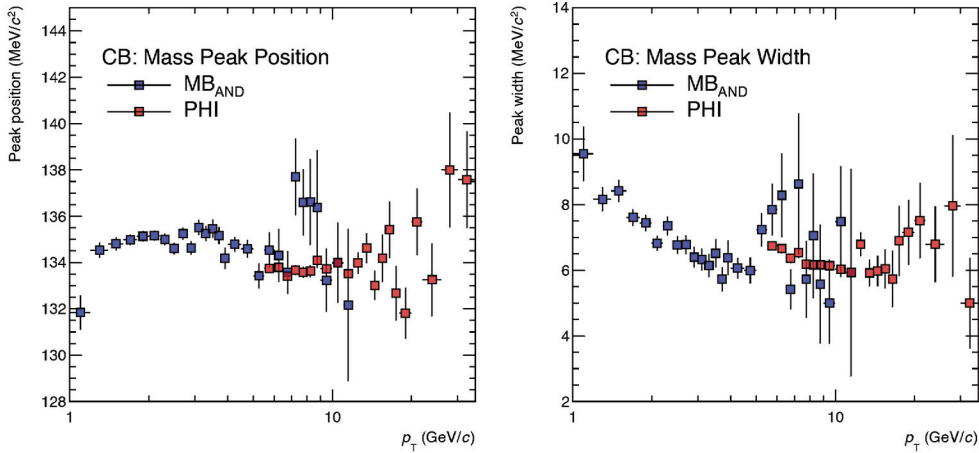
Figure 4.31: The peak position and width as a function of transverse momentum.

parton interaction, string fragmentation and decay. In addition to these processes, the diffractive processes based on Regge theory [66] are also implemented. The initial state in nuclear is described with the parton distribution functions (PDFs) models, e.g CTEQ5L [69], MSTWpdf [25], CTEQ6pdf [69] and so on. The hard scattering is optimized for leading order processes, $2 \rightarrow 1$ and $2 \rightarrow 2$ processes. The hadronization is computed with the LUND String Model [67]. The decay properties of all hadrons are stored in decay tables and are decayed accordingly [68]. As Pythia combines a lot of different processes, it has many tunable parameters with significant influence on the generated distributions, reflected especially in the low momentum transfer processes. One of these parameters is the connection between low and high momentum processes, which is given by a minimum momentum transfer of 2 GeV/c.

Cut-offs on the momentum transfer ($p_{\mathrm{T,cut-off}}$) can be optimized to select events. This allows to generate samples with larger statistics for higher transverse momenta without adding particles arbitrarily and instead of following the original compositions and energy distributions. However, those productions need to be weighted in order to correctly describe the spectrum and should not be used below a certain threshold in momentum. The weight value can be calculated as

$$w_{\mathrm{JetJet}}^{\mathrm{MB}} = \frac{\sigma_{\mathrm{JJ}}^{p_{\mathrm{T,cut-off}}}}{N_{\mathrm{JJ,trial}}^{p_{\mathrm{T,cut-off}}}} \cdot \frac{1}{N_{\mathrm{JJ,gen}}^{p_{\mathrm{T,cut-off}}}} \tag{4.55}$$

where $\sigma_{\mathrm{JJ}}^{p_{\mathrm{T,cut-off}}}$ is the cross section of the hard process with the momentum transfer above $p_{\mathrm{T,cut-off}}$, $N_{\mathrm{JJ,trial}}^{p_{\mathrm{T,cut-off}}}$ is the number of minimum-bias process to find event with the momentum transfer above $p_{\mathrm{T,cut-off}}$ (the number of trial), and $N_{\mathrm{JJ,gen}}^{p_{\mathrm{T,cut-off}}}$ is the number of process with the momentum transfer above $p_{\mathrm{T,cut-off}}$.

In this analysis, 20 cut-off bins are used to enhance the high transverse momentum statistics. Each cut-off bin range and weight is summarized in Table 4.3. The number of generated neutral pion in a unit rapidity ($|y| < 0.5$) of each cut-off transverse momentum bin w/ (right) and w/o (left) weight in are described in Figure 4.32.

4.5.2 Realistic Detector Response in MC

Detector response is simulated by using GEANT3 [71] with ALICE offline framework [72]. The response is tuned with the neutral pion mass peak position and width for energy calibration and de-calibration. The mass peak and width of MB$_{\mathrm{AND}}$ and PHI are combined with the method

Bin#	min $p_{\text{T,cut-off}}$ (GeV/c)	max $p_{\text{T,cut-off}}$ (GeV/c)	$w_{\text{JetJet}}^{\text{MB}}$
1	5	7	28.3084
2	7	9	8.43644
3	9	12	4.08152
4	12	16	1.54488
5	16	21	0.543354
6	21	28	0.208337
7	28	36	0.0652981
8	36	45	0.018692
9	45	57	0.0083484
10	57	70	0.00301511
11	70	85	0.00125962
12	85	99	0.000474334
13	99	115	0.000244081
14	115	132	0.000119326
15	132	150	6.09949e-05
16	150	169	3.24288e-05
17	169	190	1.84495e-05
18	190	212	1.00916e-05
19	212	235	5.69035e-06
20	235	inf	8.38186e-06

Table 4.3: The summary table of each transverse momentum cut-off range [70].

considering the correlation between then as explained in Section 4.6.9. The reconstructed neutral pion mass peak position and width are compared as a function of transverse momentum between data and MC to confirm a proper detector response in the simulation. The comparisons are shown in Figure 4.33.

4.5.3 Acceptance $\times$ Reconstruction Efficiency

The number of reconstructed π^0 is limited by detector geometrical acceptance. The PHOS detector is covering in azimuthal angle $260° < \phi < 320°$ ($\Delta\phi = 60°$) and in rapidity range of $-0.12 < \eta < 0.12$ ($\Delta\eta = 0.24$) in 2012 runs. The particle production induced by proton+proton collisions doesn't depend on the azimuthal angle and the rapidity distribution at the mid-rapidity region.

The opening angle between two photons in lab frame depends on the momentum of parent neutral pion. The probability that both two photons are detected by the PHOS decreases with lower transverse momentum because the opening angle is larger than the detector acceptance. The acceptance correction factor Acc is calculated with following equation.

$$Acc = N_{\pi^0}^{\text{Acceptance}} / N_{\pi^0}^{\text{Generated } |y|<0.5} \tag{4.56}$$

where $N_{\pi^0}^{\text{Acceptance}}$ is the number of neutral pion of which two photons going to the PHOS acceptance and $N_{\pi^0}^{\text{Generated } |y|<0.5}$ is the number of neutral pion in an unit pseudo-rapidity. The acceptance Acc as a function of reconstructed transverse momentum is shown in Figure 4.34 (left panel).

The whole photons coming to the PHOS acceptance cannot be detected because there are some effects to vanish the photons. One is the external conversion in materials. About 8% photons are vanished by the effect in front of the PHOS. Besides, two clusters on the PHOS surface are expected to start merging from around 25 GeV/c because the distance between
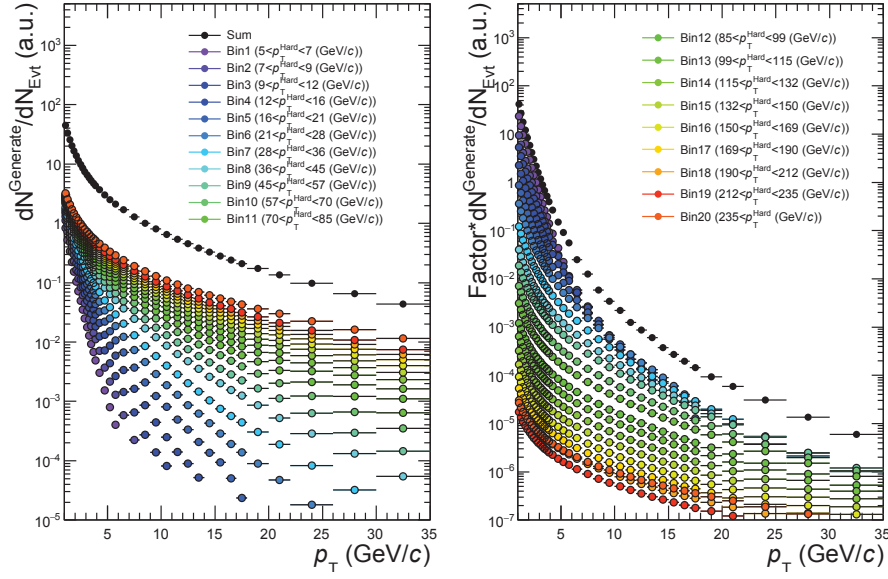
Figure 4.32: The number of neutral pion generated by Pythia 8 with cut-off bin in a unit rapidity.
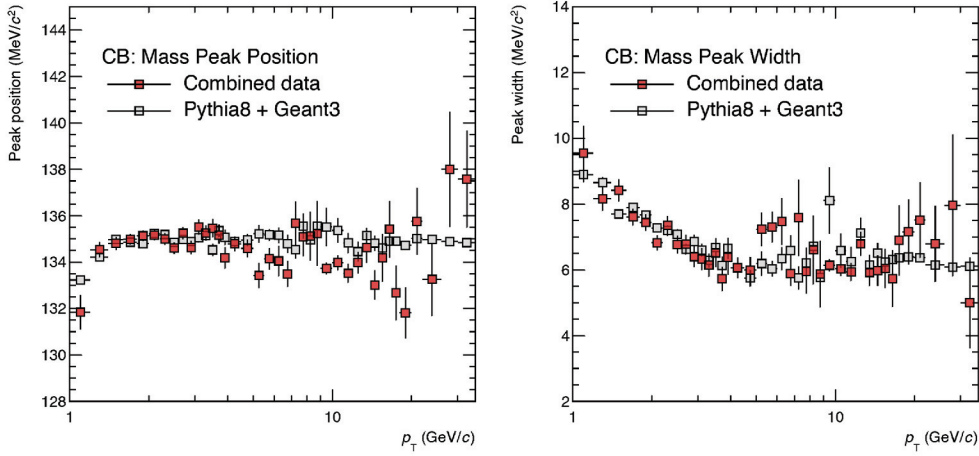
Figure 4.33: Reconstructed neutral pion peak position and width in data and MC simulation as a function of transverse momentum.

two clusters becomes smaller than one cell size (2.2×2.2 cm^2) due to small opening angle. Furthermore, there are several effects to reduce the reconstruction efficiency. To take any effects into account, the reconstruction efficiency $\varepsilon_{\rm rec}$ is defined as

$$\varepsilon_{\rm rec} = N_{\pi^0}^{\rm Rec} / N_{\pi^0}^{\rm Acceptance} \tag{4.57}$$

where $N_{\pi^0}^{\rm Rec}$ is the number of reconstructed neutral pion with the method explained in Section 4.6.1 and $N_{\pi^0}^{\rm Acceptance}$ is the number of neutral pion same as in the Equation 4.56. As expected, the reconstruction efficiency $\varepsilon_{\rm rec}$ decreases from around 25 GeV/c due to the cluster merging. Up to 50 GeV/c π^0s can be reconstructed by using the invariant mass method.
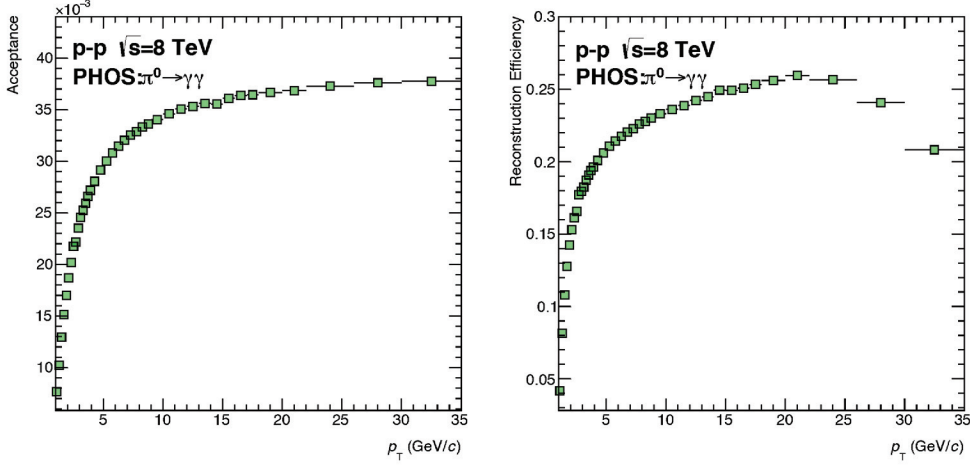
Figure 4.34: The acceptance and reconstruction efficiency as a function of transverse momentum in a given period.

With combining Equation 4.56 and Equation 4.57, the acceptance×reconstructed efficiency, $Acc \times \varepsilon_{\mathrm{rec}}$, can be calculated as following

$$Acc \times \varepsilon_{\mathrm{rec}} = N_{\pi^0}^{\mathrm{Rec}} / N_{\pi^0}^{\mathrm{Generated}\ |\eta|<0.5}. \tag{4.58}$$

The acceptance and the reconstruction efficiency are varied with a given period. To consider the difference of the $Acc \times \varepsilon_{\mathrm{rec}}$ and the number of analyzed events within a given period, the $Acc \times \varepsilon_{\mathrm{rec}}$ is combined with a following weighted method.

$$X = \sum_{i=0}^{\mathrm{nPeriod}} N_{\mathrm{evt}}^i X_i / \sum_{i=0}^{\mathrm{nPeriod}} N_{\mathrm{evt}}^i \tag{4.59}$$

where N_{evt}^i and X_i are the number of analyzed events and a variable to be combined in a given period i, respectively. The combined results of $Acc \times \varepsilon_{\mathrm{rec}}$ as a function of the reconstructed transverse momentum of $\mathrm{MB_{AND}}$ and PHI are shown in Figure 4.35. The difference between $\mathrm{MB_{AND}}$ and PHI comes from the number of analyzed events in a given time interval.

4.5.4 Trigger Efficiency for Reconstructed Neutral Pion

The trigger efficiency as a function of reconstructed neutral pion transverse momentum, $\varepsilon_{\mathrm{trig}}$, is defined as

$$\varepsilon_{\mathrm{trig}}^{\pi^0} = N_{\pi^0}^{\mathrm{Rec\&\&0PH0}} / N_{\pi^0}^{\mathrm{Rec}} \tag{4.60}$$

where $N_{\pi^0}^{\mathrm{Rec\&\&0PH0}}$ is the number of reconstructed neutral pion from which at least one photon fires the trigger tile, and $N_{\pi^0}^{\mathrm{Rec}}$ is the number of total reconstructed neutral pion. The result is shown in Figure 4.36.

The trigger efficiency as a function of reconstructed cluster energy $\varepsilon_{\mathrm{trigger}}$ in Section 4.3.5 achieves unity at high energy region. In spite of this, the highest trigger efficiency for π^0 is around 0.7 due to active TRUs. The bad TRUs are masked for both energy detection and firing the trigger tile in $\varepsilon_{\mathrm{trigger}}$. Therefore, the $\varepsilon_{\mathrm{trigger}}$ is calculated with good TRUs and achieves unity. On the other hand, in the efficiency, those bad TRU areas are not masked for energy detection, but they are masked for firing the trigger tile to enhance the statistics. There are following three scenarios when neutral pions are reconstructed.
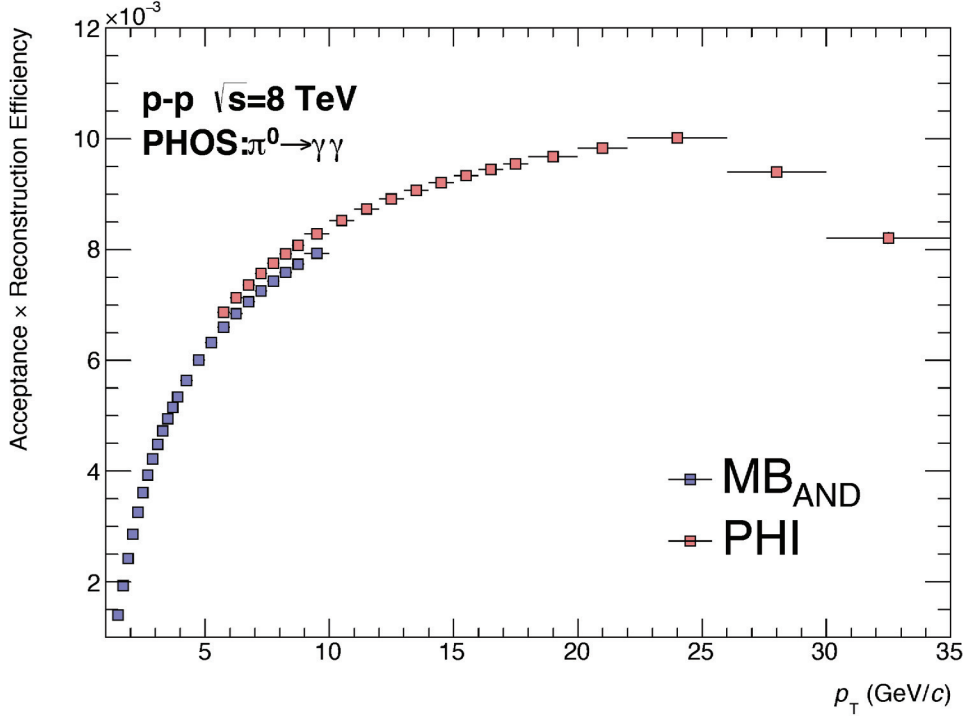
Figure 4.35: The acceptance times reconstruction efficiency for MB$_\text{AND}$ and PHI. The difference comes from the number of analyzed event in a given period.

1. One photon fires trigger tile and the other one doesn't fire the trigger tile.

2. Both photons don't fire the trigger tile.

3. Both photons fire the trigger tile.

The denominator in Equation 4.60 is the sum of scenario (1)+(2)+(3) and the numerator is the sum of scenario (1)+(3). This is the reason that the trigger efficiency as a function of reconstructed neutral pion does not reach the 100% efficiency at high transverse momentum.

4.5.5 Cluster Timing Cut Efficiency

Bunch crossing space is 50 ns in 2012 proton+proton program. The PHOS data taking window size is 6 μs, thus multiple bunch crossings can be seen during one event recording. The probability of multiple collisions during one event data taking is about 20% for $\mu \sim 0.04$. Therefore, a cut for cluster detection timing is applied to reject clusters which come from the other bunches. These clusters from not current triggered bunch crossing are called the outer-bunch pile-up cluster. The value of the timing cut is $|Timing| <25$ ns.

The contributions not from the current bunch crossing are removed with above timing cut. However, some clusters from a current bunches also rejected by the timing cut due to the timing resolution. Therefore, this cut efficiency has to be considered and correct the spectrum. The efficiency can be calculated by applying the cut to both clusters and at least one cluster which is used to reconstruct neutral pion.

$$N_\text{true} = N^{\pi^0}_\text{at least one cluster}/\left(1 - (1 - \varepsilon_\text{timing}) \times (1 - \varepsilon_\text{timing})\right) \qquad (4.61)$$

$$N_\text{true} = N^{\pi^0}_\text{both cluster}/\varepsilon_\text{timing} \times \varepsilon_\text{timing} \qquad (4.62)$$
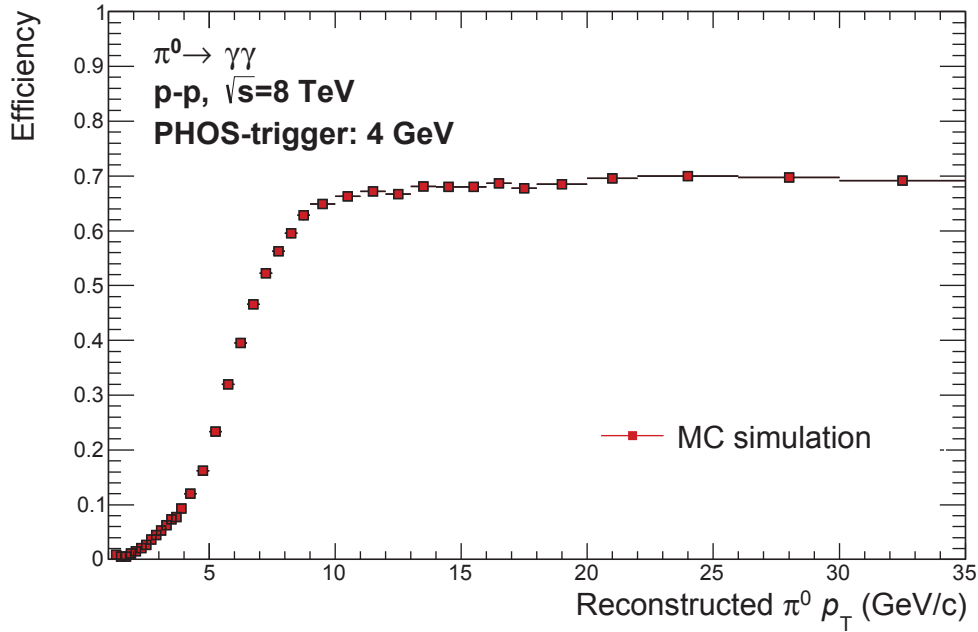
Figure 4.36: Trigger efficiency as a function of reconstructed neutral pion transverse momentum.
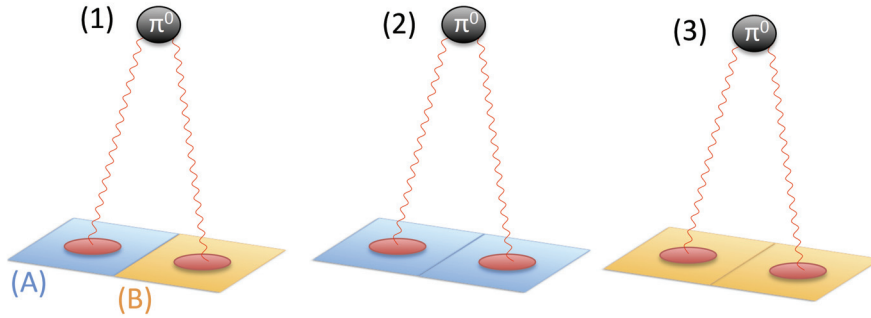
Figure 4.37: The orange tile (A) means that TRU is active and it can measure the photon energy and the blue (B) means that TRU is not active but it can measure energy in this figure. We can imagine three ways to detect two photons from a π^0: (1) One photon is detected by (A) tile and the other photon is detected by (B) tile. (2) Both photons are detected by (B) tile. (3) Both photons are detected by (A) tile. The trigger efficiency as a function of reconstruction efficiency (Figure 4.28) is the efficiency of only orange tile (not including blue tile). The denominator and the numerator in eq.4.60 are (1)+(2)+(3) and (1)+(3), respectively. Therefore, if the trigger efficiency for a cluster is 100%, the maximum efficiency can not reach 100%.
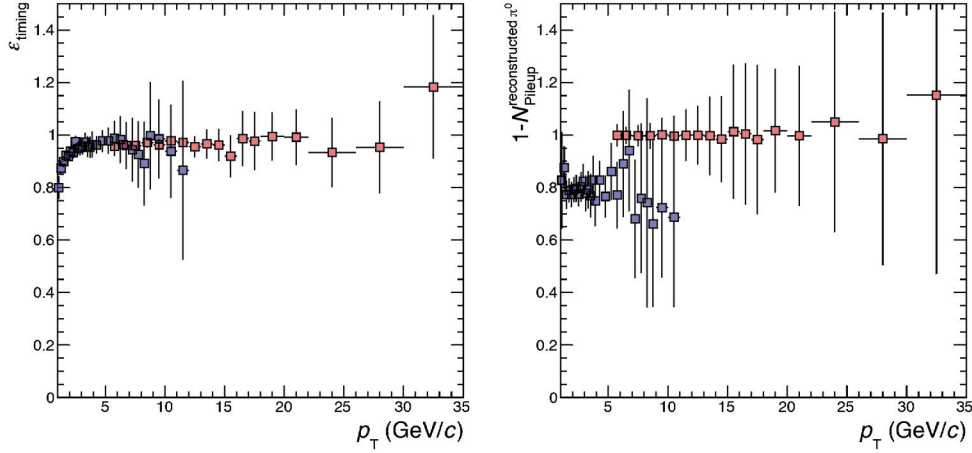
Figure 4.38: The timing cut efficiency for reconstructed neutral pion (left). The pile-up contribution in MB_{AND} and PHI (right).

where N_{true} is the number of reconstructed neutral pion from the current bunch crossing, $N^{\pi^0}_{\text{at least one cluster}}$ is the number of reconstructed neutral pion with at least one cluster passed the timing cut, $N^{\pi^0}_{\text{both cluster}}$ is the number of reconstructed neutral pion with both clusters passed timing cut and $\varepsilon_{\text{timing}}$ is the timing cut efficiency. The timing cut efficiency $\varepsilon_{\text{timing}}$ can be evaluated by solving above equations.

$$\varepsilon_{\text{timing}} = 2N^{\pi^0}_{\text{both cluster}}/(N^{\pi^0}_{\text{both cluster}} + N^{\pi^0}_{\text{at least one cluster}}) \tag{4.63}$$

The calculated results of $\varepsilon_{\text{timing}}$ and the outer-bunch pileup contribution of each trigger sample is shown in Figure 4.38 (left and right panel respectively). The timing cut efficiency decreases at low transverse momentum region because timing resolution of the PHOS is poor, but at high transverse momentum region, the efficiency is near the unity due to excellent timing resolution. In MB_{AND} case, the pile-up contribution is about 20% and doesn't have transverse momentum dependence. On the other hand, in the PHI case, there is no pile-up contribution. The probability of the PHI event is $\mu_{\text{PHI}} = \mu_{MB_{AND}}/f_{\text{RF}} \sim \times 10^{-6}$, so it is hard to happen the PHI evens several times together.

4.5.6 Secondary Neutral Pion Contribution

In order to measure the primary neutral pion yield, the secondary (off-vertex) neutral pion, from the weak decays and/or hadronic interactions in the detector material should be excluded. These contributions are estimated by using the MC simulation which is used to estimate several efficiencies.

The main source of off-vertex production from weak decay is $K_s^0 \rightarrow \pi^0\pi^0$ with a branching ratio of 30.69% and mean life time of about 0.89×10^{-10}s ($c\tau = 2.7$cm). The contribution from K_s^0 is displayed in Figure 4.39 (orange). The contribution decreases with including its transverse momentum. The lifetime of the K_s^0 gets longer with higher momentum due to relativity. All photons cannot be tracked and so their momentum is calculated by assuming that they come from the primary vertex. When the neutral pion comes from not the near primary vertex, the calculated mass position becomes smaller than expected and never counted. The deviation of the calculated mass is proportional to the flight distance, so the contribution from K_s^0 becomes smaller with higher transverse momentum. The other contributions of weak decays, Λ and K_L^0
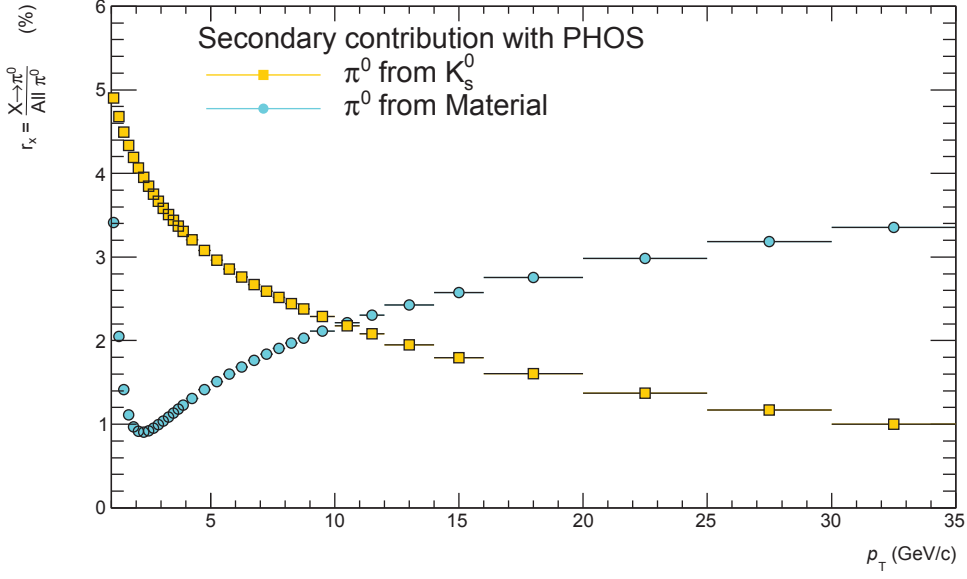
Figure 4.39: The fraction of secondary contributions from the feed-down and materials.

can be expected, but these contributions can be negligible because both contributions are less than 0.1% for all transverse momentum range.

While the contribution from material interaction shown in Figure 4.39 (light blue) becomes larger with increasing transverse momentum because the interaction probability between any particle coming from the collision and material becomes larger. The high transverse momentum neutral pion induced by the material interaction is punched out by high momentum particles. Therefore, the contribution becomes larger.

4.5.7 Bin-shift Correction

There is difference induced by the finite bin width between true and data points. It can be corrected by moving the points along the x-axis with bin-shift correction. The bin-shift correction for the x-axis is carried out as following with spectrum shape assumption function $f(x)$. The weight of the bin m is extracted with following.

$$m = \int_{p_\mathrm{T}^\mathrm{min}}^{p_\mathrm{T}^\mathrm{max}} p_\mathrm{T} f(p_\mathrm{T}) dp_\mathrm{T} / \int_{p_\mathrm{T}^\mathrm{min}}^{p_\mathrm{T}^\mathrm{max}} f(p_\mathrm{T}) dp_\mathrm{T} \tag{4.64}$$

where p_T^max and p_T^min are minimum ana maximum p_T of the bin. Then, following ratio of m to the center of the bin, p_T^cent, is calculated.

$$r = m/p_T^\mathrm{cent} \tag{4.65}$$

In this formula, p_T^cent is a center position of the bin. The r is correction factor for each point and it moves along the x-axis.

$$p_\mathrm{T}^\mathrm{corr} = p_\mathrm{T}^\mathrm{before} \times r \tag{4.66}$$

These procedures are repeated (iteration) until all points are stable.

4.6 Systematic Uncertainties

Following systematic uncertainties are considered in this analysis.

4.6.1 Signal Yield Extraction

Basically, a sum of the crystal ball function and 2nd order polynomial function is used to fit the peak. To estimate the signal yield extraction systematic uncertainty, the peak and polynomial functions are varied to fit the peak. The peak function should have a low mass tail like the CB. Therefore, the following function is employed,

$$f(x; M_{\pi^0}, \lambda) \quad = \quad A\left(G(x) + \exp\left(\frac{x - M_{\pi^0}}{\lambda}\right)\left(1 - G(x)\right)\Theta(M_{\pi^0} - x)\right), \qquad (4.67)$$

$$G(x) \quad = \quad \exp\left(-\frac{(x - M_{\pi^0})^2}{2\sigma_x^2}\right) \qquad (4.68)$$

where M_{π^0} is true π^0 mass, λ and σ_x are fit free parameters and Θ is a step function. This function is the combination of the exponential tail and Gaussian part at lower and higher mass region than the peak position, respectively. The fit is performed with several combinations of the peak and the polynomial functions. The $RMS/Mean$ is used for calculation of the systematic uncertainty induced by the signal yield extraction.

4.6.2 Non-linearity for energy response

Following simple non-linearity model is applied to correct measured cluster energy in MC simulation.

$$E_{\text{corr}} \quad = \quad E \cdot f(E), \qquad (4.69)$$

$$f(E) \quad = \quad c \cdot (1 + \frac{a}{1 + E^2/b^2}) \qquad (4.70)$$

where E and E_{corr} are before and after re-tuning the cluster energy, respectively. The free parameters in this equation are a and b. These two parameters are changed and compared the peak position of real data and MC simulation. Then, χ^2/ndf is calculated to find best parameters. The uncertainties of the parameters are defined by using $\delta\chi^2/\text{ndf}=1$ points.

4.6.3 Acceptance (Bad maps)

The γ deposits about 80% their energy in the injected cell. However, remaining 20% energy leaks outside of the cell. To study this effect, we analyzed the spectra with two type acceptances, only bad maps, and bad maps + fiducial cut analysis. The fiducial cut means clusters on edge of the module and adjacent to bad cells are rejected. Each full corrected spectrum is compared and the systematic uncertainty is calculated with the $RMS/Mean$.

4.6.4 Cluster timing cut efficiency

Normally, $|Timing| < 25$ ns is used to reject neutral pion which comes from not current bunch crossings. The cut efficiency can be evaluated by the method explained in Section 4.5.5. To estimate the systematic uncertainty of the cut, other cut values $|timing| < 5, 10, 15, 20$ ns are also used. The systematic uncertainty related to the cut is estimated by comparing each full corrected spectrum.

4.6.5   Trigger efficiency

To estimate uncertainty related to the trigger efficiency, three type trigger efficiency for a reconstructed cluster energy, (1)MC point,(2)real data point and (3)fitted results are used to estimate the systematic uncertainty. The fit function for the trigger efficiency is a combination of three Fermi functions as follows.

$$\varepsilon_{\text{trigger}}(E_{\text{cluster}}) \quad = \quad F_{\text{transition}} \times F_{\text{low}} + (1 - F_{\text{transition}}) \times F_{\text{high}} \tag{4.71}$$

$$F(x) \quad = \quad \frac{p_0}{\exp(x - p_1)/p_2 + 1} \tag{4.72}$$

The deviation is larger at low transverse momentum region due to the turn on curve is very steep. The uncertainty of the efficiency is $RMS/mean$ value of these three types.

4.6.6   Normalization factor

The standard method to calculate the rejection factor uses the total analyzed events explained in Section 4.3.7. The rejection factor of each given period is calculated and used to estimate the systematic uncertainty related to the rejection factor.

4.6.7   Global energy scaling

The absolute energy scale is estimated by comparing the mass peak of MC and data. The difference between MC and data is 0.1%. The final full spectrum is affected by the difference via efficiency corrections. The effect is quantified by the following equation,

$$\delta f(p_{\text{T}}) = f(p_{\text{T}} * (1 + \delta p_{\text{T}}))/f(p_{\text{T}}) \tag{4.73}$$

where $f(x)$ is the fit function reproducing the final spectrum and the Tsalis-Levy function [73] is employed, δp_{T} is transverse momentum deviation described as $\delta p_{\text{T}} = 1.001 * p_{\text{T}}$. This has the great effect on the spectrum at low transverse momentum region because the spectrum is steeper than higher transverse momentum region.

4.6.8   Other sources

The material budget in front of the PHOS, especially between TPC and PHOS cannot be measured well because inside of the TPC the material budget can be measured by using the photon conversion method (PCM), but outside of the TPC, the electron-positron pairs from photon conversion cannot be reconstructed. To estimate the material budget between the outside of the TPC, the L3 solenoid magnet off special runs are carried out. During runs with the L3 magnet on, an electron-positron pair from photon conversion is curved toward opposite side each other and their clusters on the PHOS is separated. On the other hand, without the L3 magnet, the conversion electron/positron creates one cluster on the PHOS because the pair is not bent. The systematic uncertainty related to the material budget (conversion) can be estimated by comparing the difference of the number of clusters in magnet on and off between data and MC. The material budget is same as the previously published paper [74] and the same value is used in this analysis.

4.6.9   Total systematic uncertainty

The systematic uncertainties sources of each triggered sample as a function of transverse momentum are shown in Figure 4.40. In the figures, the constant systematic uncertainties are put together and named "Total Constant Syst.Uncert.". In case of the MB_{AND} analysis, the conversion, acceptance, timing cut and event generator are grouped as the constant uncertainty

and the total constant systematic uncertainty is found to be 7.1%. In addition to above uncertainty sources, in the PHI analysis, the systematic uncertainty related to normalization factor is also added to the constant source uncertainty and it is found to be 9.2%. At low transverse momentum region, the main sources are the signal yield extraction and reconstructed efficiency in MB_{AND} analysis. In PHI analysis, the largest uncertainty is the normalization factor.
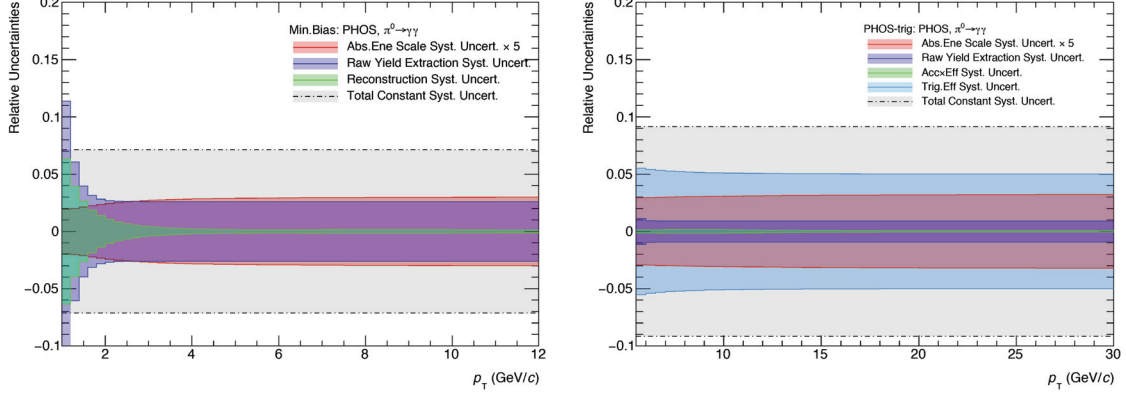
Figure 4.40: The total systematic errors in MB_{AND} (left) and the total systematic errors in PHI (right).

The quadratic sum of the uncertainties is the total systematic uncertainty. The total systematic and statistical uncertainty of MB_{AND} and PHI are shown in Figure 4.41.
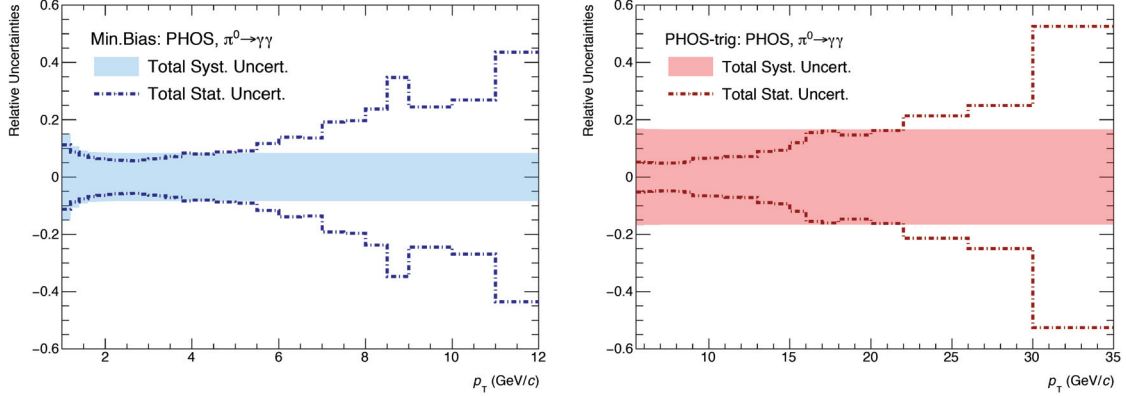
Figure 4.41: The total statistics and systematic uncertainties in MB_{AND} (left) and the total statistics and systematic uncertainties in PHI (right).

When combining MB_{AND} and PHI analyses, the correlated and un-correlated systematic uncertainties are considered. The method to combine spectra which are same physical quantities measured by different methods is based on the following papers [75, 76]. First of all, the correlation coefficients between correlated systematic uncertainties r_{ij}, the subscripts represent the trigger name, are calculated as

$$r_{ij} = \sum_{k=1}^{n} \sigma_k^{MB_{AND}} \sigma_k^{PHI} / \sqrt{\sum_{k=1}^{n} \sigma_k^{MB_{AND}} \sum_{k=1}^{n} \sigma_k^{PHI}} \tag{4.74}$$
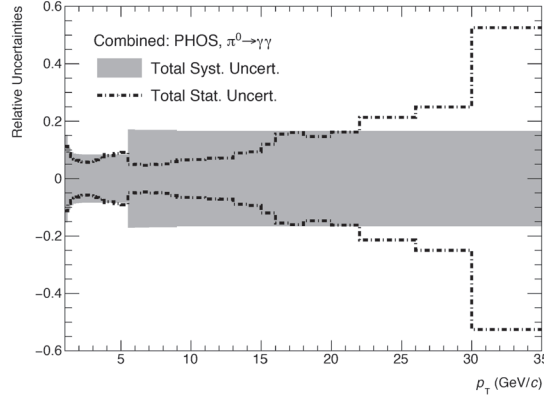
Figure 4.42: The combined total statistics and systematic uncertainties.

where σ represents the systematic uncertainty of each trigger. The correlation coefficient between same trigger set is 100%. Therefore, the diagonal elements in the correlation matrix should be unity. Furthermore, the assumption that the correlation fraction of statistical uncertainty between different triggers is 0% is put into this analysis.

The matrix V_{ij} can be computed as following with the statistical uncertainty σ_i^{stat}, the statistical uncertainty σ_i^{sys} and the correlation coefficients r_{ij} calculated with Equation 4.74.

$$V_{ij} = r_{ij}^{stat}\sigma_i^{stat}\sigma_j^{stat} + r_{ij}^{sys}\sigma_i^{sys}\sigma_j^{sys} \tag{4.75}$$

The weight vector w_i for combine spectra is calculated as

$$w_i = \frac{\sum_k \left(V_x^{-1}\right)_{ik}}{\sum_{jk} \left(V_x^{-1}\right)_{jk}}. \tag{4.76}$$

The average weighted mean, statistical uncertainties σ^{stat} and correlated systematic uncertainties σ^{sys} of each p_{T} bin can be found as

$$\overline{x} = \sum_i w_i x_i \tag{4.77}$$

$$\overline{\sigma}^{stat} = \sqrt{\frac{1}{\sum_i 1/\sigma_i^{stat}}} \tag{4.78}$$

$$\overline{\sigma}^{sys} = \sqrt{\sum_i \sum_j w_i w_j V_{ij}}. \tag{4.79}$$

The total systematic and statistical uncertainty of combined spectrum is shown in Figure 4.42;

Chapter 5

Experimental Results

In this section, the invariant cross section result as a function of transverse momentum is presented. The invariant cross-section of neutral pion is measured by using two different triggers. The PHOS spectrum is obtained by combining these two triggered data. The final spectrum of the ALICE experiment is obtained by combining the PHOS spectrum and the other measurement methods. The four different spectra are combined for obtaining the final result. These different measurements are introduced in the paper [78, 79].

5.1 Invariant Cross Section Results

The invariant cross section $Ed^3\sigma^{pp\to\pi^0 X}/dp^3$ is calculated by

$$E\frac{\mathrm{d}^3\sigma^{pp\to\pi^0 X}}{\mathrm{d}p^3} = \frac{1}{2\pi p_{\mathrm{T}}}\frac{\sigma_{\mathrm{MB_{AND}}}}{N_{\mathrm{evt}}^{\mathrm{MB_{AND}}}}\frac{1}{BR}\frac{1}{Acc\cdot\varepsilon}N_{\pi^0}^{\mathrm{rec}}\cdot\left(1 - C_{\mathrm{secondary}}\right). \tag{5.1}$$

$\sigma_{\mathrm{MB_{AND}}}$ is the cross section of $\mathrm{MB_{AND}}$ measured in Section 4.1.4. $N_{\mathrm{evt}}^{\mathrm{MB_{AND}}}$ is the number of analyzed event corresponding to $\mathrm{MB_{AND}}$ event. In case of the $\mathrm{MB_{AND}}$ analysis, it is the number of analyzed events. Meanwhile, in the PHI analysis, it is calculated as $\mathrm{MB_{AND}} = N_{\mathrm{evt}}^{\mathrm{PHI}} * f_{\mathrm{RF}}$ where $N_{\mathrm{evt}}^{\mathrm{PHI}}$ is the number of analyzed PHI events and f_{RF} is the rejection factor measured in Section 4.3.7. BR is the branching ratio of $\pi^0 \to \gamma\gamma$ decay channel and it is 98.823±0.034% [65]. $Acc\cdot\varepsilon$ is acceptance × total efficiency. In $\mathrm{MB_{AND}}$ analysis, the total efficiency is the product of the acceptance and reconstruction efficiency, while in PHI analysis, it is the product of the acceptance, reconstruction efficiency, and trigger efficiency. The acceptance×reconstruction efficiency and trigger efficiency are estimated in Section 4.5.3 and Section 4.5.4, respectively. $N_{\pi^0}^{\mathrm{rec}}$ is the number of reconstructed neutral pion explained in Section 4.6.1. $C_{\mathrm{secondary}}$ is the fraction of the secondaries including feed-down from $\mathrm{K_s^0}$ and created in the material.

The measured invariant cross-section spectrum is fitted with following three functions.

Levy-Tsallis function:

$$E\frac{\mathrm{d}^3\sigma}{\mathrm{d}p^3} = \frac{C}{2\pi}\frac{(n-1)(n-2)}{nT\big(nT + m(n-2)\big)}\left(1 + \frac{m_{\mathrm{T}} - m}{nT}\right)^{-n} \tag{5.2}$$

This function is based on Tsallis statistics. The free parameters C, n and T indicate a normalization factor, a power-law exponent at the high transverse momentum and a temperature obey the Boltzmann-Gibbs statistics. It is discussed in more detail in [73].

Two Component Model (TCM):

$$E\frac{\mathrm{d}^3\sigma}{\mathrm{d}p^3} = A_{\mathrm{e}}\exp\big(-E_{\mathrm{T,kin}}/T_{\mathrm{e}}\big) + A\left(1 + \frac{p_{\mathrm{T}}^2}{T^2 n}\right)^{-n} \tag{5.3}$$

The function is introduced to serve a convenient parametrization of the spectrum. It is the combination of the statistical mechanics and the hard scattering parts at low and high transverse momentum region, respectively. The first term follows the statistic mechanics, Boltzmann-Gibbs statistics, which is decreasing exponentially. In the term, $E_{\mathrm{T,kin}} = \sqrt{p_{\mathrm{T}}^2 + m^2} - m$ is the transverse kinematic energy of the neutral pion with m is the rest mass of neutral pion, A_{e} is the normalization factor and T_{e} has a dimension of the temperature. The second term represents the power-law behavior on the hard scattering which is derived from Levy-Tsallis function (Equation 5.2). The function is explained in more detail in [77].

Modified Hagedorn function:

$$E\frac{\mathrm{d}^3\sigma}{\mathrm{d}p^3} \quad = \quad A\big\{\exp\big(-(ap_{\mathrm{T}} + bp_{\mathrm{T}}^2)\big) + p_{\mathrm{T}}/p_0\big\}^{-n} \tag{5.4}$$

The function is close to the Hagedorn function [90] at low transverse momentum. This is developed by the PHENIX collaboration [89] to better describe the neutral pion spectrum for wider transverse momentum range. The function satisfies the exponential behavior like Boltzmann-Gibbs statistics at low transverse momentum and pure power-law slope at high transverse momentum.

Power low function:

$$E\frac{\mathrm{d}^3\sigma}{\mathrm{d}p^3} \quad = \quad Z \cdot p_{\mathrm{T}}^{-n} \tag{5.5}$$

The Z is a normalization factor and n is derived from the Equation 2.31.

The invariant cross section as a function of neutral pion transverse momentum of $\mathrm{MB_{AND}}$ and PHI triggered sample without event multiplicity class selection are shown in Figure 5.1 (top). The covering transverse momentum range of each data sample is $1.0 < p_{\mathrm{T}} < 12$ GeV/c and $5.5 < p_{\mathrm{T}} < 30$ GeV/c for $\mathrm{MB_{AND}}$ and PHI, respectively. The ratio of each data and the global fit result of TCM (Equation 5.3) is shown in Figure 5.1 (bottom). Within the uncertainties, two measurements are found to be consistent with each other in the overlapping region.

The invariant cross sections of each event multiplicity class are shown in Figure 5.2. The spectra of $\mathrm{MB_{AND}}$ and PHI are covering $1.0 < p_{\mathrm{T}} < 6.0$ GeV/c and $6.0 < p_{\mathrm{T}} < 16$ GeV/c, respectively. The circle marker represents the $\mathrm{MB_{AND}}$ and the open square marker is PHI. The black spectrum is without event multiplicity selection and same as Figure 5.1 but the binning is changed to fit the other event class results. The dashed line is TCM (Equation 5.3) fitted result.

5.2   Combine $\mathrm{MB_{AND}}$ and PHI Spectra

The spectra of each triggered data are combined with taking the correlated and uncorrelated uncertainties into account with the method explained in Section 4.6.9. In each event multiplicity class measurement, combined spectra are the connecting $\mathrm{MB_{AND}}$ and PHI at 6 GeV/c in this analysis.

The combined result without the event multiplicity class selection is shown in Figure 5.3. The combined PHOS spectrum covers transverse momentum range of $1.0 < p_{\mathrm{T}} < 30$ GeV/c. The total systematic uncertainties are combined with the method explained in Section 4.6.9. The total statistic uncertainties are calculated with the quadratic sum due to not correlations between them. The combined spectra of each event multiplicity class are shown in Figure 5.4. The combined systematic and statistic uncertainties are just from each spectrum.
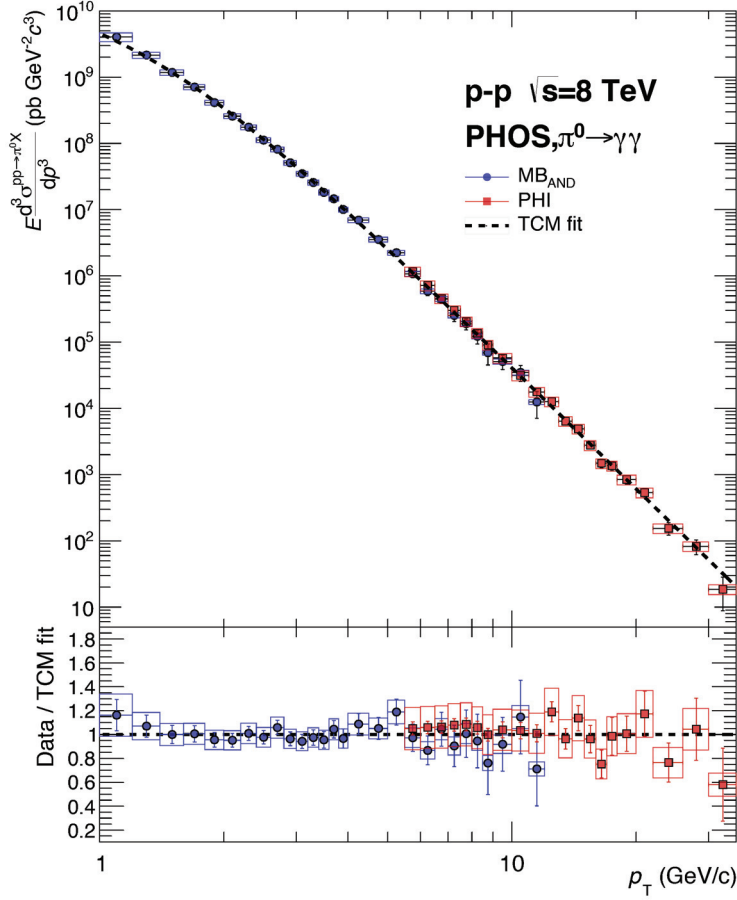
Figure 5.1: Top: The full corrected except the bin-shift correction invariant cross section of each triggered sample. The blue and red are MB_{AND} and PHI triggered results respectively. The spectra of MB_{AND} and PHI are covering $1.0 < p_T < 12$ GeV/c and $5.5 < p_T < 30$ GeV/c, respectively. The dashed line is the global fit result with Two Component Model (TCM) represented in Equation 5.3. Bottom: The ratio of the data and fitted result. The systematic uncertainty related to the reference cross section $\sigma_{MB_{AND}}$ is not included.

5.3 Combined Results with the Other Systems

The neutral pion is measured without the event multiplicity class selection in proton+proton collisions at $\sqrt{s} = 8$ TeV by the other detector systems in ALICE experiment, EMCal, Photon-Conversion Method (PCM) and PCM-EMCal hybrid [78]. The EMCal and PCM-EMCal hybrid methods are using not only MB_{AND} trigger but also high energy trigger deployed by the EMCal detector [78, 80]. The PCM method uses MB_{AND} triggered sample only, but its capability enables to measure very low transverse momentum range, below 1 GeV/c. The invariant mass distributions around neutral pion of each system in a given transverse momentum range are shown in Figure 5.5 [79]. The mass peak position and width of each system is shown in Figure 5.6 [78]. For mass peak width, the PCM result is the best resolution because the resolution is reflected by good track momentum resolution of about 0.7% at 1 GeV/c. The EMCal has a reasonable energy resolution and covers the wide area. Therefore, the mass width of the EMCal-PCM hybrid method is between the PCM and the EMCal method. The EMCal
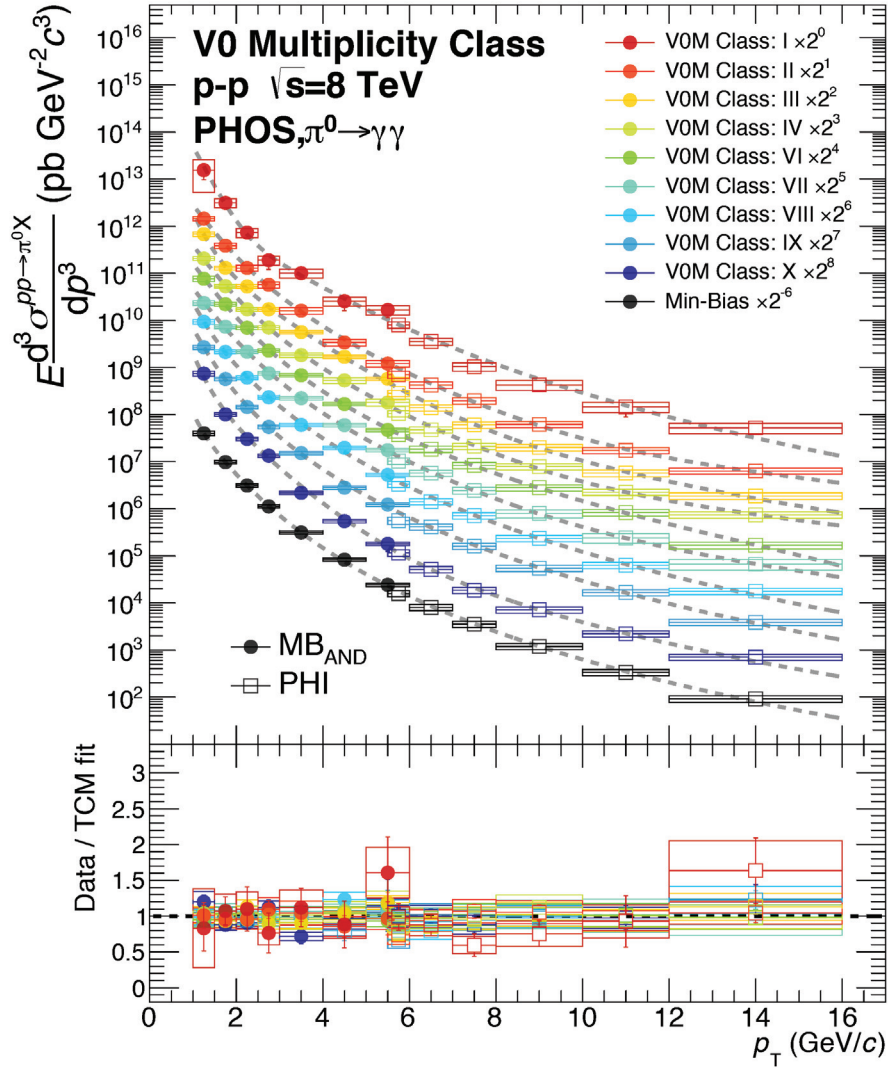
Figure 5.2: Top: The scaled invariant cross section of each event multiplicity class. The dashed line is the scaled global fit result with Two-Component Model (TCM) represented in Equation 5.3. Bottom: The ratio of the data and the fitted result of each trigger sample and each event multiplicity class. The systematic uncertainty related to the reference cross section $\sigma_{\mathrm{MB_{AND}}}$ is not included.

resolution becomes less in high transverse momentum range because the EMCal cell size is large, 6×6 cm^2, and the two photons start to merge around 10 GeV/c. Hence, it is difficult to measure one photon energy correctly. For the peak position of EMCal in a low transverse momentum region, the mass position becomes lower than true mass position due to detector non-linearity effect. On the other hand, in a high transverse momentum region, the mass position becomes larger than the true mass position due to cluster merging effect. The closed marker and open marker indicate the data and MC simulation, respectively. For the whole systems, the GEANT3 simulation describes the detector response precisely.

Each system spectrum is shown in Figure 5.7 (top). The PCM, EMCal and PCM-EMCal
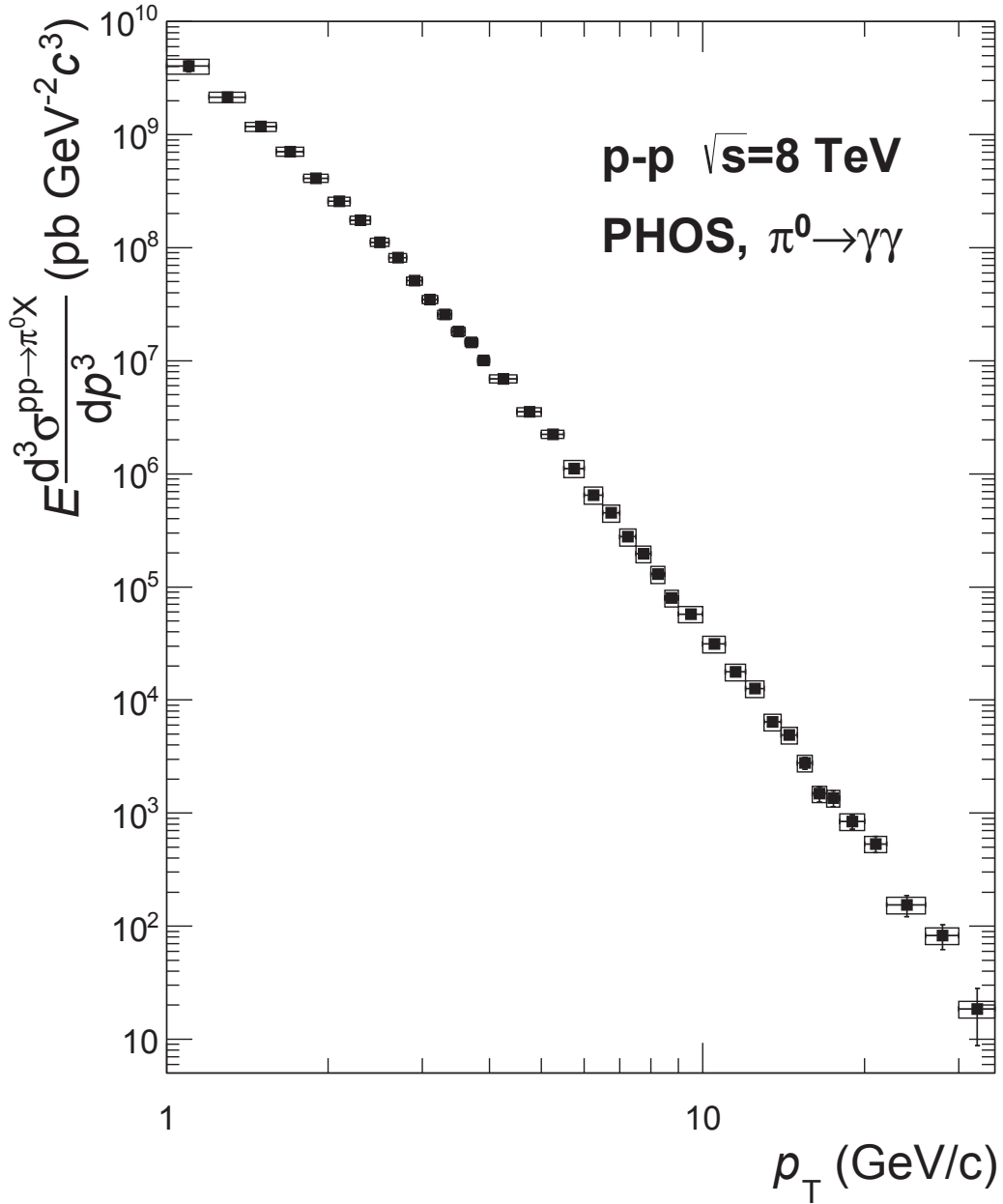
Figure 5.3: The combined spectrum witout the event multiplicity class selection. Total systematic uncertainties are calculated with the method introduced in Section 4.6.9. The total statistic uncertainties are the quadratic sum.

hybrid methods are covering the range of $0.3 < p_T < 12$ GeV/c, $1.2 < p_T < 20$ GeV/c and $0.8 < p_T < 35$ GeV/c, respectively. Therefore, the covering range of combined spectrum is $0.3 < p_T < 35$ GeV/c. The PCM-EMCal hybrid is using photons, one detected by EMCal and the other one detected by PCM technique. Therefore, there are correlated systematic uncertainties between PCM, EMCal, and PCM-EMCal. The method to combine these spectra is same as the
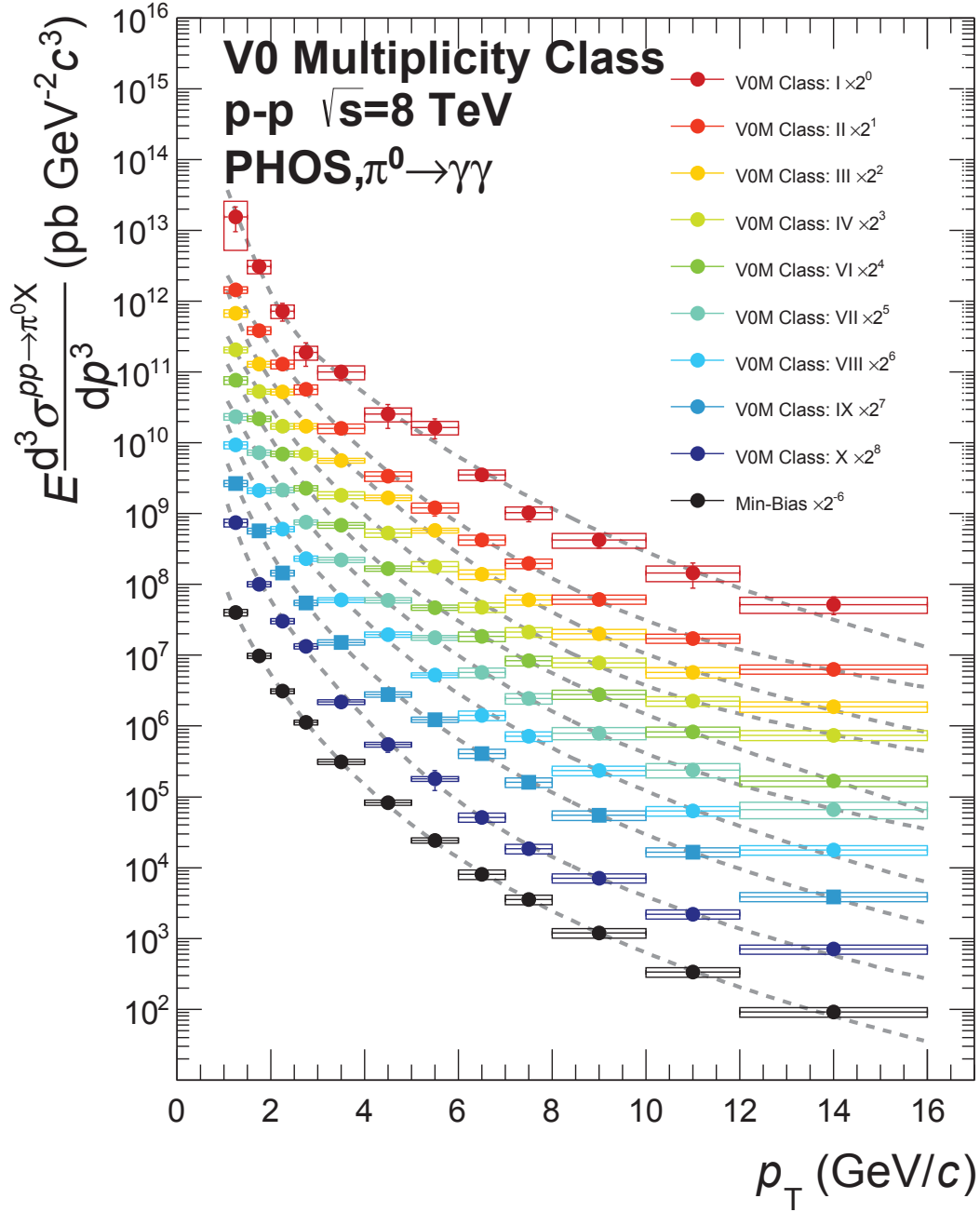
Figure 5.4: The combined spectra of each event multiplicity class. The covering range of each triggered spectra are $1.0 < p_T < 6.0$ GeV/c and $6.0 < p_T < 16$ GeV/c for MB$_{\text{AND}}$ and PHI, respectively.

method to combine the MB$_{\text{AND}}$ and PHI spectra of PHOS measurement explained in Section 4.6.9. Between PHOS and the other systems, there are no correlated systematic uncertainties. Hence, the systematic uncertainties between PHOS and the other systems are calculated with
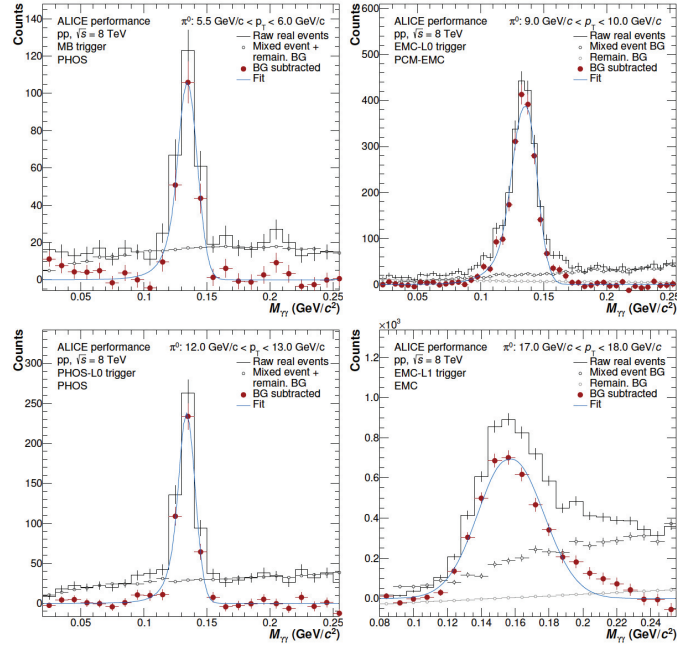
Figure 5.5: Invariant mass distribution around neutral pion mass of PCM-EMCal hybrid (top-left), EMCal (top-right), PHOS (bottom-left) and PCM (bottom-right) [79].
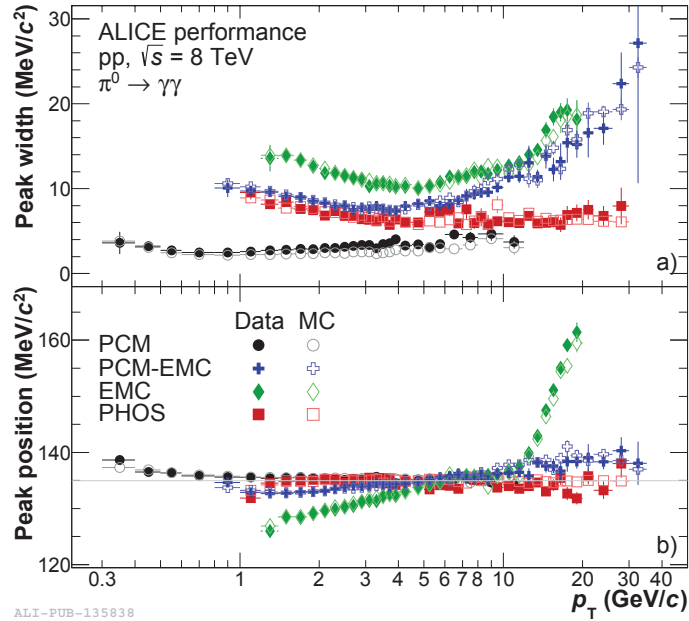
Figure 5.6: The plots show reconstructed neutral pion peak positions (bottom) and widths (top) of each reconstruction method for the transverse momentum bins. [78].

the quadratic sum method. The combined spectrum is shown in Figure 5.8.
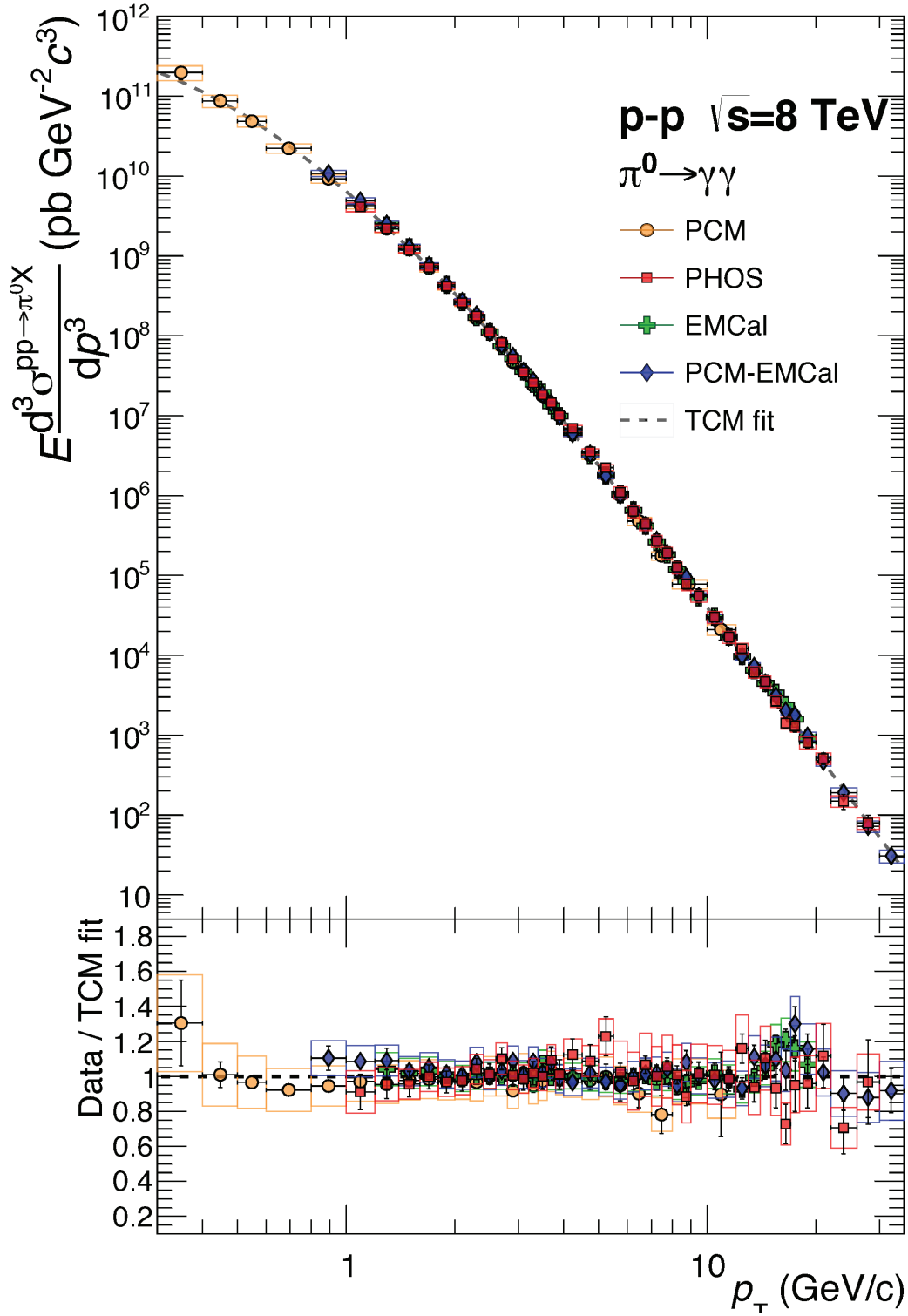
Figure 5.7: Top:The full corrected spectra measured by using PHOS (red), PCM (orange), EMCal (green) and PCM-EMCal hybrid (blue) [78]. Bottom: The ratio of the global fit to each system. Within the uncertainties, all results are consistent with each other.
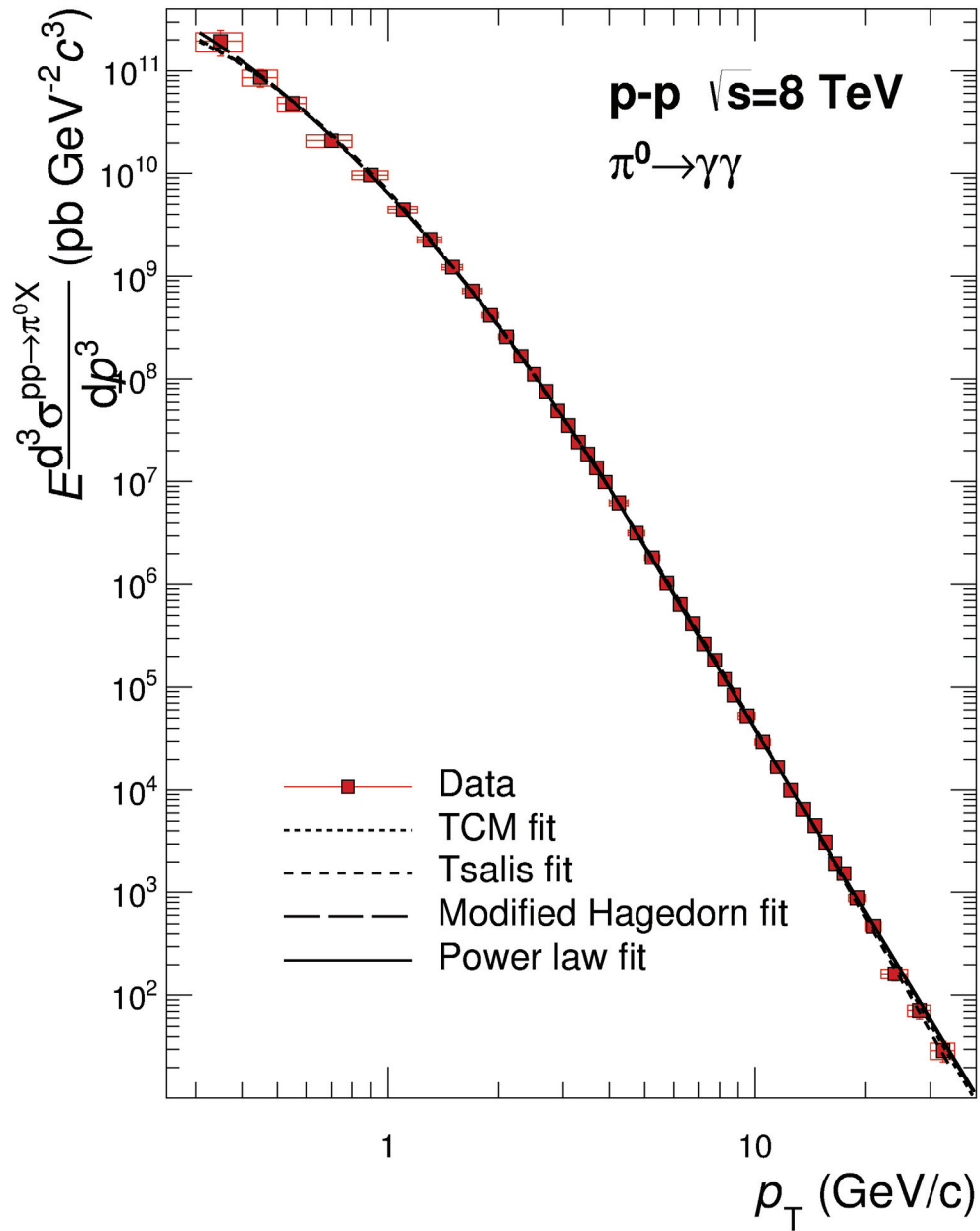
Figure 5.8: The combined invariant mass spectrum in proton+proton collisions at $\sqrt{s} = 8$ TeV. The fitted lines are also shown.

Chapter 6

Discussion

The final spectrum obtained by combining the four methods is compared with different collision energies, $\sqrt{s} = 0.0624$ TeV [83], $\sqrt{s} = 0.2$ TeV [84], $\sqrt{s} = 0.51$ TeV [85], $\sqrt{s} = 0.9$ TeV [74], $\sqrt{s} = 2.76$ TeV [86] and $\sqrt{s} = 7$ TeV [74]. Then, the higher-twist contribution explained in Section 2.3.5 is investigated at RHIC and LHC energies. Finally, the multiplicity dependence of neutral pion production and properties of high multiplicity events in proton+proton collisions at LHC energies are discussed.

6.1 Inclusive Spectrum

The combined spectrum is fitted with functions introduced in the previous section. The fitted results are shown in Figure 5.8 and summarized in Table 6.1 to Table 6.4.

The integrated yield at mid-rapidity, $\mathrm{d}N/\mathrm{d}y$, and the mean transverse momentum, $\langle p_\mathrm{T} \rangle$ are extracted from the fitted results with the following function,

$$\frac{\mathrm{d}N}{\mathrm{d}y} = \int_0^\infty f(p_\mathrm{T})\mathrm{d}p_\mathrm{T} \tag{6.1}$$

$$\langle p_\mathrm{T} \rangle = \int_0^\infty p_\mathrm{T} \cdot f(p_\mathrm{T})\mathrm{d}p_\mathrm{T} / \int_0^\infty f(p_\mathrm{T})\mathrm{d}p_\mathrm{T} \tag{6.2}$$

where $f(p_\mathrm{T})$ represents the differencial yield function obteined by the fitted result of the invariant cross section. The invariant cross-section is converted into the integrated yield by dividing with the inelastic cross section in proton+proton collisions at $\sqrt{s} = 8$ TeV and multiplying with $2\pi p_\mathrm{T}$. The inelastic cross section has been measured by the TOTEM experiment [40] and the value $\sigma_{pp}^{\mathrm{INEL}} = 74.7 \pm 17$ mb [81] is used. In addition to the measured systematic uncertainties, the fit function systematic uncertainties are considered. In this analysis, three different functions, Levy-Tsalis (Equation 5.2), TCM (Equation 5.3) and the modified Hagedorn function (Equation 5.4) are used to estimate the additional systematic uncertainty. The calculated integrated yield is $\mathrm{d}N/\mathrm{d}y = 3.291 \pm 0.129$ (stat) ± 0.997 (sys) ± 0.145 (fit-sys) and the mean transverse momentum is $\langle p_\mathrm{T} \rangle = 0.429 \pm 0.006$ (stat) ± 0.023 (sys) ± 0.018 (fit-sys) (GeV/c). The integrated yield is affected heavily by the magnitude of the spectrum at low transverse momentum. The systematic uncertainty at low transverse momentum region is large and so the integrated yield systematic uncertainty related to experimental measurement (sys) is large. The lowest measured transverse momentum is 0.3 GeV/c, but the yield is larger at lower transverse momentum region. Therefore, the extrapolation uncertainty which is reflected by from 0 to 0.3 GeV/c shape has been considered and it is found to achieve 45%.

The invariant cross section in proton+proton collisions at $\sqrt{s} = 0.0624$ TeV [83], 0.2 TeV [84], 0.51 TeV [85], 0.9 TeV [74], 2.76 TeV [86], 7 TeV [74] are shown in Figure 6.2. The fitted

results are also shown in the figure and the parameters obtained by fitting are summarized in from Tabel 6.5 to Tabel 6.7.

For all fit functions, the exponent n of the power-law part has the clear trend that it decreases with larger collision energy. The parameters corresponding to the total yield, C, A_e and Z, have an increasing trend with the larger collision energy. In TCM function, the parameter A_e of $\sqrt{s} = 0.51$ TeV has a large uncertainty because it is refrected by the statistics below 1 GeV/c, strongly. The spectrum of $\sqrt{s} = 0.51$ TeV starts form 1 GeV/c, so it has large uncertainty. The fitted results of $\sqrt{s} = 0.9$ TeV have large fluctuation because it is poor statistics in a whole transverse momentum range. Empirically, Levy-Tsallis function has been used to discuss the evolution of spectrum shape. As mentioned above, the exponent power-law n has a clear trend. A noteworthy thing in the trend is that it increases steeply below $\sqrt{s} = 0.51$ TeV. On the other hand, the parameter T which has a temperature dimension doesn't depend on the collision energy. The parameter C indicating the total yield as a function of collision energy is fitted with a function proportional to the collision energy and it is found to be $E\mathrm{d}^3\sigma^{pp\to\pi^0 X}/\mathrm{d}p^3 \propto \sqrt{s}^{0.37\pm0.02}$.

Table 6.1: Levy-Tsallis function [73] fitted result of neutral pion.

Levy-Tsallis	C (pb)	T (GeV)	n
π^0	$(2.4 \pm 0.2) \times 10^{11}$	0.121 ± 0.004	0.48

Table 6.2: Two Component Model (TCM) [77] fitted result of neutral pion.

TCM	A_e (pb GeV$^{-2}c^3$)	T_e (GeV)	A (pb GeV$^{-2}c^3$)	T (GeV)	n
π^0	$(6.7 \pm 2.7) \times 10^{11}$	0.14 ± 0.02	$(3.4 \pm 0.9) \times 10^{10}$	0.60 ± 0.03	3.03 ± 0.02

Table 6.3: Modified Hagedron function [89] fitted result of neutral pion.

Mod. Hagedorn	A (pb GeV$^{-2}c^3$)	a (GeV/c^{-1})	b (GeV/c^{-2})	p_0 (GeV/c)	n
π^0	(4.2 ± 4.6) (pb GeV$^{-2}c^3$)	0.2 ± 0.4	0.1 ± 0.2	0.45 ± 0.10	5.94 ± 0.12

Table 6.4: Power-Law function fitted result of neutral pion.

Power-Law	Z (pb GeV$^{-2}c^3$)	n
π^0	$(3.2 \pm 0.6) \times 10^{10}$	5.92 ± 0.09

The results at LHC collision energies are compared with the model based on the NLO pQCD framework with the MSTW2008 PDF [25] and DSS14 FF [82] which describes the neutral pion spectrum at RHIC energies [85]. The comparison with the experimental data is shown in Figure 6.1. The uncertainty of the model is caused by the scale options. The scale from $\mu = p_\mathrm{T}/2$ to $\mu = 2p_\mathrm{T}$ is used and the band is reflected from the scale. The covering transverse momentum range starts from 2.0 GeV/c because the precision becomes poor and it has large uncertainties in low transverse momentum region. For $\sqrt{s} = 0.9$ result which is close to RHIC collision energy, the model describes the data well. However, for the higher collision energies, in all transverse momentum region, the model is larger than the data by about 50 % at middle and high transverse momentum. Furthermore, the deviation beween $\sqrt{s} = 2.76$ TeV and $\sqrt{s} = 8$ TeV becomes systematically larger. In particular, they are different distinctly at high transverse momentum region where the precision of pQCD becomes better.
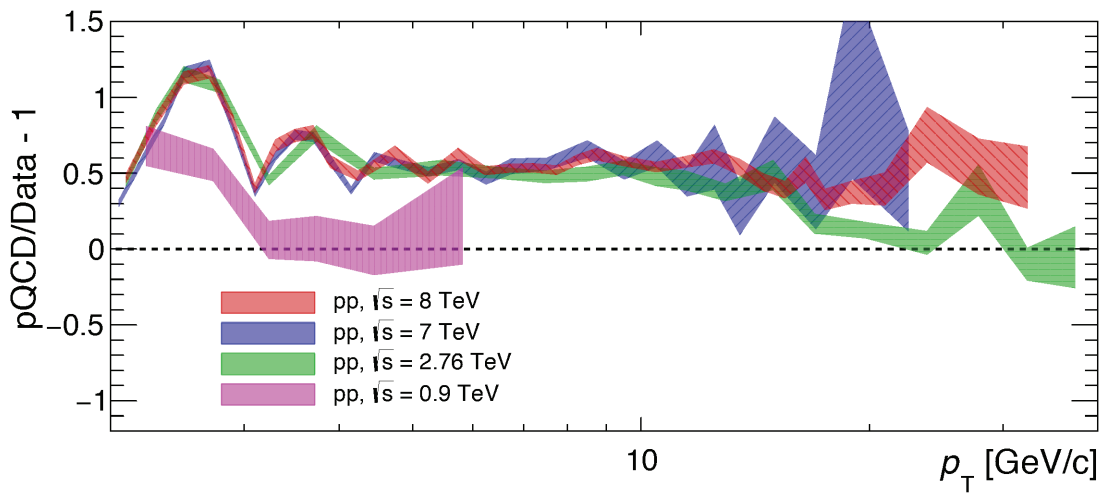
Figure 6.1: The ratio of the NLO pQCD with MSTW2008 PDF plus DSS14 FF and data of each collision energy.
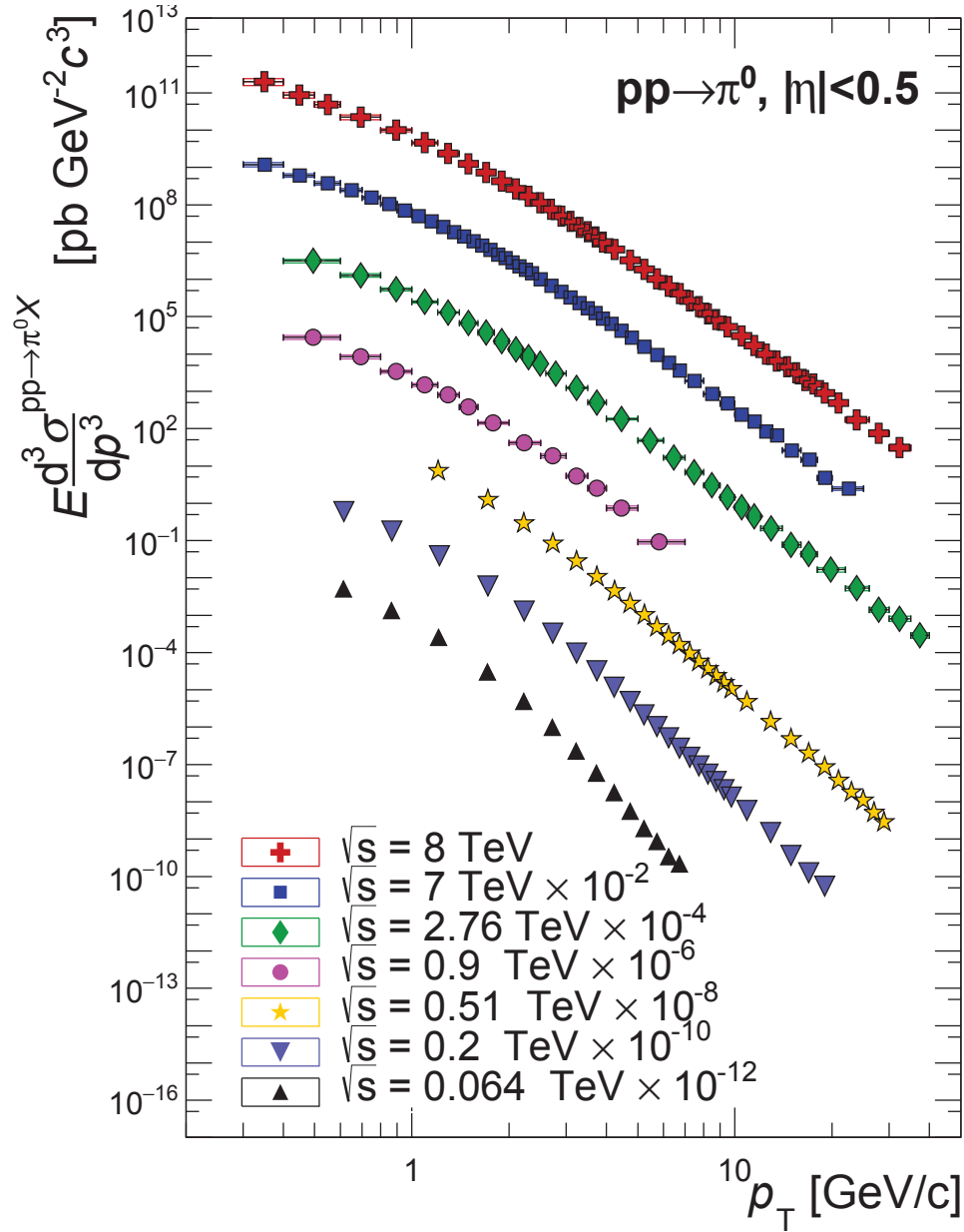
Figure 6.2: The neutral pion invariant cross-section in proton+proton collisions at RHIC and LHC collision energies.

Table 6.5: Levy-Tsallis function [73] fitted result of neutral pion in proton+proton collisions at LHC energies [83, 84, 85, 86, 74].

Levy-Tsallis fit range	$\sqrt{s}$ (TeV)	C (pb)	T (GeV)	n
[0.3,35]	8	$(2.4 \pm 0.2) \times 10^{11}$	0.121 ± 0.004	6.46 ± 0.04
[0.3,25]	7	$(1.79 \pm 0.09) \times 10^{11}$	0.138 ± 0.003	6.80 ± 0.06
[0.4,40]	2.76	$(1.29 \pm 0.09) \times 10^{11}$	0.128 ± 0.004	7.04 ± 0.07
[0.4,6]	0.9	$(8.80 \pm 0.51) \times 10^{10}$	0.126 ± 0.046	7.51 ± 1.76
[1.0,30]	0.51	$(1.35 \pm 0.30) \times 10^{11}$	0.102 ± 0.006	7.89 ± 0.09
[0.5,20]	0.2	$(5.14 \pm 0.47) \times 10^{10}$	0.121 ± 0.004	9.42 ± 0.11
[0.5,7]	0.0624	$(3.39 \pm 0.39) \times 10^{10}$	0.138 ± 0.006	12.6 ± 0.4

Table 6.6: Two Component Model (TCM) [77] fitted result of neutral pion in proton+proton collisions at LHC energies.

TCM fit range	$\sqrt{s}$ (TeV)	A_e (pb GeV$^{-2}c^3$)	T_e (GeV)	A (pb GeV$^{-2}c^3$)	T (GeV)	n
[0.3,35]	8	$(6.7 \pm 2.7) \times 10^{11}$	0.14 ± 0.02	$(3.4 \pm 0.9) \times 10^{10}$	0.60 ± 0.03	3.03 ± 0.02
[0.3,25]	7	$(4.2 \pm 0.5) \times 10^{11}$	0.144 ± 0.007	$(3.7 \pm 0.3) \times 10^{10}$	0.693 ± 0.011	3.064 ± 0.012
[0.4,40]	2.76	$(7.9 \pm 3.5) \times 10^{10}$	0.57 ± 0.03	$(7.4 \pm 1.3) \times 10^{10}$	0.44 ± 0.02	3.08 ± 0.03
[0.4,6]	0.9	$(1.8 \pm 0.6) \times 10^{10}$	0.008 ± 0.664	$(10.5 \pm 1.4) \times 10^{10}$	0.363 ± 0.001	2.96 ± 0.09
[1.0,30]	0.51	$(7 \pm 68) \times 10^{14}$	0.07 ± 0.04	$(1.1 \pm 0.4) \times 10^{10}$	0.59 ± 0.03	3.72 ± 0.03
[0.5,20]	0.2	$(1.2 \pm 0.9) \times 10^{11}$	0.14 ± 0.03	$(6.7 \pm 2.7) \times 10^{9}$	0.58 ± 0.04	4.22 ± 0.04
[0.5,7]	0.0624	$(1.2 \pm 0.7) \times 10^{11}$	0.14 ± 0.03	$(3.2 \pm 2.7) \times 10^{9}$	0.62 ± 0.07	5.4 ± 0.2

Table 6.7: Power-Law function fitted result of neutral pion in proton+proton collisions at LHC energies.

Power-Law fit range	$\sqrt{s}$ (TeV)	Z (pb GeV$^{-2}c^3$)	n
[3.5,35]	8	$(3.2 \pm 0.6) \times 10^{10}$	5.92 ± 0.09
[3.5,25]	7	$(3.0 \pm 0.6) \times 10^{10}$	5.95 ± 0.10
[3.5,40]	2.76	$(1.9 \pm 0.8) \times 10^{10}$	6.2 ± 0.2
[3.5,6]	0.9	$(1.6 \pm 3.3) \times 10^{10}$	6.7 ± 1.6
[3.5,30]	0.51	$(1.41 \pm 0.09) \times 10^{10}$	7.21 ± 0.03
[3.5,20]	0.2	$(1.29 \pm 0.10) \times 10^{10}$	8.07 ± 0.04
[3.5,7]	0.0624	$(1.5 \pm 0.3) \times 10^{10}$	9.5 ± 0.1

6.2 Higher-Twist Effect

The particles produced by the jet fragmentation have associated hadrons within a certain area. The jet properties are studied deeply and almost all associated hadrons are known to exist in a cone of $R < 0.4$. The cone parameter, R, is defined as

$$R = \sqrt{(\eta_{\pi^0} - \eta_i)^2 + (\phi_{\pi^0} - \phi_i)^2} \qquad (6.3)$$

where i represents i^{th} accosiated particles.

The particle produced by the higher-twist process is isolated because there are no fragmentation particles. Therefore, the hadrons produced by the higher-twist process may be identified with the isolation cut. When there is no charged particle and residual clusters detected by PHOS within a cone of $R < 0.4$, the neutral pion is assumed to be isolated. The cut is called isolation cut. The invariant cross-section of neutral pion with isolation cut is shown in Figure 6.3 (top) compared with the inclusive measurement. The black and red express the inclusive and isolated spectra, respectively. The bottom plot in Figure 6.3 shows the fraction of neutral pion passing the isolation cut. At low transverse momentum region, the contribution reaches ∼20%, but it decreases with the larger transverse momentum and reaches ∼5%.

To check if some of the high transverse momentum particles are produced by the higher-twist process, the fraction is compared with the full MC simulation, Pythia 8-Monash 2013 and the realistic detector response simulator (GEANT3 [71]) which is used in Section 4.5.3. The simulated result is plotted in Figure 6.3 (bottom) red band. The contribution can be seen at the same magnitude in the whole transverse momentum range. In Pythia 8, the higher-twist process is not included. Therefore, the particles passed isolation cut can be explained with unphysical effect, e.g. inefficient areas of detectors, and the significance of the higher-twist production is not found with the isolation method.

The exponent n_{eff} is calculated for further study of the higher-twist production. The n_{eff} is calculated from two different energies with Equation 2.36. The n_{eff} of the neutral pion from $\sqrt{s_1} = 8$ TeV, $\sqrt{s_2} = 2.76$ TeV (red) [86] and $\sqrt{s_1} = 510$ GeV, $\sqrt{s_2} = 200$ GeV measured by PHENIX experiment (blue) [84, 85] are shown in Figure 6.4. The inclusive jet result from $\sqrt{s_1} = 8$ TeV, $\sqrt{s_2} = 2.76$ TeV measured by CMS experiment [87, 88] (green) is also plotted in the same figure. The n_{eff} of the neutral pion from $\sqrt{s_1} = 8$ TeV, $\sqrt{s_2} = 2.76$ TeV is constant in the range of $2 \times 10^{-3} < x_{\text{T}} < 3 \times 10^{-2}$. The result is fitted with the constant function and the fitted value is found to be $n_{\text{eff}} = 4.897 \pm 0.010$. On the other hand, the result of $\sqrt{s_1} = 510$ GeV, $\sqrt{s_2} = 200$ GeV is not flat and it is higher value than the LHC energies, $5.5 < n_{\text{eff}} < 6.0$ in the range of $3 \times 10^{-2} < x_{\text{T}} < 10^{-1}$. The jet result from $\sqrt{s_1} = 8$ TeV, $\sqrt{s_2} = 2.76$ TeV is also constant and the fitted result is found to be $n_{\text{eff}} = 4.60 \pm 0.02$. The plot indicates the important information relevant to the difference between LHC and RHIC energy of the hadron
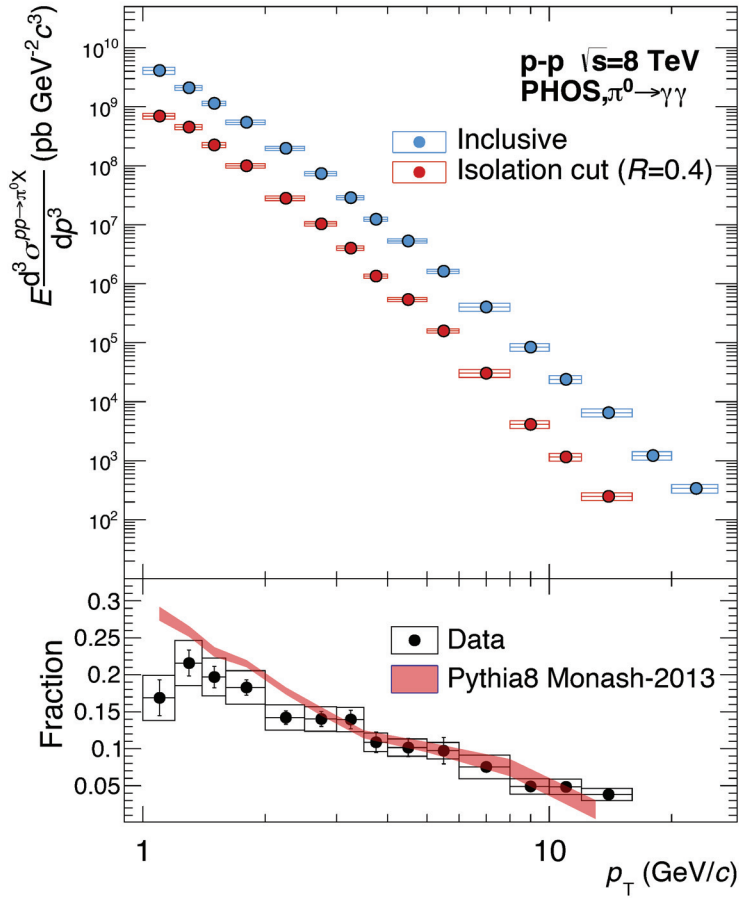
Figure 6.3: Top: The invariant cross section on inclusive (blue) and isolated (red) measuremd by PHOS. The cone size of $R = 0.4$ is used for the isolation cut. Bottom: The fraction of the neutral pion passing the isolation cut, data (black) and Pythia 8 (red).

production mechanism. At the LHC energy, the n_{eff} of neutral pion and jet are consistent and this result suggests that almost all hadrons are produced by the jet fragmentation. Meanwhile, at the RHIC energy, the n_{eff} of neutral pion is larger than the jet result. This suggests that hadrons are produced by not only the jet fragmentation but also the higher-twist production mechanism, i.e. the direct hadron production. Therefore, the higher-twist contribution should be taken into account for several model calculation, e.g. the hadron energy loss in the strong interaction matter at the RHIC experiments. The result suggests that higher-twist contribution should be measured quantitatively at RHIC to compare the several physics results at LHC and RHIC.

The particle production difference is arisen from the parton distribution function. The gluon contribution becomes large extremely at low Bjorken-x region (Figure 2.8). The higher-twist process needs at least one quark in the first hard subprocess (Figure 2.11). Therefore, at the LHC energies, low Bjorken-x region, the higher-twist contribution becomes very small. On the other hand, at RHIC collision energies, large Bjorken-x region, the fraction of the quark contents in the nucleon is not negligible. This leads to the difference of hadron production mechanism at LHC and RHIC.

In order to see the higher-twist contributions as a function of transverse momentum, the
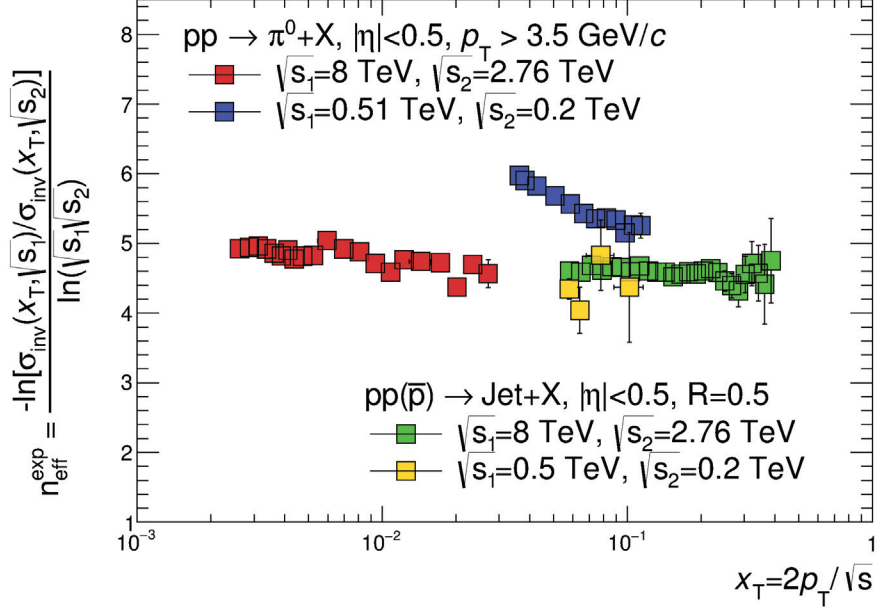
Figure 6.4: The measured exponent n_{eff} of the neutral pion and jet.

simplest two-component model [31] is introduced as

$$E\frac{\mathrm{d}^3\sigma^{pp\to\pi^0 X}}{\mathrm{d}p^3} \equiv \sigma^{\text{inv}} \propto \frac{A(x_{\text{T}})}{p_{\text{T}}^4} + \frac{B(x_{\text{T}})}{p_{\text{T}}^6} \tag{6.4}$$

corresponding to the jet fragmentation $(A(x_{\text{T}})/p_{\text{T}}^4)$ and the higher-twist $(B(x_{\text{T}})/p_{\text{T}}^6)$ contributions. The measured effective exponent n_{eff} is studied in [31] and it is found to be described as

$$n_{\text{eff}} \equiv -\frac{\partial \ln\sigma^{\text{inv}}}{\partial \ln p_{\text{T}}} + n^{\text{NLO}}(x_{\text{T}}) - 4 \tag{6.5}$$

$$= \frac{2B/A}{p_{\text{T}}^2 + B/A} + n^{\text{NLO}}(x_{\text{T}}). \tag{6.6}$$

This equation satisfies that $n_{\text{eff}} \to n^{\text{NLO}} + 2$ for $B/A \to \infty$ and $n_{\text{eff}} \to n^{\text{NLO}}$ for $B/A \to 0$. The prior corresponds to that there is only the higher-twist contribution and the latter is only the jet contribution. The value of B/A in the formula is corresponding to the relative strength of higher-twist cross-section to the jet cross-section. The calculated B/A for $\sqrt{s} = 0.51$ TeV and $\sqrt{s} = 8$ TeV as a function of transverse momentum are shown in Figure 6.5. The parameter n^{NLO} should be the same as the value of jet. Therefore, this time, the measured values (green and yellow in Figure 6.4) are used for the calculation. At the whole transverse momentum range, the higher-twist contribution at $\sqrt{s} = 0.51$ TeV is larger than at $\sqrt{s} = 8$ TeV. However, above 20 GeV/c, the contribution becomes large at $\sqrt{s} = 8$ TeV. This behavior is caused by the $n_{\text{eff}}^{\text{exp}}$ measurement. The $n_{\text{eff}}^{\text{exp}}$ is measured by two different energies. The higher-twist contribution at $\sqrt{s} = 2.76$ TeV is expected to be not negligible above 20 GeV/c. The fraction of gluon-gluon, gluon-quark and quark-quark scattering processes to neutral pion production at mid-rapidity for RHIC and LHC are shown in Figure 6.6 [101]. At RHIC energy, the scattering involving at least one quark, sum of the gluon-quark and the quark-quark, is expected to be larger than the gluon-gluon scattering from ~ 3 GeV/c. At LHC energy, the scattering fraction
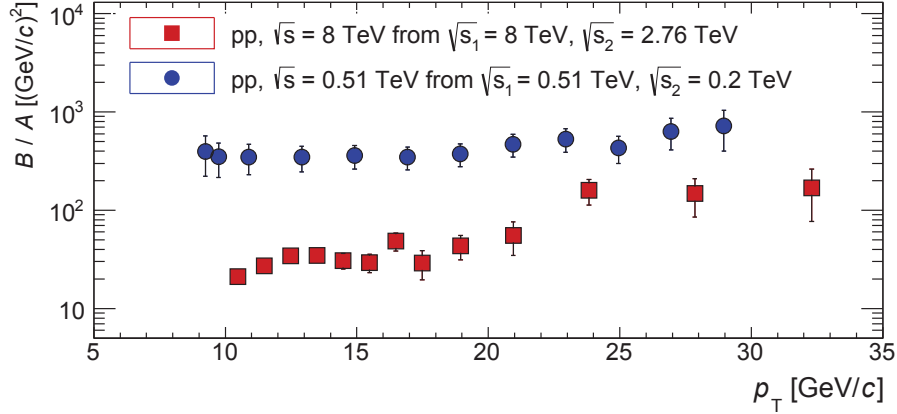
Figure 6.5: The value of B/A calculated by $n_{\mathrm{eff}}^{\mathrm{exp}}$ for $\sqrt{s} = 0.51$ TeV and $\sqrt{s} = 8$ TeV.

is found to be larger from ~ 25 GeV/c. The amplitude of B/A starts to be large from almost same transverse momentum and the expectation is consistent with the result.
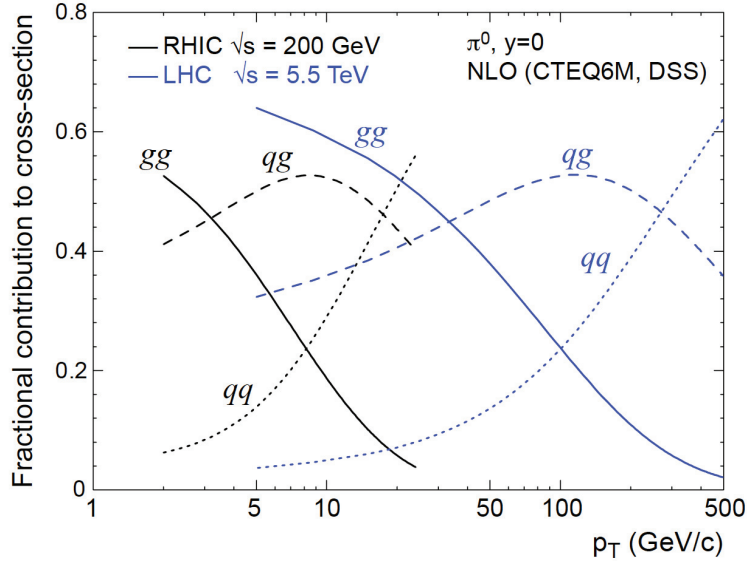
Figure 6.6: The fraction of gluon-gluon, gluon-quark and quark-quark scattering processes to neutral pion production at mid-rapidity for RHIC (black) and LHC (blue) [101].

The result may explain the discrepancy of nuclear modification factor of the inclusive charged particles in proton-lead collisions at $\sqrt{s_{\mathrm{NN}}} = 5.02$ TeV between ALICE and CMS [92]. The nuclear modification factor in proton-lead collisions is calculated as

$$R_{\mathrm{pPb}}(p_{\mathrm{T}}) = \frac{\mathrm{d}N^{\mathrm{pPb}}/\mathrm{d}p_{\mathrm{T}}}{\langle N_{\mathrm{coll}}\rangle\, \mathrm{d}N^{pp}/\mathrm{d}p_{\mathrm{T}}} = \frac{\mathrm{d}N^{\mathrm{pPb}}/\mathrm{d}p_{\mathrm{T}}}{T_{\mathrm{pPb}}\mathrm{d}\sigma^{\mathrm{pp}}/\mathrm{d}p_{\mathrm{T}}} \tag{6.7}$$

where N_{pPb} and N_{pp} are the particle yields in proton-lead collisions and proton+proton collisions, σ^{pp} is the particle cross section in proton+proton collisions, the ratio $T_{\mathrm{pPb}} = \langle N_{\mathrm{coll}}\rangle / \sigma^{\mathrm{pp}}_{\mathrm{inel}}$

indicates the nuclear overlap function obtained by a Glauber model of the nuclear collision geometry [91]. When the factor is a unit, $R_{\mathrm{pPb}} = 1$, the particle yield induced by the proton-lead collisions can be described as the overlap of the proton+proton collisions. When the factor is not 1, it suggests there are some nuclear effects. The results of ALICE and CMS are shown in Figure 6.7. The ALICE result shows the plateau above 10 GeV/c. However, the CMS result becomes larger than 1. The ALICE measurement uses the minimum-bias triggered data, so it contains both the jet fragmentation and the higher-twist effect. On the other hand, CMS uses the jet triggered sample. Therefore, the result of CMS includes charged particles from only the jet fragmentation.
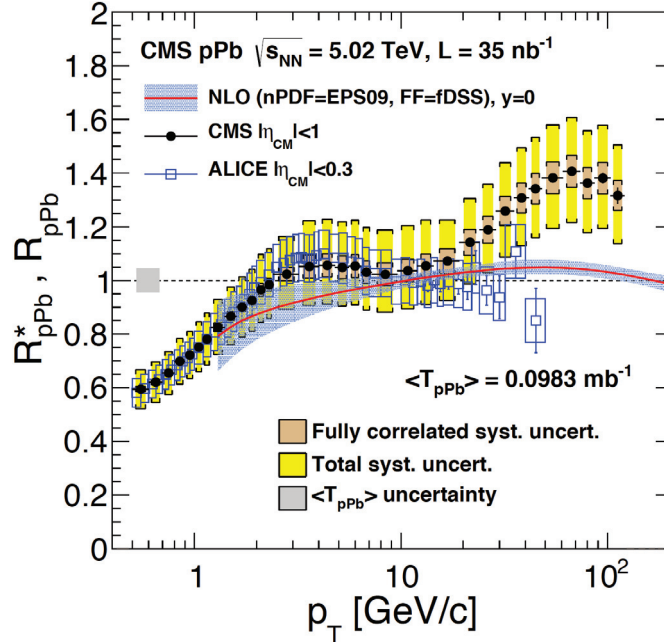
Figure 6.7: The nuclear modification factor of charged particle in proton-lead collisions measured by ALICE and CMS [92].

For the energy of $\sqrt{s} = 5.02$ TeV, the higher-twist contribution becames large from $\sim$ 15 GeV/c which is derived from the Figure 6.5 and the relationship btween Bjorken-x at mid-rapidity and the collision energy ($x \sim 2p/\sqrt{s}$). The charged particles around 15 GeV/c originated from jet fragmentation typically come from $100 \sim 200$ GeV/c jets. These jets are generated by the partons with Bjorken-$x = 10^{-2} \sim 10^{-1}$ at mid-rapidity. The parton density in the nucleus is changed by the nuclear effect explained in Section 2.3.3 and the Bjorken-x regions is the anti-shadowing area (Figure 2.9). Hence, the nuclear modification factor of charged particles originated from only jet fragmentation enhances. On the other hand, the particles originated from the higher-twist at around 15 GeV/c are generated by partons with Bjorken-$x \sim 10^{-3}$ at mid-rapidity. These partons are reduced in the nuclear by the shadowing effect (Figure 2.9). Consequently, the nuclear modification factor of charged particles originated from the higher-twist effect become fewer.

For the ALICE measurement, above 15 GeV/c region, there are two contributions, the higher-twist effect and the jet fragmentation because the events are collected by the minimum-bias trigger. In lead nuclear, the higher-twist contribution is reduced by the shadowing, but the jet fragmentation is enhanced by the anti-shadowing. The measured result is the sum of these contributions. On the other hand, for the CMS measurement, there are charged particles originated from only the jet fragmentation because the jet triggered sample is used. In the

nuclear, the contribution of jet fragmentation is enhanced by the anti-shadowing. For the reason, there is the discrepancy between ALICE and CMS.

6.3   Multiplicity Dependence

The neutral pion yield of each multiplicity event class relative to the average multiplicity as a function of the charged multiplicity in $|\eta| < 1.0$ is presented in Figure 6.8. A similar increase with the charged multiplicity is observed in the low transverse momentum result (blue). On the other hand, the high transverse momentum result (red) shows a steeper increase than the low transverse momentum and the multiplicity. This result indicates that the high transverse momentum particles have the strong impact on the high multiplicity event.

The Pythia 8 with and without the CR effect (Section 2.4.2) is also shown in Figure 6.8. The without the CR calculation is found out that at both low and high transverse momentum region, they increase similarly to the multiplicity evolution. Meanwhile, with the CR calculation is reviewed that the spectra of both low and high transverse momentum region are steeper increasing than the linear and it reproduces the data. This result suggests that the CR effect is not negligible and plays an important role in the particle spectrum.

The differential invariant cross-section is fitted with Levy-Tsallis function (Equation 5.2). The multiplicity dependence of exponent power-law n in the equation is plotted in Figure 6.9. The slope is found not to be affected by the event multiplicity class. In Pythia 8 both with and without CR also show the same behavior.
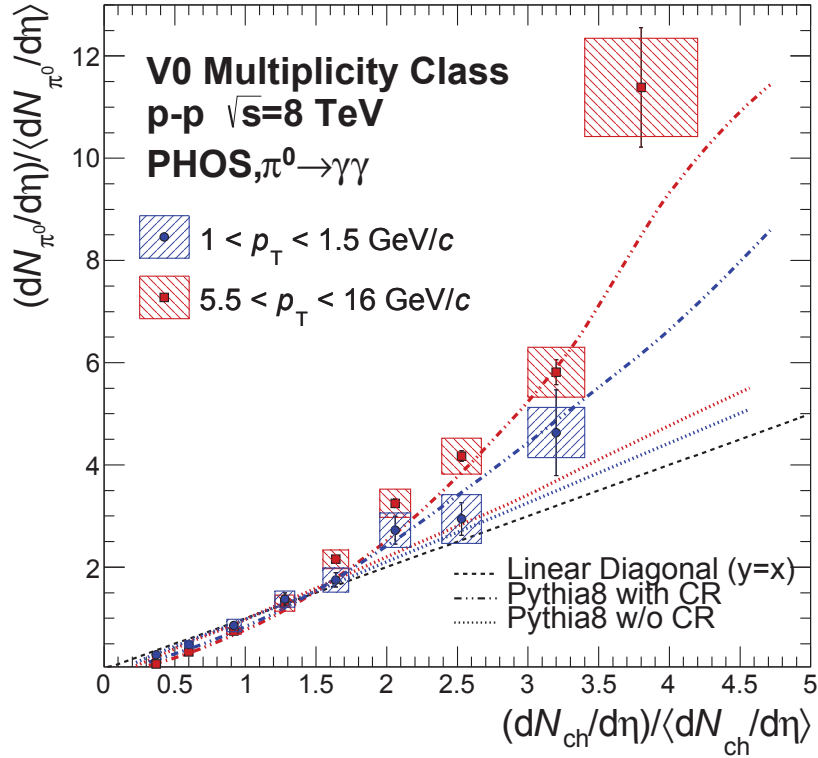
Figure 6.8: The relative neutral pion yield measured by PHOS as a function of relative charged-particle multiplicity at mid-rapidity ($|\eta| < 1.0$) measured by SPD in two transverse momentum intervals, compared with theoretical calculations. The blue and red points represent the low and high transverse momentum data, respectively. The dashed line represents a diagonal line to show a linearity guide.
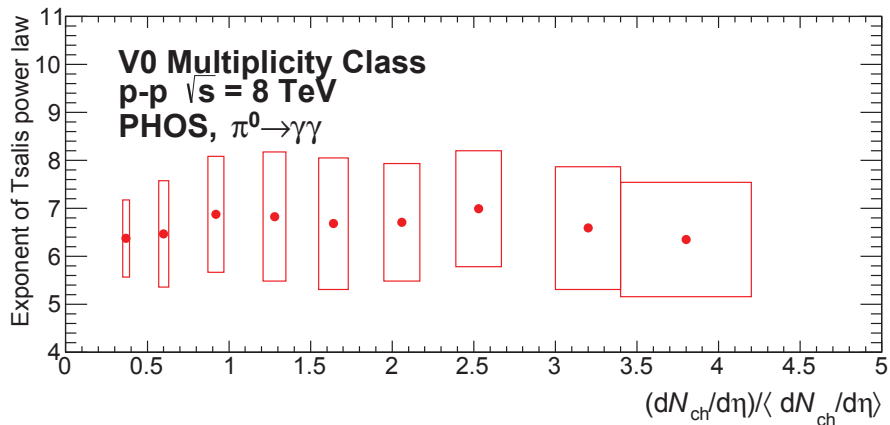
Figure 6.9: The exponent power-law n as a function of the event multiplicity class.

Chapter 7

Conclusion

The measurement of neutral pion production in proton+proton collisions at $\sqrt{s} = 8$ TeV has been carried out with ALICE experiment located at LHC.

Neutral pions have been reconstructed from two photons detected by PHOS electromagnetic calorimeter which is composed of lead-tungstate ($PbWO_4$) crystal. To enhance the statistics in high transverse momentum region, the data sample of not only minimum-bias (MB_{AND}), but also the PHOS high energy photon trigger (PHI) have been analyzed. Because of these data sample, neutral pions have been measured from 1.0 GeV/c to 30 GeV/c without the event multiplicity separation and 1.0 GeV/c to 16 GeV/c in each event multiplicity class. Other ALICE sub-systems, PCM, EMCal and PCM-EMCal hybrid, also have measured the neutral pion spectra without the event multiplicity selection. The PHOS result is consistent with the other sub-systems results. When all sub-system results have been combined into one spectrum, the covering kinematic range becomes wider from 0.3 GeV/c to 35 GeV/c.

The combined spectrum has been compared with the theoretical predictions. The pQCD with MSTW2008 (PDF) and DSS14 (FF), which predicts the spectrum at $\sqrt{s} = 510$ GeV very well, overestimates the LHC energies by about 50%. The spectrum is also compared with the other collision energies and the relationship between the production cross-section and the collision energy is found to be $\sqrt{s}^{-0.37\pm0.02}$.

The neutral pions produced by the higher-twist process (direct hadron production) have been searched for by using the isolation cut method. However, the isolated neutral pion expected to be originated from the higher-twist effect is not observed below 12 GeV/c at $\sqrt{s} = 8$ TeV. In terms of the exponent n_{eff}, the higher-twist effect has been investigated and compared with the jet results with several energy combinations. At the LHC energies, the exponents n_{eff} of neutral pion and of jet have been found to be both ~ 5. On the other hand, at the RHIC energies, the jet result is consistent with the LHC energies, but neutral pion result represents larger than the jet by ~ 1. This result indicates that the higher-twist contribution can not be ignored at the RHIC collision energies, but the contribution becomes smaller at LHC energies. The higher-twist effect is measured quantitatively as a function of transverse momentum by using a simple two-component model. At LHC energies, even though the higher-twist contribution is still smaller than at RHIC energies, it enhances from a dozen GeV/c. This result has a potential to explain the discrepancy of the nuclear modification factor of inclusive charged particles in proton-lead collisions.

The event multiplicity dependence of the neutral pion production has been measured by eight event multiplicity classes. The higher transverse momentum neutral pion has been found to grow steeper than the lower one with the event multiplicity. These two interval results have been compared with Pythia8 to investigate the color reconnection effect. The comparison reveals that the color reconnection has significant influence to the particle production, especially for the high multiplicity event.

The difference of particle production mechanism between RHIC and LHC gives an im-

portant insight of the Quark-Gluon Plasma (QGP) study. For example, the high transverse momentum particle suppression in heavy ion collisions can be affected heavily by the higher-twist effect. The phenomenon is caused by the particle energy loss during traversing the QGP and the amount of energy loss depends on the particle species and the particle structure. Many energy loss models calculate the parton energy loss and the formed hadron energy loss is not considered. These models lead the correct way in case of LHC energy because the higher-twist effect can be ignored. However, in case of the RHIC energy, there is the higher-twist contribution and the energy loss of the formed hadron should be considered. Furthermore, the "collectivity" is one of the important signal from the QGP to investigate its property. The collectivity is caused by the pressure gradient of reaction matter and the correlation between partons in the QGP. However, there is a possibility to produce the additional collectivity by the color reconnection mechanism and it can embarrass the collectivity measurement. The effect is expected to be predominant at LHC because it is caused by the multi parton interaction and its strength is proportional to the number of the parton interaction.

This thesis reveals the particle production mechanism in proton+proton collisions and suggests the importance of higher-twist effect for RHIC and the color reconnection effect for LHC, respectively. These results probably help to understand the discrepancies between RHIC and LHC results and lead correct understanding of not only the standard model and but also beyond the standard model.

Acknowledgements

Bibliography

[1] ALICE Collaboration, "The ALICE experiment at the CERN LHC", *JINST* vol. 3, no. S08002, 2008.

[2] ALICE Collaboration, "Performance of the ALICE Experiment at the CERN LHC", *CERN-PH-EP-2014-031*, 2014.

[3] CMS Collaboration, "Observation of a new boson at a mass of 125 GeV with the CMS experiment at the LHC", *Phys. Lett.*, B716 (1):3061, 2012.

[4] ATLAS Collaboration, "Observation of a new particle in the search for the Standard Model Higgs boson with the ATLAS detector at the LHC", *Phys. Lett.*, B716 (1):129, 2012.

[5] L. Evans, "THE CERN LARGE HADRON COLLIDER: ACCELERATOR AND EXPERIMENTS", *JINST*, vol. 3, no. S08001, 2008.

[6] O. S. Bruning, "LHC Design Report Vol.1: The LHC Main Ring", *CERN-2004-003-V1*, 2004

[7] O. S. Bruning, "LHC Design Report Vol.1: The LHC Infrastructure and General Services", *CERN-2004-003-V2*, 2004

[8] O. S. Bruning, "LHC Design Report Vol.3: The LHC Injector Chain", *CERN-2004-003-V3*, 2004

[9] Masayuki Nakahata et al., "Atmospheric Neutrino Background and Pion Nuclear Effect for Kamioka Nucleon Decay Experiment", *J. Phys. Soc. Jpn.*, 55, 3786-3805, 1986.

[10] F. Cooper et al., "Supersymmetry and quantum mechanics", *Phys. Rep.*, 251, 126, 1995.

[11] Particle Data Group, "Review of QUANTUM CHROMODYNAMICS", http://pdg.lbl.gov.

[12] Gauss Centre for Supercomputing, "Numerical Determination of the Phase Diagram of Nuclear Matter", http://www.gauss-centre.eu.

[13] M. G. Alford et al., "Color superconductivity in dense quark matter", *Rev. Mod. Phys.*, 80, 1455, 2008.

[14] Nuclear Instruments and Methods A, 499 (2003) 235-244.

[15] PHENIX Collaboration, "Formation of dense partonic matter in relativistic nucleusnucleus collisions at RHIC: Experimental evaluation by the PHENIX Collaboration", *Nucl. Phys.*, A757: 1-2, 184-283, 2005.

[16] STAR Collaboration, "Experimental and theoretical challenges in the search for the quarkgluon plasma: The STAR Collaboration's critical assessment of the evidence from RHIC collisions", *Nucl. Phys.*, A757: 1-2, 102-183, 2005.

[17] BRAHMS Collaboration, "Quarkgluon plasma and color glass condensate at RHIC? The perspective from the BRAHMS experiment", *Nucl. Phys.,* A757: 1-2, 1-27, 2005.

[18] PHOBOS Collaboration, "The PHOBOS perspective on discoveries at RHIC", *Nucl. Phys.,* A757: 1-2, 28-101, 2005.

[19] BNL High Energy and Nuclear Physics Directorate, "Hunting the Quark Gluon Plasma Assessments by the experimental collaborations Results from the first 3 years at RHIC", https://www.phenix.bnl.gov, 2005.

[20] C. G. Callan et al., "High-Energy Electroproduction and the Constitution of the Electric Current",*Phys. Rev. Lett.*, 22, 156, 1969.

[21] J. I. Friedman, "Deep inelastic scattering: Comparisons with the quark model",*Rev. Mod. Phys.* 63, 597, 1991.

[22] Y. Nambu et al., "Dynamical Model of Elementary Particles Based on an Analogy with Superconductivity", *Phys. Rev.* 122, 345 (1961).

[23] Yu. L. Dokshitser, "Calculation of structure functions of deep-inelastic scattering and e^+e^- annihilation by perturbation theory in quantum chromodynamics",*JETP,* Vol. 46, No. 4, p. 641, 1977.

[24] G.Altarelli et al., "Asymptotic freedom in parton language",*Nucl. Phys.* B 126, 298, 1977.

[25] A. D. Martin et al., "Parton distributions for the LHC", *Eur. Phys. J* C63: 2, 189-285, 2009.

[26] K. J. Eskola et al., "EPS09: A New Generation of NLO and LO Nuclear Parton Distribution Functions", *JHEP*, vol. 04, p. 065, 2009.

[27] J. Aubert et al., "The ratio of the nucleon structure functions for iron and deuterium", *Phys. Lett.,* B317, 200, 1993.

[28] European Muon Collaboration, "Measurement of the proton structure function F_2 in muon - hydrogen interactions at 120-GeV and 280-GeV",*Phys.Lett.* B105, 315-321, 1981.

[29] P. B. Straub et al., "Nuclear dependence of high-xt hadron and high-τ hadron-pair production in p-A interactions a $\sqrt{s} = 38.8$ GeV", *Phys. Rev. Lett.*, 68, 452, 1992.

[30] CMS Collaboration, "In a World Without Color, Why do I believe in Gluons?", http://www.quantumdiaries.org/tag/event-displays/.

[31] F. Arleo et al., "Direct hadron production in hadronic collisions", *Nucl. Phys.,* B:207-208, 81-84, 2010.

[32] R. Maciua, "Double-parton scattering contribution to production of jet pairs with large rapidity separation at the LHC", *Phys. Rev.,* D90, 014022, 2014.

[33] A. O. Velasquez et al., "Color Reconnection and Flowlike Patterns in pp Collisions", *Phys. Rev. Lett.,* 111, 042001, 2013.

[34] CERN, "LEP Design Report", *CERN-LEP-84-01*, 1984.

[35] D. Leroy, "The superconducting magnets for LHC, in proceedings of the 15th International Conference on Charged Particle Accelerators, Protvino, Russian Federation", 1996.

[36] ATLAS Collaboration, "The ATLAS experiment at the CERN LHC", *JINST*, vol. 3, no. S08003, 2008.

[37] CMS Collaboration, "The CMS experiment at the CERN LHC", *JINST*, vol. 3, no. S08004, 2008.

[38] LHCb Collaboration, "The LHCb experiment at the CERN LHC", *JINST*, vol. 3, no. S08005, 2008.

[39] LHCf Collaboration, "The LHCf experiment at the CERN LHC", *JINST*, vol. 3, no. S08006, 2008.

[40] TOTEM Collaboration, "The TOTEM experiment at the CERN LHC", *JINST*, vol. 3, no. S08007, 2008.

[41] MoEDAL Collaboration, "Technical Design Report of the MoEDAL Experiment", *CERN-LHCC-2009-006*, 2009.

[42] B. Adeva et al., "The construction of the L3 experiment", *Nucl. Instrum. Meth.* A289, 35, 1990.

[43] ALICE Collaboration, "ALICE Inner Tracking System (ITS): Technical Design Report", *CERN-LHCC-99-012*, 1999.

[44] ALICE Collaboration, "ALICE time projection chamber: Technical Design Report", *CERN-LHCC-2000-001*, 2000.

[45] ALICE Collaboration, "ALICE transition-radiation detector: Technical Design Report", *CERN-LHCC-2001-021*, 2001.

[46] ALICE Collaboration, "ALICE Time-Of-Flight system (TOF): Technical Design Report", *CERN-LHCC-2000-012*, 2000.

[47] ALICE Collaboration, "ALICE high-momentum particle identification: Technical Design Report", *CERN-LHCC-98-019*, 1998.

[48] ALICE Collaboration, "Technical design report of the photon spectrometer", *CERN-LHCC-99-004*, 1999.

[49] ALICE Collaboration, "ALICE electromagnetic calorimeter: addendum to the ALICE technical proposal", *CERN-LHCC-2006-014*, 2006.

[50] ALICE Collaboration, "The forward muon spectrometer of ALICE : addendum to the technical proposal for a Large Ion Collider experiment at the CERN LHC", *CERN-LHCC-96-032*, 1996.

[51] ALICE Collaboration, "ALICE Zero-Degree Calorimeter (ZDC): Technical Design Report", *CERN-LHCC-99-005*, 1999.

[52] ALICE Collaboration, "ALICE dimuon forward spectrometer: Technical Design Report", *CERN-LHCC-99-022*, 1999.

[53] ALICE Collaboration, "ALICE Photon Multiplicity Detector (PMD): Technical Design Report", *CERN-LHCC-99-032*, 1999.

[54] ALICE Collaboration, "ALICE trigger data-acquisition high-level trigger and control system: Technical Design Report", *CERN-LHCC-2003-062*, 2003.

[55] ALICE Collaboration, "ALICE forward detectors: FMD, TO and VO: Technical Design Report", *CERN-LHCC-2004-025*, 2004.

[56] ALICE Collaboration, "ACORDE a cosmic ray detector for ALICE", *Nucl. Instrum. Meth.*, A572, 102, 2007.

[57] H. Muller, "Trigger electronics for the Alice PHOS detector", *Methods in Physics Research* A 518, 525528, 2004.

[58] S. van der Meer, "Calibration of the eective beam height in the ISR *CERN-ISR-PO-68-31*, 1968.

[59] C. Ohm et al., "The ATLAS beam pick-up based timing system", *Nucl. Instrum. Meth.* A623, 558-560, 2010.

[60] J. J. Gras, "Optimization of the LHC beam current transformers for accurate luminosity determination", *Tech. Rep. CERN-ATS-2011-063*, 2011.

[61] A. Boccardi, "LHC Luminosity calibration using the Longitudinal Density Monitor", *Tech. Rep. CERN-ATS-Note-2013-034 TECH*, 2013.

[62] P. Forck, "eam Position Monitor", *CERN-2009-005*, 2009.

[63] CERN Accelerator Beam Physics Group, "MAD-Methodical Accelerator Design", http://mad.web.cern.ch/mad/.

[64] M. J. Oreglia, "A Study of the Reconstructions $\psi' \to \gamma\gamma\psi$", *PhD thesis, SLAC, Stanford University*, Stanford, California 94305, 1980.

[65] Particle Data Group, "Mesons Summary Table", http://pdg.lbl.gov.

[66] P. Collins, "An Introduction to Regge Theory and High-Energy Physics", *Cambridge University Press*, 1977.

[67] B. Andersson, "Recent developments in the Lund model", arXiv:hep-ph/0212122

[68] K. Nakamura et al., "Review of particle physics", *J.Phys.* G37, 075021, 2010.

[69] P. M. Nadolsky et al., "Implications of CTEQ global analysis for collider observables", *Phys. Rev.* D78, 013004, 2008.

[70] ALICE TWiki, "Cross section scaling factors for MC productions with jet-jet and gamma-jet events ", https://twiki.cern.ch/twiki/bin/viewauth/ALICE/JetMCProductionsCrossSections .

[71] R. Brun et al., "GEANT3", *CERN-DD-EE-84-1*, BASE001, 13, 1987.

[72] ALICE Collaboration, "ALICE Off-line Project", https://alice-offline.web.cern.ch/ .

[73] C. Tsallis, "Possible Generalization of Boltzmann-Gibbs Statistics", *J. Statist. Phys.* 52, 479-487, 1988.

[74] ALICE Collaboration, "Neutral pion and η meson production in proton-proton collisions at $\sqrt{s} = 0.9$ TeV and $\sqrt{s} = 7$ TeV", *Phys. Lett.* B717, 162172, 2012.

[75] L. Lyons, "How to combine correlated estimates of a single physical quantity", *Nucl. Instrum. Meth.* A270, 110-117, 1988.

[76] P. Avery, "Combining Measurements with Correlated Error", CLEO Note CBX 95-55, 1996.

[77] A. Bylinkin, "Predictions on the transverse momentum spectra for charged particle production at LHC-energies from a two component model", *Eur. Phys. J.* C75, 166, 2015.

[78] ALICE Collaboration, "π^0 and η meson production in proton-proton collisions at $\sqrt{s} = 8$ TeV", arXiv:1708.08745 [nucl-ex].

[79] ALICE Collaboration, "Supplemental figures: π^0 and η meson production in proton-proton collisions at $\sqrt{s} = 8$ TeV", ALICE-PUBLIC-2017-009.

[80] O. Bourrion et al., "The ALICE EMCal L1 trigger first year of operation experience", *JINST* vol 8, C01013, 2013.

[81] TOTEM Collaboration, "Luminosity-Independent Measurement of the Proton-Proton Total Cross Section at $\sqrt{s} = 8$ TeV", *Phys. Rev. Lett.* 111, 012001, 2013.

[82] D. de Florian et al., "Parton-to-Pion Fragmentation Reloaded", *Phys. Rev.* D91, 014035, 2015.

[83] PHENIX Collaboration, "Inclusive cross section and double helicity asymmetry for π^0 production in p+p collisions at $\sqrt{s} = 62.4$ GeV", *Phys. Rev.* D76, 012003, 2009.

[84] PHENIX Collaboration, "Midrapidity Neutral-Pion Production in Proton-Proton Collisions at $\sqrt{s} = 200$GeV", *Phys. Rev. Lett.* 91, 241803, 2003.

[85] PHENIX Collaboration, "Inclusive cross section and double-helicity asymmetry for π^0 production at midrapidity in p+p collisions at $\sqrt{s} = 510$ GeV", *Phys. Rev. D* 93, 011501, 2016.

[86] ALICE Collaboration, "Production of π^0 and η mesons up to high transverse momentum in pp collisions at 2.76 TeV", *Eur. Phys. J.* C77:339, 2017.

[87] CMS Collaboration, "Measurement of the inclusive jet cross section in pp collisions at $\sqrt{s} = 2.76$ TeV" *Eur. Phys. J.* C76, 5, 265, 2016

[88] CMS Collaboration, "Measurement of the double-differential inclusive jet cross section at $\sqrt{s} = 8$ TeV" *CMS-PAS-SMP-14-001*, 2016.

[89] PHENIX Collaboration, "Detailed measurement of the e^+e^- pair continuum in p+p and Au+Au collisions at $\sqrt{s_{NN}} = 200$ GeV and implications for direct photon production", *Phys. Rev.* C 81, 034911, 2010.

[90] P. K. Khandai et al., "Meson spectra and m_{T} scaling in $p + p$, d+Au and Au + Au collisions at $\sqrt{s_{\text{NN}}} = 200$ GeV", *Phys. Rev.* C 84, 054904, 2011.

[91] M. L. Miller et al., "Glauber modeling in high energy nuclear collisions", *Ann. Rev. Nucl. Part. Sci.* 57, 205, 2007.

[92] CMS Collaboration, "Nuclear effects on the transverse momentum spectra of charged particles in pPb collisions at $\sqrt{s_{\text{NN}}} = 5.02$ TeV", *Eur. Phys. J.* C75:237, 2015.

[93] ATLAS Collaboration, "Transverse momentum, rapidity, and centrality dependence of inclusive charged-particle production in $\sqrt{s_{\text{NN}}} = 5.02$ TeV p+Pb collisions measured by the ATLAS experiment", *Phys. Lett.* B763, 313, 2015.

[94] H1 Collaboration, "Deep-inelastic inclusive ep scattering at low x and a determination of α_s", *Eur. Phys. J.* C21, 22, 2001.

[95] H1 Collaboration, "Measurement and QCD analysis of neutral and charged current cross sections at HERA", *Eur. Phys. J.* C30, 1, 2003.

[96] ZEUS Collaboration, "A ZEUS Next-to-Leading-Order QCD analysis of data on deep inelastic scattering", *Phys. Rev.* D 67, 012007, 2003.

[97] BCDMS Collaboration, "A high statistics measurement of the proton structure functions F_2(x,Q^2) and R from deep inelastic muon scattering at high Q^2", *Phys. Lett.* B 223, 485, 1989.

[98] New Muon Collaboration, "Measurement of the proton and deuteron structure functions, $F_2(p)$ and $F_2(d)$ and of the ratio σ_L/σ_T", *Nucl. Phys.* B 483, 3, 1997.

[99] J. Beringer et al., "Review of Particle Physics", *Phys. Rev.* D 86, 010001, 2012.

[100] T. Sostrand et al., "A Brief Introduction to PYTHIA 8.1", *Comput.Phys.Commun.* 178, pp. 852-867, 2008.

[101] Thomas Ullrich, "The emerging QCD frontier: the Electron-Ion Collider", *J. Phys.* G 35, 104041, 2008.

List of Figures

List of Tables